SMIP08

SMIP08 SEMINAR ON
UTILIZATION OF STRONG-MOTION DATA

Los Angeles, California
September 18, 2008

PROCEEDINGS

Sponsored by

California Strong Motion Instrumentation Program
California Geological Survey
California Department of Conservation

Co-Sponsors

California Seismic Safety Commission
California Office of Emergency Services
California Department of Transportation
Office of Statewide Health Planning and Development

The California Strong Motion Instrumentation Program (CSMIP), a program within the California Geological Survey (CGS) of the California Department of Conservation, records the strong shaking of the ground and structures during earthquakes for analysis and utilization by the engineering and seismology communities through a statewide network of strong motion instruments (www.conservation.ca.gov/CGS/smip). CSMIP is advised by the Strong Motion Instrumentation Advisory Committee (SMIAC), a committee of the California Seismic Safety Commission. Major program funding is provided by an assessment on construction costs for building permits issued by cities and counties in California, with additional funding from the California Office of Emergency Services, the California Department of Transportation and the Office of Statewide Health Planning and Development.

In July 2001, the California Office of Emergency Services began funding for the California Integrated Seismic Network (CISN), a newly formed consortium of institutions engaged in statewide earthquake monitoring that grew out of TriNet, funded by FEMA, and includes CGS, USGS, Caltech and UC Berkeley. The goals are to record and rapidly communicate ground shaking information in California, and to analyze the data for the improvement of seismic codes and standards (www.cisn.org). CISN produces ShakeMaps of ground shaking, based on shaking recorded by stations in the network, within minutes following an earthquake. The ShakeMap identifies areas of greatest ground shaking for use by OES and other emergency response agencies in the event of a damaging earthquake.

The Center for Engineering Strong Motion Data (CESMD) is operated by the CSMIP Program of the CGS in cooperation with the National Strong-Motion Project (NSMP) and the Advanced National Seismic System (ANSS) of the U.S. Geological Survey (USGS). The CESMD builds on and incorporates the CISN Engineering Data Center and will continue to serve the California region while expanding to serve other ANSS regions. The Data Center provides strong-motion data rapidly after a significant earthquake in the United States. Users also have direct access to data from previous earthquakes and detailed information about the instrumented structures and sites. The Data Center is co-hosted by CGS and USGS at www.strongmotioncenter.org

DISCLAIMER

SMIP08

SMIP08 SEMINAR ON
UTILIZATION OF STRONG-MOTION DATA

Los Angeles, California
September 18, 2008

PROCEEDINGS

Edited by

Moh Huang

Sponsored by

California Strong Motion Instrumentation Program
California Geological Survey
California Department of Conservation

Co-Sponsors

California Seismic Safety Commission
California Office of Emergency Services
California Department of Transportation
Office of Statewide Health Planning and Development

PREFACE

The California Strong Motion Instrumentation Program (CSMIP) in the California Geological Survey of the California Department of Conservation established a Data Interpretation Project in 1989. Each year CSMIP Program funds several data interpretation contracts for the analysis and utilization of strong-motion data. The primary objectives of the Data Interpretation Project are to further the understanding of strong ground shaking and the response of structures, and to increase the utilization of strong-motion data in improving post-earthquake response, seismic code provisions and design practices.

As part of the Data Interpretation Project, CSMIP holds annual seminars to transfer recent research findings on strong-motion data to practicing seismic design professionals, earth scientists and post-earthquake response personnel. The purpose of the annual seminar is to provide information that will be useful immediately in seismic design practice and post-earthquake response, and in the longer term, useful in the improvement of seismic design codes and practices. Proceedings and individual papers for each of the previous annual seminars are available in PDF format at http://www.consrv.ca.gov/CGS/smip/proceedings.htm The SMIP08 Seminar is the nineteenth in this series of annual seminars.

The SMIP08 Seminar is divided into two sessions in the morning and two sessions in the afternoon. The sessions in the morning include an invited presentation on the new California earthquake rupture forecast model, a presentation on near-fault instrumentation projects and accuracy of relative displacements, and three presentations on CSMIP-funded projects. These include the Turkey Flat ground motion prediction project and two presentations on foundation modeling techniques in building response analysis. The afternoon sessions include the 2008 Joyner Lecture by Chris Poland, on transparent seismic mitigation for community resilience, presentations by two investigators of CSMIP-funded projects on the Carquinez suspension bridge and ground motion tasks in the Tall Building Initiatives, and reports by two speakers on the strong-motion records and the field investigation of the M8.0 Wenchuan, Sichuan earthquake of May 12, 2008. Prof. Bill Iwan of Caltech will present a luncheon address on some milestones in strong motion monitoring.

Moh J. Huang, Ph.D., P.E.
CSMIP Data Interpretation Project Manager

Members of the Strong Motion Instrumentation Advisory Committee

Main Committee

Chris Poland, Degenkolb Engineers
Ali Sadre, Seismic Safety Commission, EsGil Corporation
Norman Abrahamson, Pacific Gas & Electric Company
Anil Chopra, UC Berkeley
Bruce Clark, Leighton & Associates
Martin Eskijian, California State Lands Commission
Wilfred Iwan, California Institute of Technology
Michael Keever, Caltrans
Maurice Power, Geomatrix Consultants
Daniel Shapiro, SOHA Engineers
Robert Anderson (ex-officio), Seismic Safety Commission

Ground Response Subcommittee

Maurice Power, Chair, Geomatrix Consultants
Abbas Abghari, Caltrans
Yousef Bozorgnia, PEER
Brian Chiou, Caltrans
Marshall Lew, MACTEC Engineering & Consulting
Geoffrey Martin, Univ. of Southern California
Ben Tsai, Pacific Gas & Electric Company

Buildings Subcommittee

Chris Poland, Chair, Degenkolb Engineers
Ali Sadre, Seismic Safety Commission, EsGil Corporation
Lucie Fougner, Degenkolb Engineers
Kenneth Honda, URS Corporation
Donald Jephcott, Structural Engineer
David Leung, City of San Francisco
Bret Lizundia, Rutherford & Chekene
Eduardo Miranda, Stanford University
Farzad Naeim, John A. Martin & Associates Engineers
John Robb, Structural Engineer
Chia-Ming Uang, UC San Diego
John Wallace, UC Los Angeles

Lifelines Subcommittee

Martin Eskijian, Chair, California State Lands Commission
David Gutierrez, DWR Division of Safety of Dams
Michael Keever, Caltrans
Stuart Nishenko, Pacific Gas & Electric Company
Vern Persson, DWR Division of Safety of Dams (retired)

Data Utilization Subcommittee

Wilfred Iwan, Chair, California Institute of Technology
Representatives from each Subcommittee

TABLE OF CONTENTS

SMIP08 SEMINAR ON UTILIZATION OF STRONG-MOTION DATA

September 18, 2008

USC Davidson Conference Center
3415 South Figueroa Street, Los Angeles, California

PROGRAM

8:00 am **REGISTRATION**

9:00 am **WELCOMING REMARKS**
Chris Poland, Strong Motion Instrumentation Advisory Committee (SMIAC)
Ali Sadre, California Seismic Safety Commission
John Parrish, State Geologist, California Geological Survey

9:10 am **INTRODUCTION**
Anthony Shakal, Manager, California Strong Motion Instrumentation Program
Moh Huang, California Strong Motion Instrumentation Program

Session I

Moderator: *Wilfred Iwan*, Caltech and SMIAC

9:15 am **The Uniform California Earthquake Rupture Forecast Version 2 (UCERF 2) and Its Effect on the National Seismic Hazard Maps**
Ned Field and others, US Geological Survey and SCEC, *and Chris Wills*, California Geological Survey

9:45 am **CSMIP Near-Fault Instrumentation Projects and Accuracy of Relative Displacements Computed from Strong-Motion Records**
Anthony Shakal, CSMIP

10:15 am **Turkey Flat Ground Motion Prediction – Initial Review**
Steve Kramer, University of Washington, Seattle

10:45 am Break

Session II

Moderator: *Chris Poland*, Degenkolb Engineers and SMIAC

11:05 am **Impact of Various Foundation Modeling on the Accuracy of the Response History Analysis of a Tall Building – Part I Foundation Modeling Methods**
Farzad Naeim, S. Tileylioglu, A. Alimoradi, JAMA *and Jonathan Stewart*, UC Los Angeles

11:35 am **Impact of Various Foundation Modeling on the Accuracy of the Response History Analysis of a Tall Building – Part II Response History Analysis**
Farzad Naeim, S. Tileylioglu, A. Alimoradi, John A. Martin & Associates, Los Angeles, *and Jonathan Stewart,* UCLA

12:05 pm **Luncheon**
Introduction *John Parrish,* State Geologist, California Geological Survey
Speaker*: Wilfred Iwan,* Caltech
Title: **Some Milestones in Strong Motion Monitoring**

Session III

Moderator: *Martin Eskijian,* California State Lands Commission and SMIAC

1:45 pm **Transparent Seismic Mitigation for Community Resilience**
The 2008 Joyner Lecture
Chris Poland, Degenkolb Engineers, San Francisco

2:25 pm **Identification of the Baseline Modal Parameters of the Carquinez Suspension Bridge Using Ambient Vibration Data**
Raimondo Betti and Ah Hong, Columbia University, New York

2:55 pm Break

Session IV

Moderator: *Maurice Power,* Geomatrix Consultants and SMIAC

3:15 pm **Ground Motion Tasks in the Tall Buildings Initiative**
Yousef Bozorgnia and Jack Moehle, PEER, UC Berkeley

3:45 pm **Preliminary Summary of Strong-Motion Records from the M8.0 Sichuan, China Earthquake of May 12, 2008**
Xiaojun Li, Zhenghua Zhou, China Earthquake Administration*, and Moh Huang, CSMIP*

4:00 pm **Impressions from a Field Investigation of the Wenchuan, Sichuan Province, Earthquake of May 12, 2008**
Marshall Lew, David Friedman and Laurie Johnson, EERI Field Investigation Team

4:30 pm **Adjourn**

THE UNIFORM CALIFORNIA EARTHQUAKE RUPTURE FORECAST VERSION 2 (UCERF 2) AND ITS EFFECT ON THE NATIONAL SEISMIC HAZARD MAPS

E. Field[1], T. Dawson[1], K. Felzer[1], A. Frankel[1], V. Gupta[2], T. Jordan[2], T. Parsons[1], M. Petersen[1], R. Stein[1], R. Weldon[2], and C. Wills[3]

[1] U.S. Geological Survey
[2] Southern California Earthquake Center
[3] California Geological Survey

Summary

The Working Group on California Earthquake Probabilities (WGCEP) has developed the Uniform California Earthquake Rupture Forecast version 2 (UCERF 2). This model was developed by the USGS, CGS, and SCEC, with significant support from the California Earthquake Authority. The time-independent model was developed jointly with the USGS National Seismic Hazard Mapping Program (NSHMP). As with past WGCEP and NSHMP efforts, the model depends on accurate fault locations and slip rates. This study updated fault locations based on the SCEC Community Fault Model and slip rates based on recent studies. The overall fault slip across the region was constrained by GPS deformation rates and long term plate rates. The resulting model is consistent with moment rates from GPS, long term plate tectonic models, and historic seismicity. A careful analysis of historical seismicity rates revealed an over-prediction of the rate of M>6.5 earthquakes in previous models, which we reduced to a 30% over prediction in UCERF 2 (within observed 95% confidence bounds).

Our study differs from previous WGCEP efforts by: 1) reporting earthquake probability for the entire state of California; 2) using uniform methodology across all regions; 3) compiling and using updated, uniform, and publicly accessible statewide data; 4) developing new methods to make models more rigorously adherent to observational data; 5) implementing in a modular (object-oriented), extensible framework, so that alternative logic-tree branches can easily be investigated and future updates can be quickly accommodated as new data and methods emerge. Advice and comment from the scientific and engineering communities was sought regularly through open meetings and workshops. Time-dependent probabilities were applied to fault-based sources using an empirical model (where long-term earthquake rates were adjusted according to any recent changes in observed seismicity) and using an elastic-rebound-motivated renewal model on major faults where the date of previous event was known.

Although UCERF2 is more complete and more consistent with geologic and seismic data than previous models, there are aspects of the model that we believe need improvement in the future. These include: assumptions regarding fault segmentation, the lack of fault-to-fault ruptures, and the lack of earthquake triggering and temporal clustering effects.

The UCERF2 served as the input fault model for calculation of the California portion of the National Seismic Hazard Map. The 2008 hazard maps are significantly different from the

2002 maps in many parts of the United States. The new maps for the Western United States indicate about 10-percent reductions for 0.2-s spectral acceleration and peak horizontal ground acceleration and up to 30-percent reductions in 1.0-s spectral acceleration at similar hazard levels. Most of the changes in the new maps can be attributed to the introduction of new attenuation relations for crustal and subduction earthquakes; however, changes to the fault and seismicity parameters also can be significant. In California, the ground motion calculated for the same hazard level increased up to 10 percent near major faults and up to over 15% in the Santa Barbara area and above the Cascadia Subduction Zone for 0.2-s spectral acceleration and peak horizontal ground acceleration. For 1.0-s spectral acceleration ground motions calculated for the same hazard level are lower everywhere except above the Cascadia Subduction Zone, but decrease less in the Santa Barbara area and the Mojave Desert, where the fault model was modified to reflect increased slip rates or new fault models.

Details of UCERF2 are contained in:
2007 Working Group on California Earthquake Probabilities (Edward H. Field, Timothy E. Dawson, Karen R. Felzer, Arthur D. Frankel, Vipin Gupta, Thomas H. Jordan, Tom Parsons, Mark D. Petersen, Ross S. Stein, Ray J. Weldon II, and Chris J. Wills), 2008, The Uniform California Earthquake Rupture Forecast, Version 2 (UCERF 2): U.S. Geological Survey Open-File Report 2007-1437 and California Geological Survey Special Report 203 [http://pubs.usgs.gov/of/2007/1091/].

Documentation for the National Seismic Hazards Maps is in:
Petersen, Mark D., Frankel, Arthur D., Harmsen, Stephen C., Mueller, Charles S., Haller, Kathleen M., Wheeler, Russell L., Wesson, Robert L., Zeng, Yuehua, Boyd, Oliver S., Perkins, David M., Luco, Nicolas, Field, Edward H., Wills, Chris J., and Rukstales, Kenneth S., 2008, Documentation for the 2008 Update of the United States National Seismic Hazard Maps: U.S. Geological Survey Open-File Report 2008–1128, 61 p. [http://pubs.usgs.gov/of/2008/1128/].

CSMIP NEAR-FAULT INSTRUMENTATION PROJECTS AND ACCURACY OF RELATIVE DISPLACEMENTS COMPUTED FROM STRONG-MOTION RECORDS

Anthony Shakal

California Strong Motion Instrumentation Program
California Geological Survey

Summary

Near-Fault Instrumentation

In the early 1980s a strong motion array was deployed near Parkfield in central California because of the expectation of an earthquake in the area. Important data had been obtained during the 1966 Parkfield, and given the prediction of a repeat earthquake in the 1980s, special arrays were deployed by both CGS and USGS. The CSMIP array included 45 strong motion stations, a significant investment at the time. The Parkfield earthquake eventually did occur on September 28, 2004 (magnitude 6.0 Mw). The resource investment was well warranted as very important data was recovered including some of the strongest accelerations ever recorded from a moderate earthquake. Beyond that, because of the design and scale of the array, one of the most dense set of near-fault recordings was obtained. These recordings showed near-fault motion that was highly variable, spatially, with accelerations well over 1 g within 1 or 2 km of accelerations near 0.1g – a factor of 10. The earthquake showed that near fault motion could be quite variable, and that more observations would be important to understand this result and its generality.

Currently, the two areas with the highest likelihood of a moderate or larger earthquake in California, according to the Working Group on California Earthquake Probabilities (WGCEP), are the Hayward fault in the San Francisco Bay area and the Coachella segment of the San Andreas fault in southern California. Considering the Hayward area, given the experience of the Parkfield ground motion, it was clear that if the ground motion were to be as variable as in the Parkfield event, the station density was far too limited to capture the variability. The CSMIP Strong Motion Instrumentation Advisory Committee (SMIAC) recommended that the Hayward area instrumentation be substantially increased. This represents a departure from the urban ground motion instrumentation focus of recent years, aimed at improving ShakeMap for response, to a focus of improving the learning from an event.

Significant progress has been made in the past two years on the Hayward area, partly because the USGS has also been working to expand the instrumentation. With the completion of stations planned by CSMIP, and those being considered by the USGS, station density should become comparable to Parkfield. Special purpose arrays are also important. For example, the USGS deployed a special subarray of 14 stations with spacing of a km or less, called UPSAR. Important questions, such as tracking the rupture process, can be addressed with such arrays. Although not directly equivalent, some special USGS arrays in the San Jose area will provide important close-spacing ground motion data.

In contrast with the Hayward East Bay area, the Coachella segment of the Southern San Andreas has relatively few stations. The expected event is larger, near a magnitude 7 according to the Working Group. The number of records from the close-in region of M>7 earthquakes is very limited. For input ground motion in designing for large earthquakes, artificially generated strong motion records are sometimes needed. To address this data paucity, a relatively large number of instruments are needed within the near fault zone of large events. Since the focus of these instruments, especially those located in lightly populated areas, is not for immediate usage in ShakeMap, but to obtain data to guide future design assumptions, some of the features necessary for ShakeMap-caliber instruments can be relaxed and simpler, more economical instruments can be deployed. For example, these instruments do not need communication capability and certain other features that drive up cost and power usage. Over the next two years, a significant number, perhaps over 100, of these simple low-cost instruments are planned to be deployed in the near-fault zone of the expected Coachella earthquake. They will of course be complemented by conventional seismic instruments of the USGS and CGS arrays.

Relative Displacement Accuracy

The accuracy of displacement computed from strong-motion records is important in accessing structural response. The inter-story drift, or relative horizontal displacement of adjacent floors, is a major factor in the seismic response of a building. High inter-story drifts are likely associated with incipient damage in the structure.

For early strong motion accelerographs, displacements could only be obtained after analog film records were laboriously digitized and processed. Because of the high noise intrinsic to this procedure, the displacements obtained from doubly integrating the digitized acceleration generally had high noise. Thus, relative displacements, obtained after differencing records from nearby sensors, often had high noise, especially at long period.

Error in computed displacements increases with period. At short period (e.g., 1 second or less), the error amplitude is small (a fraction of a cm). At periods of 5 to 10 seconds, the error in displacement can be significantly greater (several cm). In comparison with early instruments, modern 18-bit digital accelerographs have very low noise. Because of this, serious consideration can be given to utilizing the inter-story drift obtained through differencing accelerations obtained at nearby floors. Some tests were recently conducted as payload instrumentation on a NEES 3-story test structure at the UCSD shake table. Accelerometers were attached to the structure as well as on a nearby stationary tower, and a relative displacement sensor recorded the motion between them. The tests indicate that except for permanent displacements, the inter-story displacements obtained from a nearby pair of modern, low-noise accelerometers is quite accurate even at periods of several seconds.

TURKEY FLAT GROUND MOTION PREDICTION – INITIAL REVIEW

Steven L. Kramer

Department of Civil and Environmental Engineering
University of Washington, Seattle, Washington

Abstract

This paper describes an investigation of the ground motions recorded at the Turkey Flat test site, and of the predictions of those motions in the blind prediction symposium that took place in 2006. The subject investigation is currently in its early stages, so the current paper focuses on the site, measured subsurface conditions, and some of the characteristics of the recorded motions. A brief summary of the results of the ground motion predictions is also provided.

Introduction

The California Geological Survey Strong Motion Instrumentation Program (CSMIP) established an instrumented site effects array in a shallow valley at Turkey Flat, located 8 km southeast of the town of Parkfield about 5 km east of the San Andreas Fault in central California. The array was intended to provide data with which to investigate the accuracy and consistency of current methods for estimating the effects of site conditions on ground surface motions (Tucker and Real, 1986). The array became operational in 1987 and was subjected to numerous episodes of weak shaking; a weak-motion blind prediction exercise was conducted in 1989 (Real and Cramer, 1989; Cramer and Real, 1990a,b; Cramer, 1991). On September 28, 2004, the M6.0 Parkfield earthquake occurred producing much higher levels of ground shaking than the array had previously experienced. This event provided the ground motion records required to conduct the long-anticipated strong motion blind prediction test. In the two-phase test, recorded rock motions were provided to predictors in March, 2005 with predictions due in October, 2005, then additional motions were provided in October, 2005 with predictions due in February, 2006. A symposium was held in September, 2006 to reveal and discuss the measured and predicted surface motions.

Following the prediction symposium, a project was initiated to (a) investigate recorded ground response at the Turkey Flat array at different levels of shaking in multiple events, (b) evaluate equivalent linear and nonlinear blind predictions of site response in the September 28, 2004 Parkfield earthquake, (c) investigate differences between predicted and recorded motions at the various instrument locations, and (d) summarize lessons learned, recommended practices, and beneficial uses of strong motion records in site response prediction. Since the project was only recently begun, this paper provides a review of the Turkey Flat site, the recorded motions, and differences between the predicted and recorded ground motions from the prediction symposium.

Turkey Flat

The Turkey Flat site is located in a northwest-trending valley within the central California Coastal Range. The valley is filled with a relatively thin layer of stiff alluvial sediments with basement rock outcrops at the south and north ends of the valley (Figure 1). The valley is about 6.5 km long and 1.6 km wide, and is bounded on the north and east by the Maxim fault at the western flank of Table Mountain and on the south and west by a gentle topographic high (Real, 1988) near the Gold Hill fault. The valley is aligned with the southwest-plunging Parkfield syncline in which approximately 1 km of Upper Cretaceous and Tertiary strata overlying Franciscan basement are folded into a U-shape that dip at about 50^{o} and 70^{o} on the southwest and northwest flanks, respectively. The rock immediately underlying the valley sediments is sandstone of the Etchegoin formation.

Instrumentation Array

The Turkey Flat test site includes four recording sites – Rock South (labeled as R1 in Figure 1), Valley Center (V1), Valley North (V2), and Rock North (R2). Surface instruments were installed at each of these sites, and downhole instruments were also installed at the Rock South and Valley Center (Figure 2) sites. Downhole instrument D1 was located at a depth of approximately 24 m at the Rock South site, and downhole instruments D2 and D3 were located at depths of approximately 10 m and 24 m, respectively, at the Valley Center site. Instrument D3 was located about 1 m below the soil/rock boundary at the Valley Center site. Each instrument location included a three-component forced-balance accelerometer and a velocity transducer with 12-bit solid-state digital recording. CSMIP also established and maintained a 45-station wide-aperture strong-motion array across the Parkfield segment of the San Andreas fault several km from the Turkey Flat test site (McJunkin and Shakal, 1983).

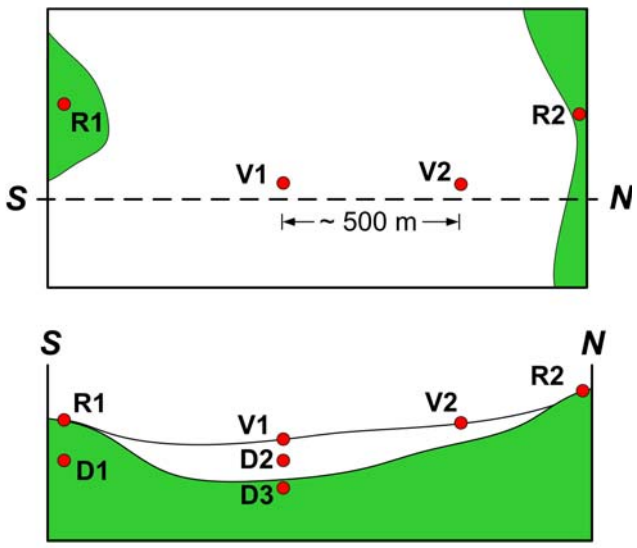

Figure 1. Schematic illustration of Turkey Flat instrumentation layout (after Tucker and Real, 1986).

Figure 2. Valley Center site looking west (after Real et al., 2006).

Subsurface Conditions

The Etchegoin sandstone formation underlies the alluvial sediments and outcrops at the borders of the valley. 25-m-deep boreholes at the southern outcrop showed medium brown to tan, highly friable sandstone with subangular to rounded, well-sorted grains composed of about 50% quartz (Real, 1988). The sandstone took on a bluish-gray color at a depth of about 14 m, which is believed to be the depth below which it remains saturated. Sandstone velocities (p- and s-wave) were measured by downhole, crosshole, and suspension logging tests; the results were interpreted as indicating two primary zones – an approximately 2.4-m-thick upper zone with V_s = 200 – 800 m/sec, and a lower zone with V_s = 700 – 1,500 m/sec. Review of individual logs indicates that the lower-velocity zone could extend to depths of approximately 6 m. Laboratory density measurements from samples in the upper 20 m showed relatively constant dry densities of 1.90 – 1.95 g/cm^3 and saturated densities of 2.20 – 2.23 g/cm^3.

The valley sediments were investigated by seismic reflection and refraction profiling, and by the installation of a dozen borings with sampling and insitu testing. The collective information was interpreted as indicating three primary soil units (Real, 1988). The upper unit consists of dark brown silty clay (at the Valley Center) to sandy clay (at Valley North). The middle unit consists predominantly of clayey sand that contains more gravel and sandy clay at the Valley North site than at the Valley Center. The lower unit fine to medium clayey sand with gravel. Shear wave velocities ranged from about 150 m/sec (Valley Center) to 135 m/sec (Valley North) in the upper unit, 460 m/sec (Valley Center) to 275 m/sec (Valley North) in the middle unit, and about 610 m/sec across the valley in the lower unit. The measured shear wave velocity data was used to construct "standard" profiles at the Rock South and Valley Center sites (Figure 3). Participants in the strong motion prediction exercise were required to make a prediction based on the standard profile, and encouraged to make another prediction using a "preferred" velocity profile based on their own interpretation of the field and laboratory velocity data.

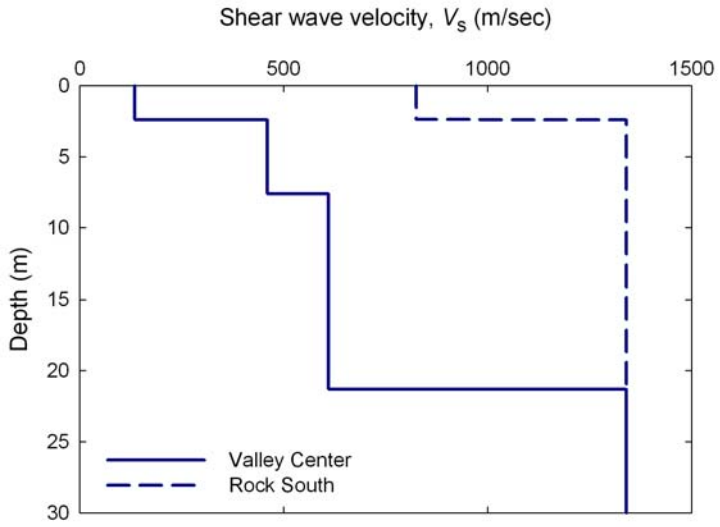

Figure 3. Standard shear wave velocity profiles for Valley Center and Rock South locations (after Real, 1988).

The September 28, 2004 Parkfield Earthquake

After some 17 years of operation, the Turkey Flat test site was subjected to strong ground shaking in the September 28, 2004 Parkfield earthquake. The earthquake was very well-documented and produced an extensive, dense set of near-fault strong motion records with measured peak accelerations of 2g or higher (Shakal et al., 2006a,b). The peak accelerations at the distance of the Turkey Flat test site were generally 0.3g or less.

Recorded Ground Motions

The acceleration time histories recorded at the Rock South and Valley Center arrays are shown in Figure 4. The time histories suggest a modest degree of amplification within the sandstone at the Rock South site; the NS component of the rock surface has a peak acceleration of 0.24g compared with a NS peak acceleration of 0.19g at the 24-m-deep R1 instrument. They also suggest a high degree of amplification at the Valley Center site; the NS peak accelerations at the ground surface (V1), mid-depth (D2), and rock (D3) instruments 0.29g, 0.12g, and 0.06g, respectively.

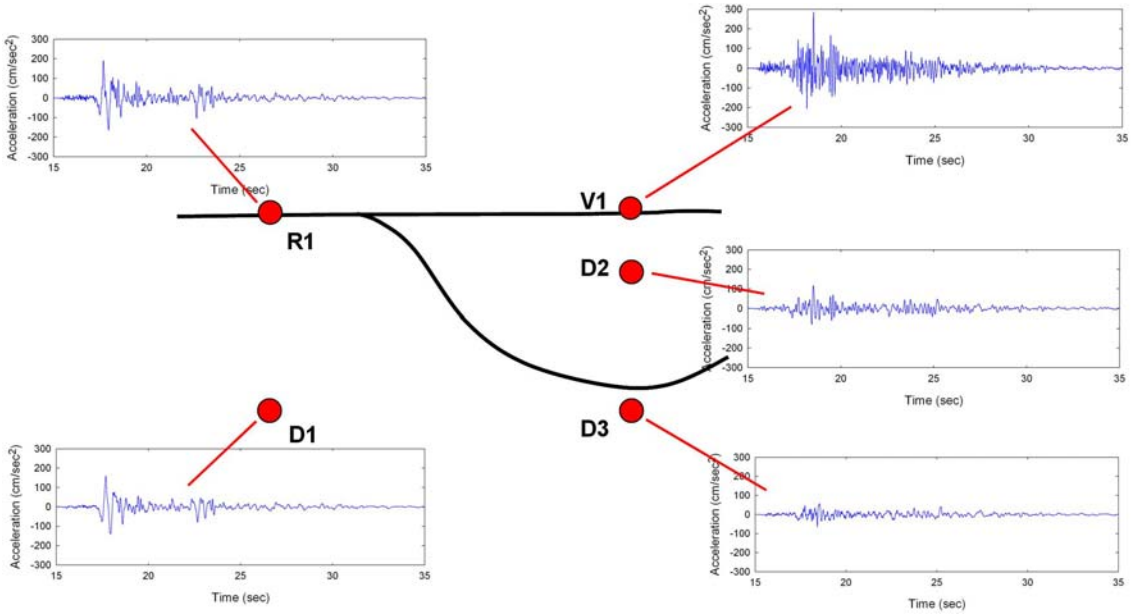

Figure 4. Time histories of North-South accelerations recorded at Rock South and Valley Center downhole arrays in September 28, 2004 Parkfield earthquake.

Response spectra for both components of the recorded motions are shown in Figure 5. At each instrument location, the NS and EW spectra are quite consistent, although the EW component of the D1 instrument was not recorded due to instrument malfunction. Nevertheless, the NS spectra at R1 and D1 are quite consistent, particularly at periods above about 0.3 sec where they are nearly identical. The R1 and D1 spectra are also nearly linear (in log-log space) over that range of periods. The NS response spectrum for the D3 instrument, which was located at the same depth below the Valley Center surface as the D1 instrument was below the Rock

South surface, is significantly weaker than the D1 spectrum at periods less than about 1.5 sec. The D3 spectrum also shows local peaks and valleys at periods above 0.3 sec, suggesting that some level of response not observed in the D1 record is occurring below a depth of 24 m at the Valley Center site.

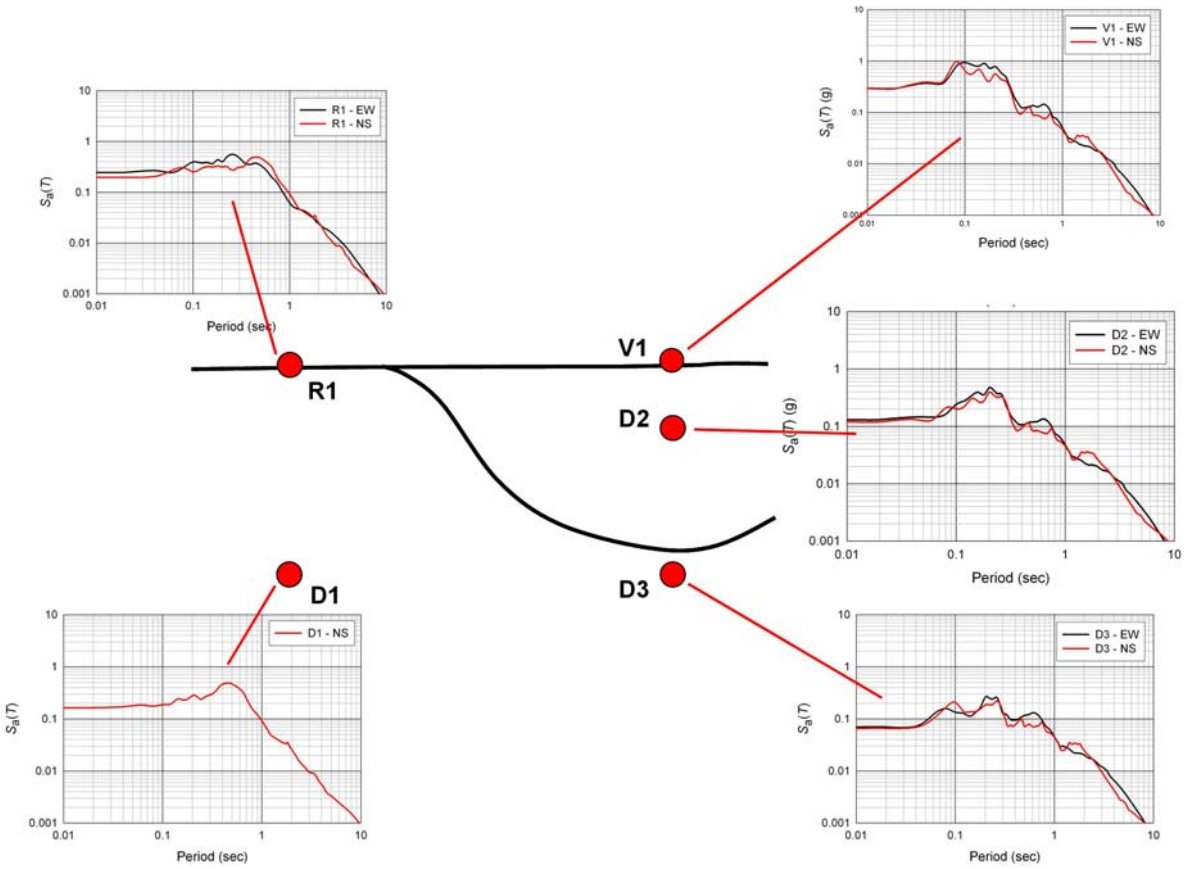

Figure 5. Response spectra from motions recorded at Rock South and Valley Center downhole arrays in September 28, 2004 Parkfield earthquake. EW component of D1 instrument was not recorded due to instrument malfunction.

Predicted Ground Motions

The strong motion prediction exercise was conducted in two phases. In the first phase, participants were provided with all available subsurface data and the recorded R1 motions, and asked to predict the response of the Valley Center profile. In the second phase, which was not initiated until all first-phase predictions had been received, participants were provided with the D3 motions and asked to predict the D2 and V1 motions. The first phase was therefore intended to represent the common situation in which recorded bedrock outcrop motions are used as input to ground response analyses, and the second to the much less common situation in which a downhole record is used excite a profile. Differences in the motions predicted by the two approaches depend on the extent to which the recorded downhole motion is similar to the "within profile" motion inferred from the rock outcrop motion and the assumed halfspace velocity.

Phase 1 Predictions

The range of predicted motions from equivalent linear analyses in the first phase are shown in Figure 6; the predictions of nonlinear analyses, though not shown here, were quite consistent with those of the equivalent linear analyses. The motions can be seen to agree with each other reasonably well, particularly at periods exceeding about 0.5 sec. The predicted spectra generally retain the linear nature of the R1 spectrum at periods greater than about 0.5-0.6 sec. Figure 7 shows the mean predicted spectrum along with the response spectrum for the recorded NS component at the Valley Center site (V1). The predicted spectra can be seen to greatly overpredict the recorded motions over a significant range of periods – approximately 0.3 – 1.5 sec.

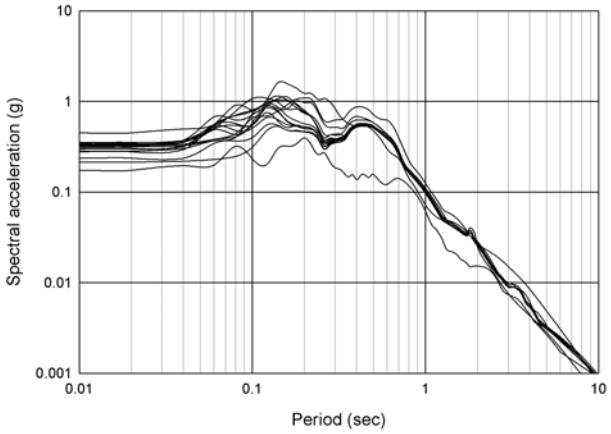

Figure 6. Equivalent linear predicted NS motions at surface of Valley Center site. Mean predicted spectrum indicated by bold line.

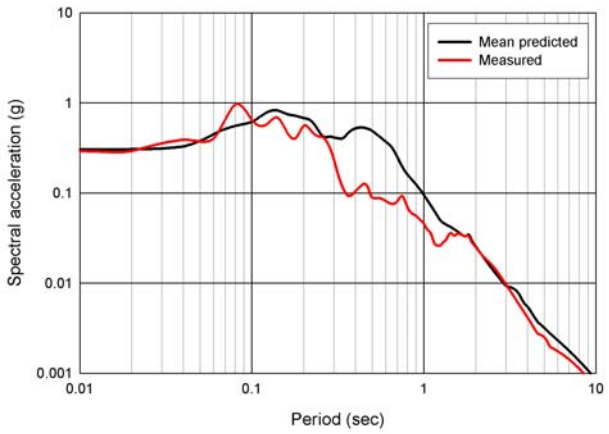

Figure 7. Recorded and mean equivalent linear predicted NS motions at surface of Valley Center site.

Phase 2 predictions

The second phase analyses were performed using the measured bedrock at the Valley Center site (D3) as the inputs to the Valley Center profile. The range of predicted motions from equivalent linear analyses in the second phase are shown in Figure 8; the predictions of nonlinear analyses were also quite consistent with those of the equivalent linear analyses. As in the case of the Phase 1 analyses, the predicted motions can be seen to agree with each other quite well over a wide range of frequencies. Figure 9 shows the mean predicted spectrum along with the response spectrum for the recorded NS component at the Valley Center site (V1). The predicted spectra can be seen to match the recorded motions very well over a broad range of periods. Due primarily to differences in the preferred velocity profiles selected by the predictors, the individual predicted spectra begin to differ from each other (and the mean, albeit modestly, from the actual) at periods less than about 0.2 sec.

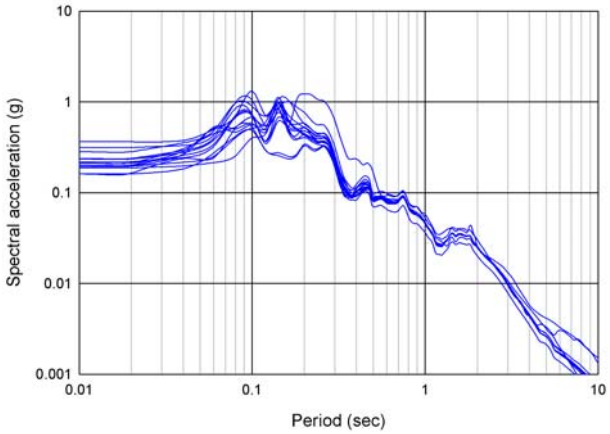

Figure 8. Equivalent linear predicted NS motions at surface of Valley Center site. Mean predicted spectrum indicated by bold line.

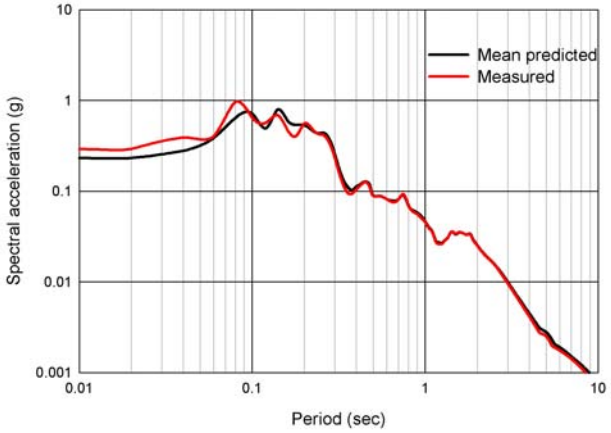

Figure 9. Recorded and mean equivalent linear predicted NS motions at surface of Valley Center site.

Comments

The high quality of the Phase 2 predictions (both equivalent linear and nonlinear), in which the Valley Center profiles selected by the participants were excited by the actual bedrock motions, indicates that (a) the site responded essentially one-dimensionally, as intended by the site developers, (b) the site responded essentially linearly in the 2004 Parkfield event, and (c) one-dimensional equivalent linear and nonlinear analyses were able to predict the measured surface response very well when the input motion was known accurately.

The low quality of the Phase 1 predictions, in which the Valley Center profiles were excited by modified versions of the Valley North rock outcrop motions, indicates that the common process of estimating within profile rock motions from nearby rock outcrop motions was not accurate, as applied by the predictors, in this particular case. This estimation process is affected by the characteristics of the rock at the rock outcrop, the characteristics of the rock and soil at the site to be analyzed, the characteristics of the measured rock outcrop motion, and the distance between the rock outcrop and the site at which the rock outcrop motion is to be used.

Preliminary Analyses

Of immediate interest is the reason for the difference in accuracy between the Phase 1 and Phase 2 predictions. Developing an understanding of the measured response requires a close look at the responses of both the Rock South and Valley Center profiles.

A sense of the response of the Rock South profile can be gained by examining at the R1 and D1 motions. The standard velocity profile for the Rock South site (Figure 3) shows a 2.4-m-thick layer of weathered sandstone with Vs = 825 m/sec. Using the familiar expression, $T = 4H/V_s$, implies that the shallow weathered sandstone layer would have a fundamental period of 8.6 Hz. As shown in Figures 4 and 5, the recorded R1 and D1 motions are quite similar in appearance (note that the EW component of the D1 motion was not recorded). Figure 10 shows the two motions plotted together, the variation with time of the difference between the two motions, and a spectrum of wavelet coefficients for the difference time history. The upper plot

confirms that the motions are quite similar in amplitude and phasing, and shows that the largest difference occurs during the strongest part of the motion, i.e., from about 17.5 – 19 sec. The middle plot confirms that observation, and the lower plot shows that the difference between the motions has a predominant frequency of about 8 – 10 Hz during that period of time. The "extra" ground surface response, therefore, appears to be consistent with excitation of the surficial weathered sandstone layer as characterized by the standard model; of course, this result could be caused by many combinations of weathered layer thickness and velocity.

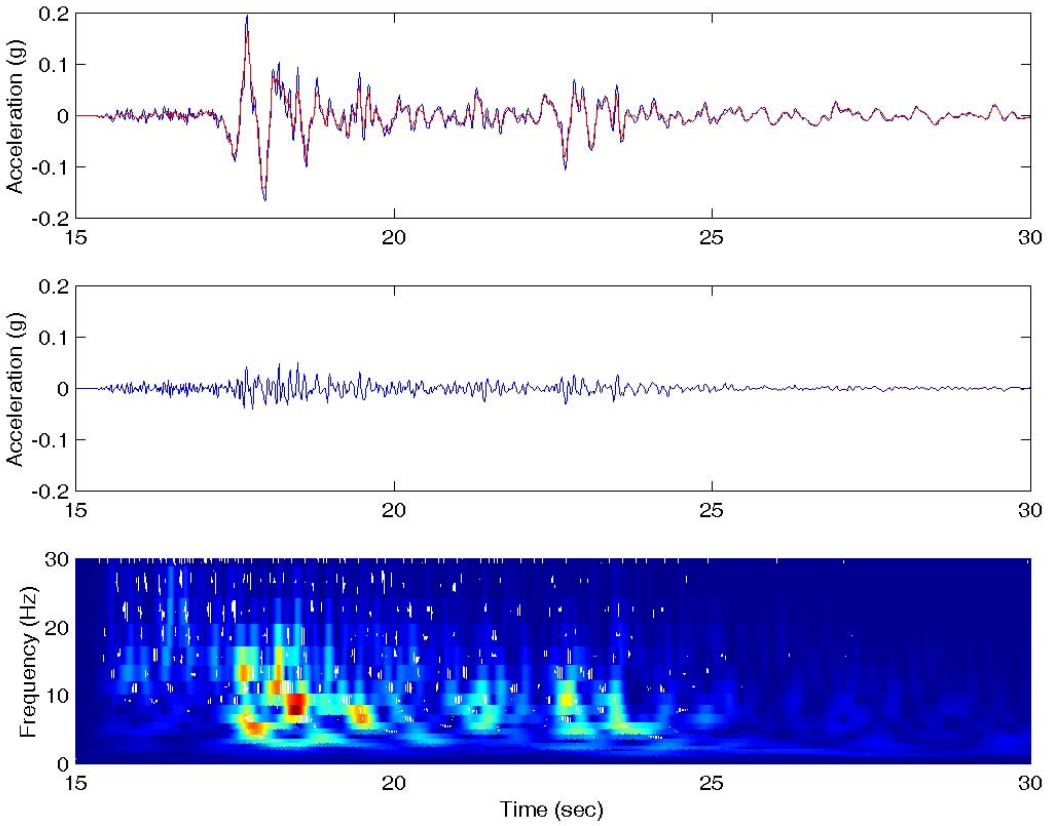

Figure 10. Rock South profile measurements: (upper) R1 (blue) and D1 (red) motions; (middle) R1 – D1 motion; and (lower) wavelet amplitudes vs. frequency and time for R1 – D1 motion.

The consistency of the R1 and D1 motions indicates that the Rock South profile behaved as expected and in a manner consistent with the standard Rock South velocity profile. The consistency of the V1 and D3 motions, and the accuracy with which the V1 motions could be predicted from the D3 motions, indicates that the upper 24 m of the Valley Center site behaved as expected. What is unexpected, therefore, is the relationship between the Rock South motions (at both R1 and D1) and the measured D3 motion. The expected D3 within-profile motion can be computed by using the preferred Valley Center profile with the measured R1 rock outcrop input motions. Figure 11 shows the measured and computed D3 motions corresponding to both components of the R1 record. Figure 12 shows the corresponding response spectra.

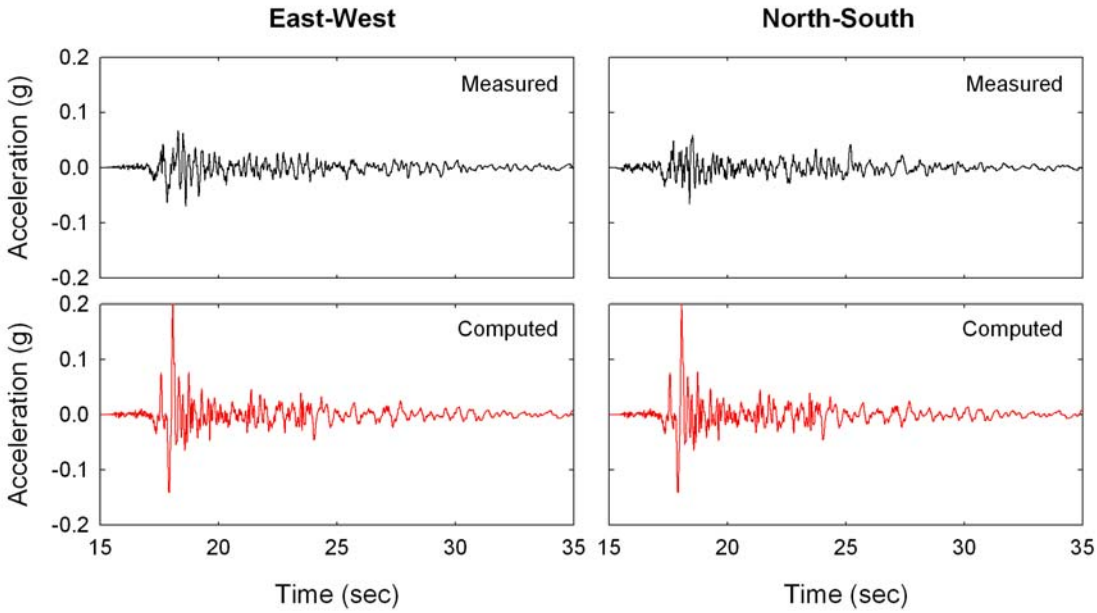

Figure 11. Measured and computed motions at location of D3 instrument. Computed motions are within-profile measurements based on measured R1 motions.

Using the standard Valley Center velocity profile, the computed D3 motions are much stronger than the measured motions in both the EW and NS directions, except at low frequencies (i.e., below about 0.5 Hz). The ratio of response spectra appears to have local maxima at periods of about 0.13 and 0.4 sec.

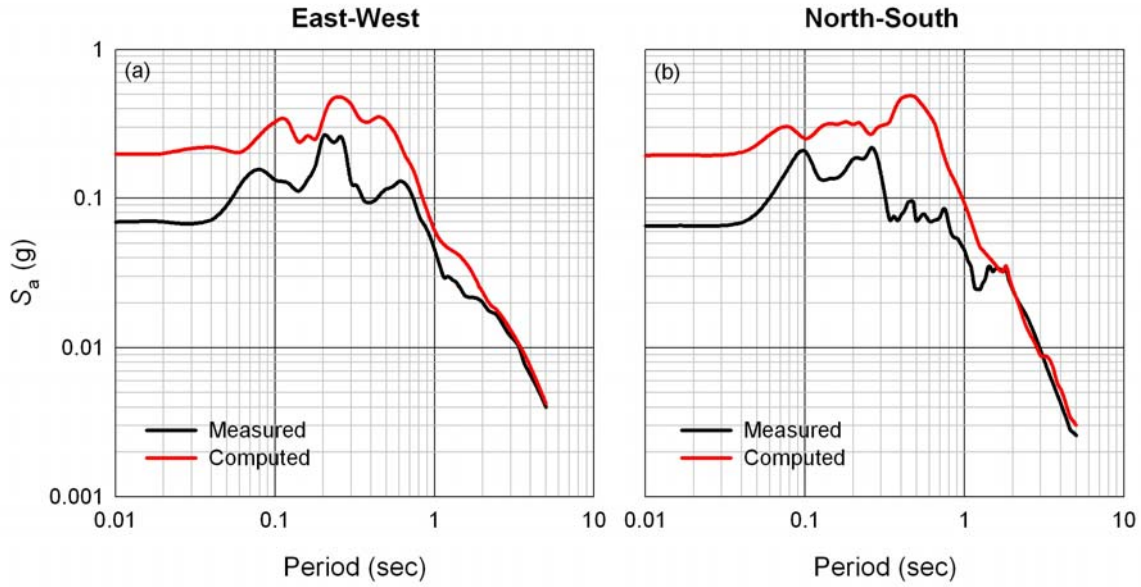

Figure 12. Measured and computed response spectra at location of D3 instrument. Computed motions are within-profile measurements based on measured R1 motions.

Figure 13 shows the computed and recorded NS components of the D3 record, and a plot of the ratio of the (natural logarithm of) wavelet coefficients of the two motions. The wavelet amplitude ratios indicate that the computed motion exceeds the recorded motion by the greatest

amount at frequencies of about 2 and 6 Hz, and that those frequencies remain relatively stable over the duration of the motion.

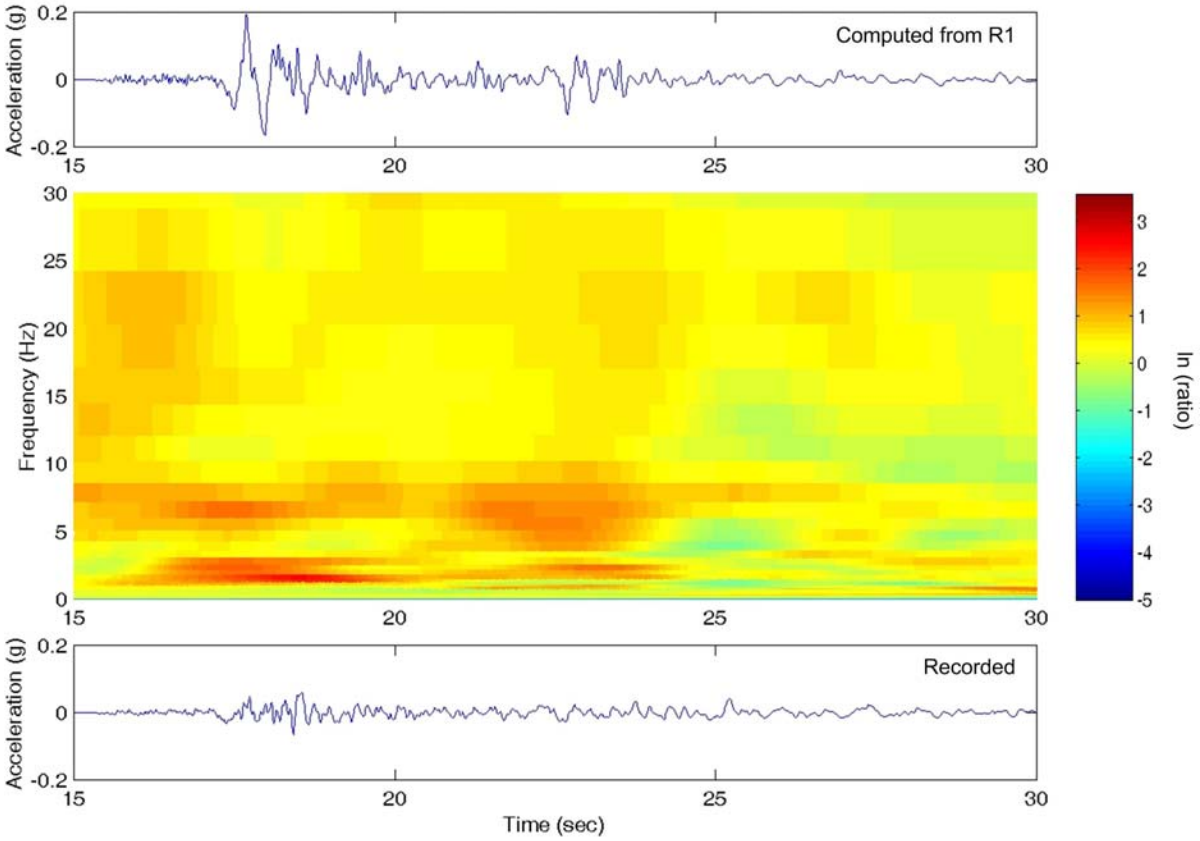

Figure 13. Time histories of NS component of D3 motion computed from R1 motion and recorded, and ratio of wavelet amplitudes (computed:recorded).

The Rock South array, at which the R1 motion was measured, is approximately 800 m from the Valley Center array. The Rock North station, at which the R2 motion was measured, is only about 300 m farther from the Valley Center array. If the Rock South motions were not available, it is likely that practicing geotechnical engineers would use the Rock North (R2) motions to predict the response at V1. Time histories from this type of analysis are shown in Figure 14. The V1 motions computed for the standard Valley Center velocity profile using both R2 components as inputs are significantly closer to the measured motions than those computed using the R1 motions as inputs. Figure 15 shows the response spectra from the motions in Figure 14; the computed spectra based on the R2 motions are much more consistent (though with some overprediction and underprediction in the 0.2 – 0.7 sec period range of the EW component, and overprediction from about 0.3 – 0.7 sec for the NS component) with the measured motions than those based on the R1 motions.

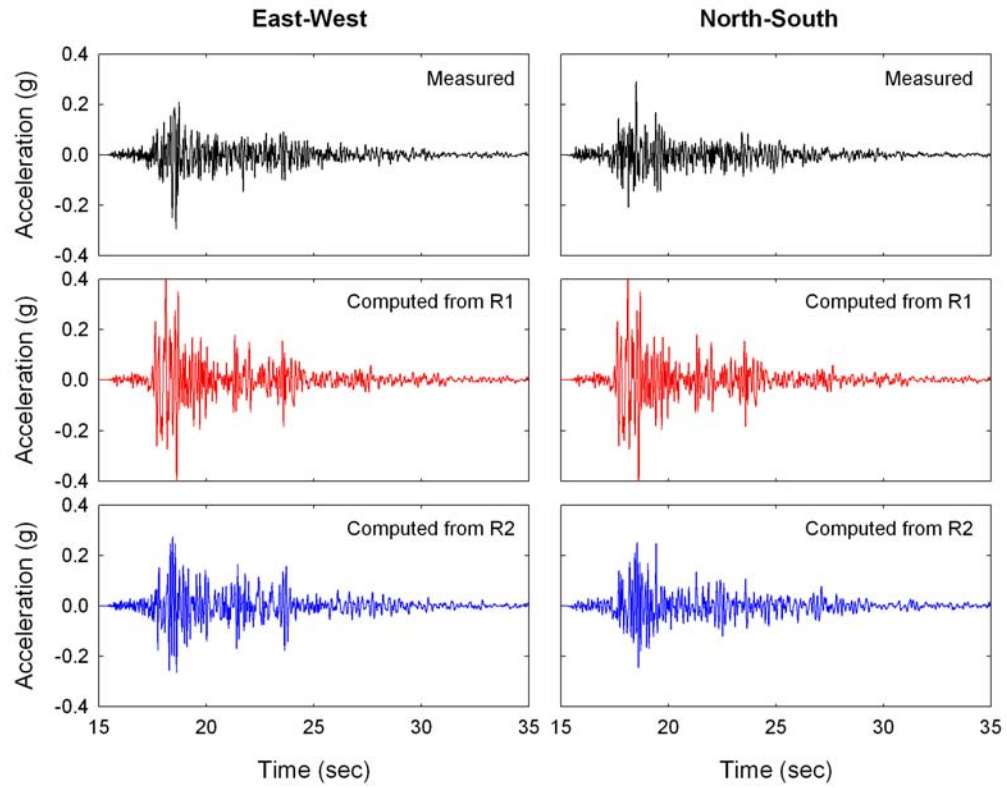

Figure 14. Measured and computed time histories for V1 instrument at Valley Center site.

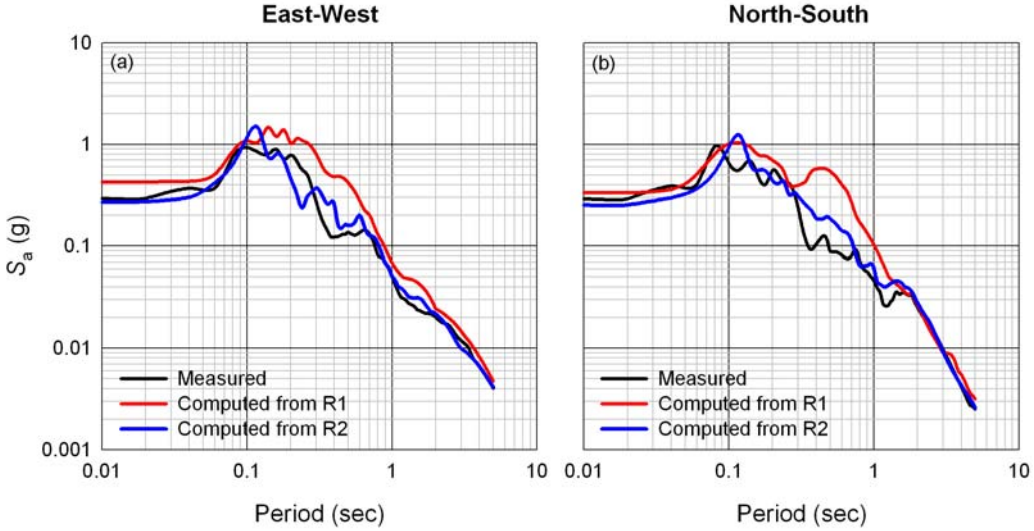

Figure 15. Measured and computed time histories for V1 instrument at Valley Center site.

Discussion

The strong motions recorded at the Turkey Flat instrumented site effects array raise some interesting questions about site characterization and response in both rock and soil materials. The response of the Rock South array appears to be consistent with one-dimensional response through the standard velocity model for that location, given the input motion recorded at 24 m

depth. The response of the Valley Center array also appears to be consistent with one-dimensional response through its standard velocity profile, given the input motion recorded at 24 m depth below that site. Predictions of the Valley Center response using the Rock South input motions, however, are not consistent with the measured response. Similar predictions using the Rock North input motions are much closer to the measured response, even though the Rock North site is farther from the Valley Center array than the Rock South site.

As stated previously, an investigation of the Turkey Flat response and its prediction in the strong motion blind test was recently begun. The project will involve detailed comparison of the predicted and observed motions with consideration of different methodologies, velocity profiles, material models, and other considerations. The lessons learned from the Turkey Flat tests will be evaluated and recommendations for site response calculations presented.

References

Cramer, C.H. (1991). "Turkey Flat, USA Site Effects Test Area – Report 6, Observations and Modeling," California Division of Mines and Geology, ESAU Technical Report No. 91-1, 92 pp.

Real, C.R. and Cramer, C.H. (1989). "Turkey Flat, USA Site Effects Test Area – Report 3, Weak Motion Test: Prediction Criteria and Input Rock Motions," California Division of Mines and Geology, ESAU Technical Report No. 89-1, 48 pp.

Cramer, C.H. and Real, C.R. (1990a). "Turkey Flat, USA Site Effects Test Area – Report 4, Weak Motion Test: Observed Seismic Response," California Division of Mines and Geology, ESAU Technical Report No. 89-1, 28 pp.

Cramer, C.H. and Real, C.R. (1990b). "Turkey Flat, USA Site Effects Test Area – Report 5, Weak Motion Test: Statistical Analysis of Submitted Predictions and Comparison to Observations," California Division of Mines and Geology, ESAU Technical Report No. 90-2, 57 pp.

McJunkin, R.D. and Shakal, A.F. (1983). "The Parkfield Strong-Motion Array," *California Geology*, Vol. 36, No. 2, pp. 27-34.

Real, C.R. (1988). "Turkey Flat, USA Site Effects Test Area – Report 2: Site Characterization," California Division of Mines and Geology, ESAU Technical Report No. TR 88-2, 39 pp.

Real, C.R., Shakal, A.F., and Tucker, B.E. (2006). "Turkey Flat, U.S.A. Site Effects Test Area: Anatomy of a Blind Ground-Motion Prediction Test," Third International Symposium on the Effects of Surface Geology on Seismic Motion, Grenoble, France, Paper Number KN 3, pp. 1-19

Shakal, A., H. Haddadi, V. Graizer, K. Lin and M. Huang (2006a). Some key features of the strong motion data from the M6.0 Parkfield, California, earthquake of 28 September 2004, *Bulletin of the Seismological Society of America*, Vol. 96, No. 4B, S90-S118.

Shakal, A., H. Haddadi and M. Huang (2006b). Note on the very high-acceleration Fault Zone 16 record from the 2004 Parkfield earthquake, *Bulletin of the Seismological Society of America*, Vol. 96, No. 4B, S119-S142.

Tucker, B. and Real, C.R. (1986). "Turkey Flat, USA Site Effects Test Area – Report 1: Needs, Goals, and Objectives," TR 86-1, California Department of Conservation, Division of Mines and Geology, 16 pp.

IMPACT OF FOUNDATION MODELING ON THE ACCURACY OF RESPONSE HISTORY ANALYSIS OF A TALL BUILDING

Farzad Naeim[1], Salih Tileylioglu[2], Arzhang Alimoradi[1] and Jonathan P. Stewart[2]

[1] John A. Martin & Associates, Inc., Los Angeles, California
[2] Department of Civil & Environmental Engineering, University of California, Los Angeles

Abstract

Soil-structure interaction can affect the response of buildings with subterranean levels by modifying the characteristics of input motions relative to those in the free-field and through the added system compliance associated with relative foundation/free-field translation and rocking. While procedures are available to account for these effects, they are seldom utilized in engineering practice. Our objective is to examine the importance of these effects on the seismic response of a 54 story building with four subterranean levels. We first generate a "most accurate" (MA) model that accounts for kinematic interaction effects on input motions, depth-variable ground motions along basement walls, compliant structural foundation elements, and soil flexibility and damping associated with translational and rocking foundation deformation modes. With reasonable tuning of superstructure damping, the MA model accurately reproduces the observed response to the 1994 Northridge earthquake. We then remove selected components of the MA model one-by-one to test their impact on building response. Factors found to generally have a modest effect on building response above ground level include compliance of structural foundation elements, kinematic interaction effects (on translation or rocking), and depth-variable ground motions applied to the ends of horizontal soil springs/dashpots. Properly accounting for foundation/soil deformations does not significantly affect vibration periods for this tall building (which is expected), but does impact significantly the distribution of inter-story drifts over the height of the structure. Two approximations commonly used in practice are shown to provide poor results: (1) fixing the structure at ground line with input consisting of free-field translation and (2) modeling subterranean soil layers using a series of horizontal springs which are fixed at their far ends and subjected to free-field ground accelerations.

1.0. Introduction

This article is a progress report on an ongoing project investigating the effects of various foundation modeling techniques on the computed response of building structures with embedded foundations. In analyzing the seismic response of a building with a basement, various approaches for modeling the base of the building can be employed. While some of these modeling approaches are very simple, others are complex and require significant effort in modeling the linear or nonlinear soil-structure interaction. What is not clear, however, is whether these more complex and time-consuming approaches actually produce substantially more accurate results.

Currently, over 180 buildings have been instrumented by CSMIP. Out of these, about 35 have subterranean floors and records from at least one earthquake (Naeim, et al. 2005). The four buildings shown in Figure 1 were selected for evaluation in this study. These buildings vary from low-rise stiff buildings to tall and flexible structures, as shown in Table 1. The focus of this article is on the response of Building No. 2 (LA 54 story building) during the 1994 Northridge earthquake.

Our analysis begins with the development of a three-dimensional model, which we call the "most accurate" (MA) model. Each MA model includes soil-foundation-structure interaction in the vertical and horizontal directions, including rocking, with a series of no tension springs and dampers reflecting site soil properties. The MA model of each building includes the embedded portion of the building and its foundations. Seismic demands imposed on the MA model include base translation and rocking (generally from recordings) as well as kinematic loading of basement walls (simulated by displacement histories applied to the ends of horizontal springs attached to basement walls).

Table 1. Buildings and earthquake records considered in this study

No.	*CSMIP ID*	*Name*	*Earthquake records*	*Embedment*	**Site Soil Condition**
1	24652	Los Angeles 6-Story Office	1. 1994 Northridge 2. 2001 Beverly Hills	1 level	Deep Alluvium
2	24629	Los Angeles 54 Story Office	1. 1994 Northridge 2. 1999 Hector Mines	4 levels	Alluvium
3	58503	Richmond 3 Story Gov. Office	1. 1989 Loma Prieta	1 level	Deep Alluvium
4	24322	Sherman Oaks 13 Story Office	1. 1987 Whittier 2. 1994 Northridge	2 levels	Alluvium

Using the aforementioned specification of "seismic demand," the MA model is calibrated to match the response interpreted from the recorded motions. Once the MA model successfully matches the recorded data, we replace components of the specified seismic demand and soil-foundation-structure interaction model (i.e., portions of the MA model that are below ground), one or more at a time, with various simplifications common in practice and assess the errors induced by each simplification on our estimates of various metrics of seismic response.

Many previous studies have been similar to the "MA" component of this work, in that they have developed mathematical models that replicate the recorded response of buildings (e.g., Chajes et al., 1996; Ventura et al., 2003; Kunnath et al., 2004; Liu et al., 2005). The novel aspect of the present work follows the MA model development. Those subsequent models simplify the MA model (without further calibration) so that the degree of error associated with each simplification can be evaluated. The objective is to find the simplest models which produce results of sufficient accuracy for engineering applications.

Following this introduction, we describe in Section 2 the attributes of the LA 54 story building. In Sections 3 and 4 we review a robust SFSI modeling procedure for buildings with subterranean levels and various simplifications to that procedure, respectively. Section 5 describes the challenges we faced with implementing the components of the SFSI model in a conventional structural analysis software package (ETABS). Finally, Sections 6 and 7 present the results of the study and conclusions, respectively.

(a) Building No. 1

(b) Building No. 2

(c) Building No. 3

(d) Building No. 4

Figure 1. Photos and instrumentation sketches for the buildings considered in this study

2.0 Details of the Los Angeles 54 Story Building

2.1. Structural and Foundation Systems

The building is 52 stories tall above ground level with a penthouse and a four-level basement. As shown in Figure 2, the building is roughly rectangular in plan with base dimensions of approximately 212 ft. by 136 ft, tapering inward at the 36th and 46th floors to 196 by 121 ft and 176 by 121 ft, respectively. The vertical load carrying system consists of composite concrete slabs (2.5 inches thick) over a 3 in. steel metal deck with welded metal studs, supported by steel frames. The spans between gravity columns vary from about 10 feet to 47 feet. The lateral load resisting system consists of moment resisting perimeter steel frame (framed tube) with 10 ft. column spacing. There are Virendeel trusses and 48 inch deep transfer girders at the setbacks at the 36th and 46th floors.

The foundation system consists of a reinforced concrete mat that is 9.5 ft thick in load bearing areas and 7 ft thick in intermediate areas. Concrete basement walls surround the subterranean levels.

2.2 Geotechnical Conditions

Geotechnical conditions at the site were characterized by LCA (1981) and are summarized by Stewart and Stewart (1997). The site exploration by LCA generally encountered 65 ft of sands with variable layers of silts and clays overlying siltstone and shale bedrock, which extended to the maximum depth explored of 130 ft. The shear wave velocities shown in Figure 3 are based on in situ downhole measurements by LCA (1981).

2.3 Recorded motions

The building is instrumented with 20 accelerometers (sensors) as shown in Figure 2. Sensors 1 and 2 installed on the top of the mat foundation measure vertical acceleration. The earthquakes recorded at the site are from 1992 Big Bear and Landers, 1994 Northridge, 2001 Hector Mine, and 2008 Chino Hills. The Northridge earthquake produced horizontal ground motions of about 0.14 g at the site whereas horizontal accelerations produced by Big Bear, Landers, Hector Mine and Chino Hills earthquakes were about 0.03 g, 0.04 g, 0.06 g and 0.02g, respectively.. In this article, we focus on the Northridge recordings.

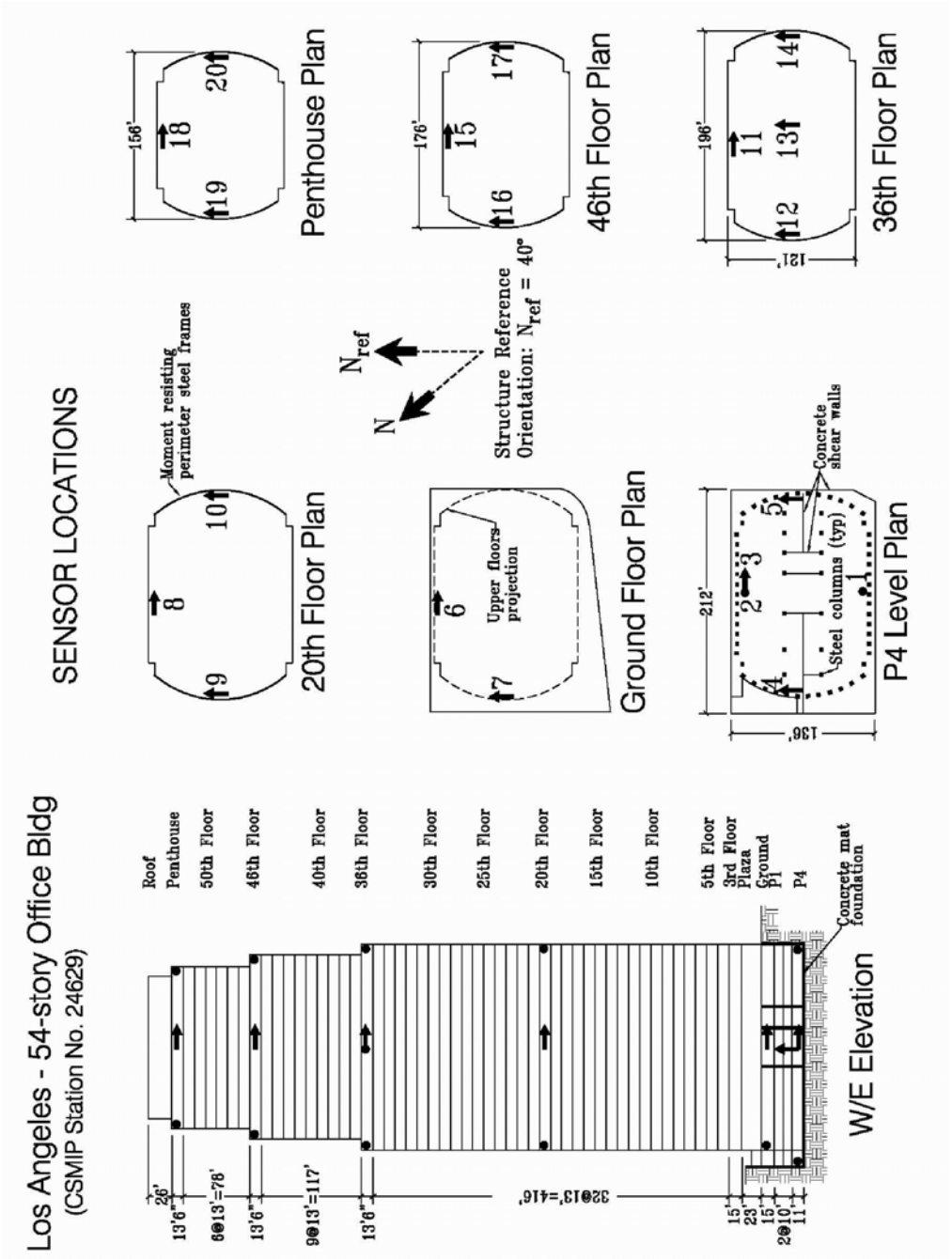

Figure 2. Instrumentation plan of the Los Angeles 54 Story Building

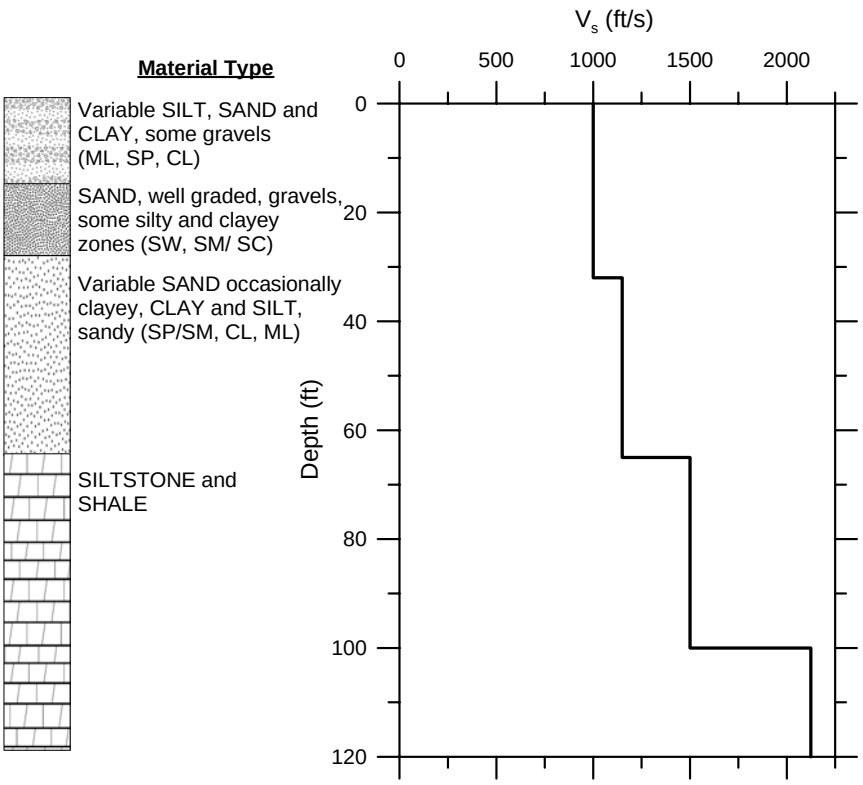

Figure 3. Geotechnical and shear wave velocity profile at LA 54 story building site

3.0 Soil-Foundation-Structure Interaction (SFSI) Modeling Procedures

3.1 General Procedures

SFSI modeling procedures have been recently presented by Stewart and Tileylioglu (2007). The following is extracted from that previous publication.

A schematic illustration of a building with subterranean levels is shown in Figure 4a. The actual soil-foundation-structure system is excited by a wave field that is incoherent both vertically and horizontally and which may include waves arriving at various angles of incidence. These complexities of the ground motions cause foundation motions to deviate from free-field motions (denoted u_g). This complex ground excitation acts on stiff, but non-rigid, foundation walls and the base slab, which in turn interact with a flexible and nonlinear soil medium having a significant potential for energy dissipation. Finally, the structural system is connected to the base slab, and possibly to basement walls as well.

A substructure approach is used to account for these complex SFSI effects, as illustrated in Figures 4b-d. As shown in Figure 4b, the first step in the substructure approach involves evaluating the motion that would be expected to occur on the foundation slab if the superstructure was absent and the foundation had no mass. This motion is termed the *foundation input motion* (FIM), and it accounts for the complexities of the incident wave field and its

interaction with the stiff foundation system. For deeply embedded foundations, the dominant mechanism affecting base slab motions are embedment effects associated with ground motion reductions that occur below the original ground surface. The analysis of the foundation input motion is commonly referred to as a *kinematic interaction* analysis. The foundation input motion consists of horizontal motions denoted u_{FIM} and rotations denoted θ_{FIM}.

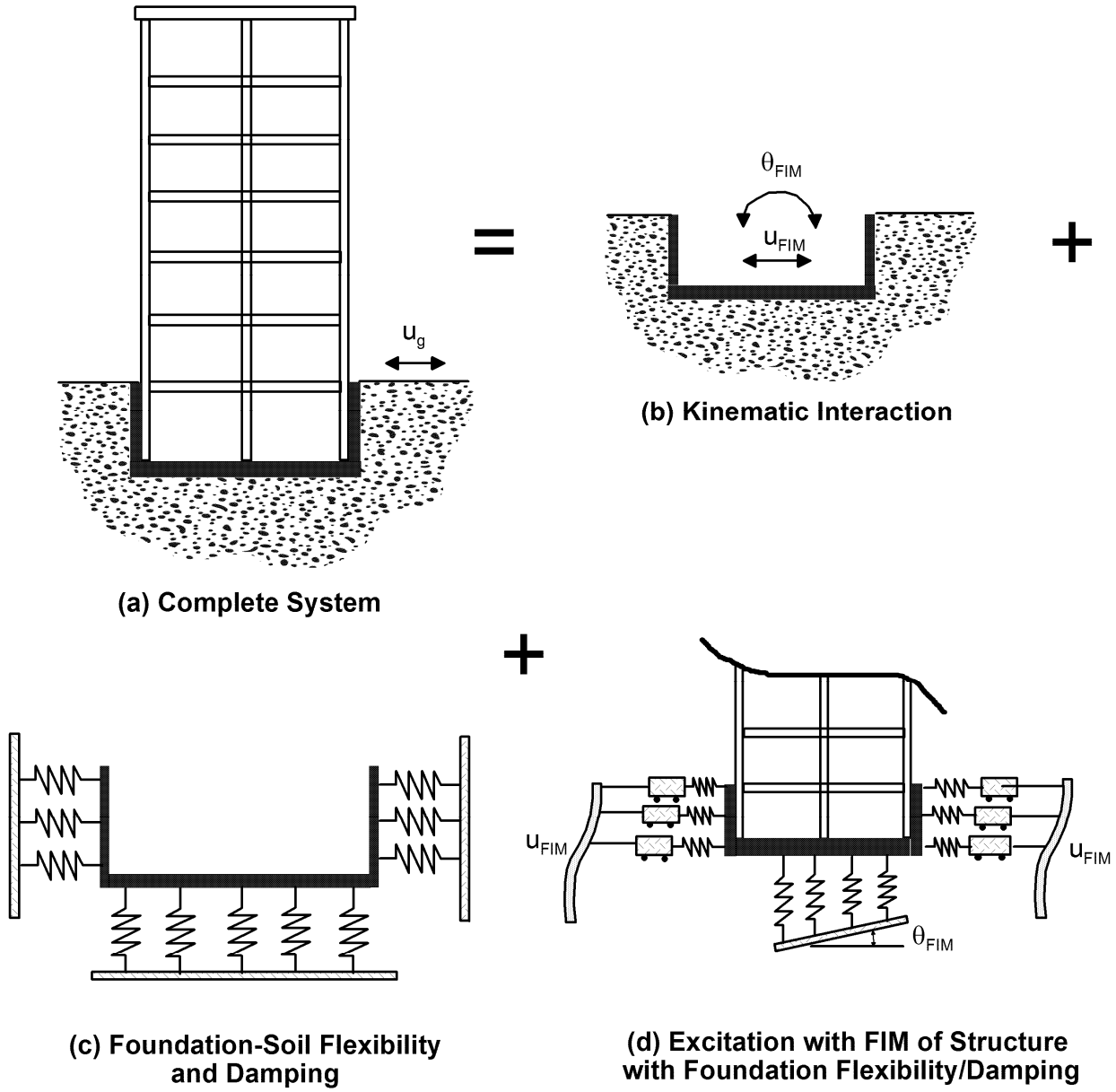

Figure 4. Schematic illustration of the substructure approach to the solution of the soil-foundation-structure interaction problem using distributed foundation springs.

In the second step the stiffness and damping characteristics of the foundation-soil interaction are characterized using a series of distributed springs and dashpots acting around the foundation (illustrated in Figure 4c). Only springs are depicted in Figure 4c for simplicity, but

dashpots are used in parallel to the springs (alternatively, the springs can be visualized as being complex-valued, which accounts for damping).

As shown in Figure 4d, the final step involves placing the superstructure atop the foundation and exciting the system by displacing the ends of the springs using the rocking and translational components of the foundation input motion. Note that differential ground displacements are applied over the height of the basement walls (= depth of embedment) because of the vertical incoherence of ground motion.

3.2 Application to the LA 54 Story Building

There is not a free-field instrument at the LA 54 story building, hence u_g is unknown. What is known is the horizontal translation at the base of the building and the rotation in the short (transverse) direction of the structure (because of the two vertical instruments on the base slab).

The recorded horizontal translation provides a good estimate of u_{FIM}. In reality, the recording is also affected by inertial soil structure interaction effects, which cause the foundation base translation to differ from u_{FIM}. However, those effects are small for buildings such as the LA 54 story building with weak inertial soil-structure interaction effects. Even when they are strong, such effects are narrow-banded at the first mode system frequency (Kim and Stewart, 2003). Hence, we take u_{FIM} as the base mat horizontal recording. Conversely, the base rotation is likely to be dominated by inertial interaction effects, so we do not rely on recordings to estimate this quantity. Instead, it is estimated based on predictions of validated theoretical models (Stewart and Tileylioglu, 2007). Those models allow the estimation of transfer functions that relate free-field motion u_g to the translational and rotational FIMs:

$$\left|H_u\right| = \frac{u_{FIM}}{u_g},\ \left|H_\theta\right| = \frac{\theta_{FIM}}{u_g} \tag{1}$$

where $\left|H_u\right|$ and $\left|H_\theta\right|$ are translational and rotational transfer functions (respectively) that can be evaluated as a function of frequency knowing the soil shear wave velocity and foundation dimension (expressions in Stewart and Tileylioglu, 2007). Figure 5a presents these functions for the LA 54 building site using the aforementioned expressions. Given $\left|H_u\right|$ and $\left|H_\theta\right|$, base rotation can be estimated from u_{FIM} through manipulation of Eq. 1 to yield:

$$\theta_{FIM} = u_{FIM}\frac{\left|H_\theta\right|}{\left|H_u\right|} \tag{2}$$

To summarize, the translational motion applied at the end of the foundation spring attached to the base slab is u_{FIM} (taken from recordings). The vertical motions applied at the end of vertical springs are defined from the product of θ_{FIM} and horizontal distance to the foundation centroid.

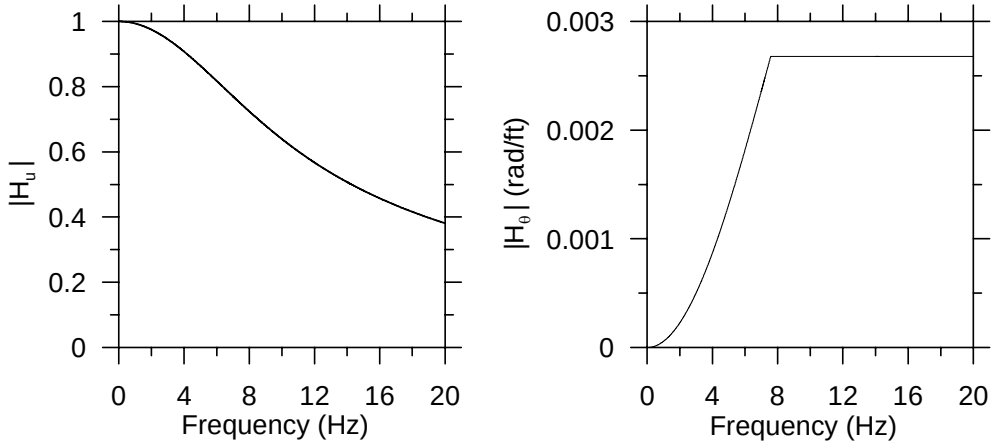

Figure 5a. Theoretical transfer functions between foundation input motions and free-field motion

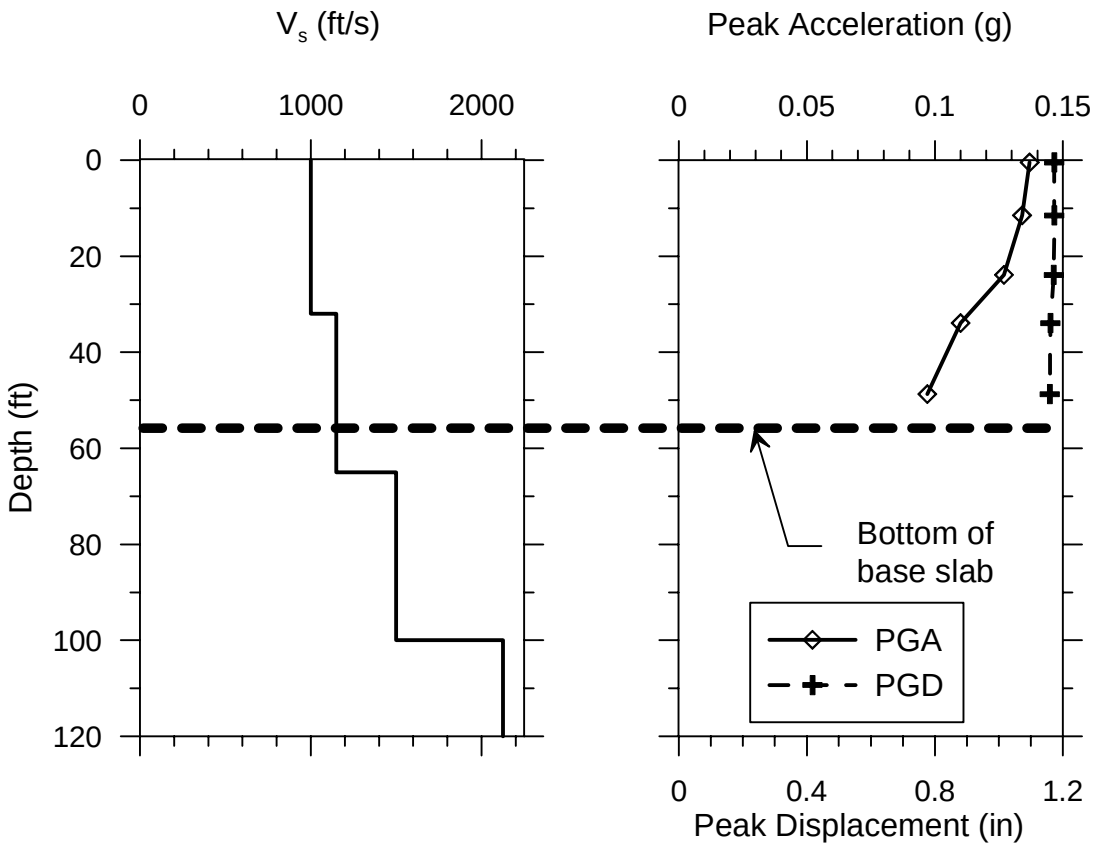

Figure 5b. Variation of peak acceleration with depth at ends of foundation springs, as calculated from ground response analysis.

The remaining issue for ground motion specification is the distribution of translations over the embedment depth, as illustrated in Figure 4d. This is evaluated by performing equivalent-linear ground response analysis with the input consisting of u_{FIM} at the average foundation depth of 46 ft as an outcropping motion. Those analyses were performed with SHAKE04 (Youngs, 2004), which is a modified version of SHAKE91(Idriss and Sun, 1992). We used the velocity profile shown in Figure 3 and nonlinear modulus reduction and damping curves as specified in EPRI (1993), Vucetic and Dobry (1991) and Seed and Idriss (1970). Figure 5b shows that the variation of ground motion over the embedment depth is minor in displacements but is significant in accelerations.

The foundation springs and dashpots are evaluated by first calculating translational (K_x, K_y) and rotational (K_{xx}, K_{yy}) stiffnesses for rectangular rigid foundations (Mylonakis et al., 2002). Dashpot coefficients (C_x, C_y, C_{xx}, C_{yy}) can be similarly evaluated using equations from Mylonakis et al. (2002). Foundation stiffnesses are shown in Figure 6a for the LA 54 story building site. For translation, the portion of the stiffness that can be attributed to the base slab is calculated using surface foundation equations in conjunction with the seismic velocities of materials below the mat. That stiffness is applied as a spring at the elevation of the foundation mat (Figure 4c). The total translational stiffness of the foundation is higher due to embedment, and the difference is applied as horizontal springs distributed along the basement walls. For rotation, vertical springs are distributed along the base of the foundation as shown in Figure 6b. Higher stiffnesses are assigned at the boundaries, but the overall rotational stiffness associated with the vertical springs matches that from the impedance function. This is accomplished by ensuring that the following equalities hold:

$$K_{xx} = \sum_i k_{z,i} \cdot y_i^2 \qquad (3)$$
$$K_{yy} = \sum_i k_{z,i} \cdot x_i^2$$

where K_{xx} and K_{yy} = overall rotational stiffness of foundation (Figure 6a), $k_{z,i}$ = stiffness of vertical spring at location indexed by i, x_i=closest horizontal distance from spring i to the y-centroidal axis of foundation, and y_i=closest horizontal distance from spring i to the x-centroidal axis of foundation. Distances x and y are measured from the centroid as illustrated in Figure 6a. The vertical stiffness values given in Figure 6b satisfy Eq. 3.

Both the horizontal and vertical springs are specified as “compression-only,” meaning that no tension is allowed to develop. This allows a gap to form, although the implementation does not track gap width.

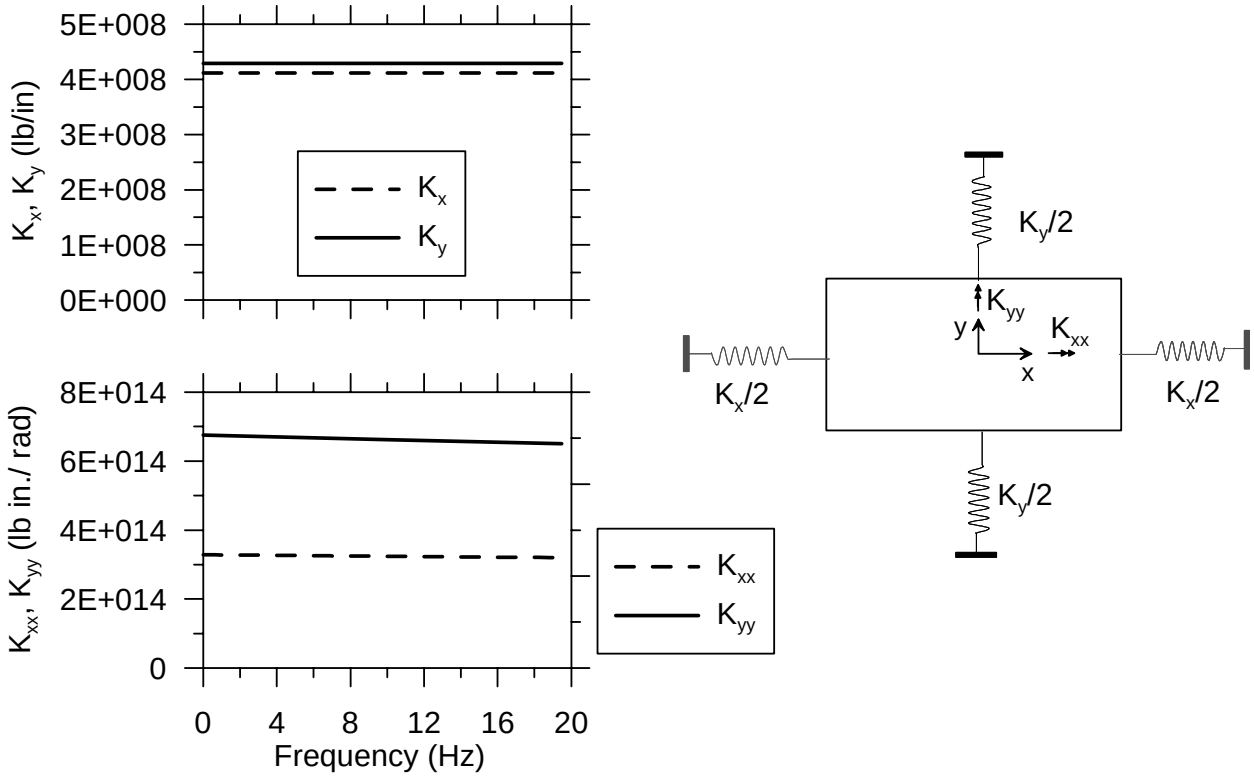

Figure 6a. Foundation impedance functions (stiffness portion) for overall foundation system

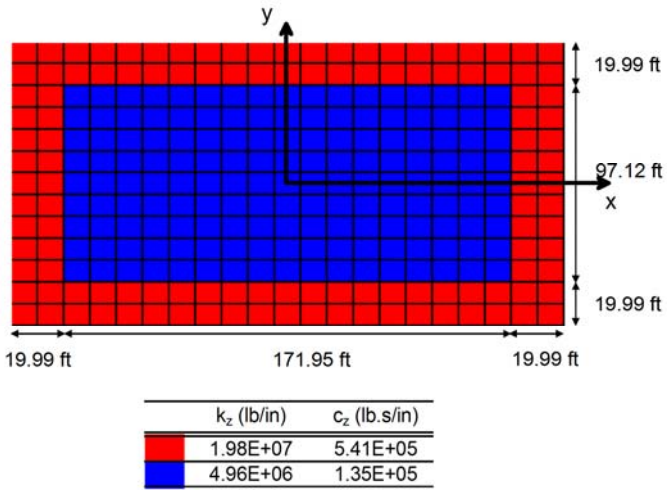

Figure 6b. Distribution of vertical foundation springs and dashpots across base slab

4.0 Simplifications to SFSI Modeling Considered in Present Study

The simplifications to the MA model fall into three categories, as illustrated in detail in Table 2:

Model 1: Replacement of compliant foundation structural elements (i.e., base slab and basement walls) representing actual cracked section properties with rigid elements.

Models 2a-c: Modification of the seismic demand to remove various aspects of the kinematic response and depth-variable ground motions.

Models 3a-d: Modification (or removal) of foundation springs.

Table 2. Summary of the properties of the MA model and the simplified models considered

Model	Compliant Found. Elements	Seismic Demand			Soil Flexibility				
		Kinematic base rocking ($\theta_{FIM}\neq0$)	Depth variant ground motion	Kinematic base translation ($u_{FIM}\neq u_g$)	No-tension springs	H & V springs at base slab	H springs on basement walls	Ignore soil; fix structure at base slab level	Ignore soil; fix structure at ground surface
MA	●	●	●	●	●	●	●		
1		●	●	●	●	●	●		
2a	●		●	●	●	●	●		
2b	●	●		●	●	●	●		
2c	●		●		●	●	●		
3a	●	●	●	●		●	●		
3b	●						●		
3c								●	
3d									●

Details of the specific modifications to the MA model are explained in the following:

1. The embedded portion of the building is assumed to be rigid. The specification of seismic demand is not modified. The objective here is to specifically investigate the effects of compliance in structural elements below ground line.

2. Change the manner in which seismic demand is specified. Three deviations from the MA model are investigated:

    a. Ignore the effect of base rocking in the specification of seismic demand (note that rocking from inertial interaction is still allowed; essentially the ends of the vertical springs on the base slab are not provided with excitations compatible with the rocking that would normally be expected from kinematic interaction).

b. Ignore the effect of kinematic loading of basement walls associated with depth-variable displacement histories applied to the ends of horizontal foundation springs. Essentially, this analysis deviates from the MA model only by fixing the ends of the horizontal springs attached to the basement walls.

c. Neglect kinematic interaction altogether by replacing the recorded motions at the base of the building by equivalent free-field motions (u_g calculated from u_{FIM} using Eq. 1 and Fig 5a; rotation taken as zero).

3. Change the manner in which soil flexibility is modeled. Specifically, we investigate:

a. Allowing springs to develop tension (removal of no-tension interface elements).

b. Neglect entirely soil flexibility at the level of the base slab (i.e., the base slab is fixed vertically and horizontally), and simulate soil flexibility along the basement walls with horizontal springs with ends fixed to match the free-field ground motion. Seismic demand consists only of horizontal motions (equivalent free-field condition) at the base slab level and at the ends of foundation springs. This simulates a condition commonly used in structural design offices.

c. Same as 3(b), except soil flexibility along basement walls is neglected (no soil springs). In this model, the height of the structure is effectively lengthened by the embedment depth and the model is fixed at the level of the base slab. This simulates another condition commonly used in some structural design offices.

d. The below ground portion of the building is ignored and the superstructure is assumed to be fixed at the ground level. Seismic demand consists only of horizontal motions (equivalent free-field condition) applied at ground level. This is the third (and final) condition commonly used in some structural design offices.

5.0 Implementation Issues

Several computing platforms for conducting SFSI analyses were considered. Since our objective was to produce modeling recommendations suitable for adaptation by design offices, we decided to utilize a software system that is most commonly used for dynamic structural analysis of buildings by reputable firms. Therefore, we decided to use ETABS computer program (Computers and Structures, 2008) for this study. Use of more powerful software such as OpenSees (PEER, 2008) may have dramatically reduced the troubles we faced, but would not have produced recommendations that were directly applicable to a design office environment.

Our MA and most other building models are subjected to multiple horizontal and vertical excitations. Horizontal soil springs at various levels and in N-S (y) and E-W (x) directions are excited by distinct input motions at their ends. The vertical springs below the mat foundation are excited by different vertical motions producing rocking of the structure on its base. The current versions of ETABS and SAP2000 can accommodate multiple excitation analysis only if excitations are defined as displacements and not accelerations. Furthermore, if displacement is applied to a node which is part of an integrated system such as a set of interconnected plate

elements representing the mat foundation, only the node excited would move and the other nodes connected to it are not displaced. To get around this issue we devised the modeling scheme presented in Figure 7 where a number of rigid pedestals are introduced at the base. These rigid pedestals are connected to each other at the top by a horizontal rigid plate. The horizontal and vertical ground displacement histories are applied to the bottom end of these rigid pedestals. A set of vertical no-tension springs and dashpots representing vertical soil properties connect this rigid plate to the plate representing the mat foundation above. A series of horizontal no-tension soil springs and dashpots are placed at the edges of the mat foundation and all other subterranean floors as well as the ground floor. The free ends of these springs and dashpots are subjected to the appropriate horizontal ground displacements. Please note that the end displacements imposed on the springs on one side of the building is equal in value and sign to the displacement imposed on the spring at the other side of the building. However, the displacements imposed on different levels are not necessarily the same.

The current version of ETABS (Ver. 9.20) does not offer direct integration as an option. This creates a serious handicap for the SFSI analyses conducted in this study. Nonlinear dynamic analysis in ETABS is conducted via a modified modal analysis technique. Although the nonlinearity in our SFSI analysis is limited to the soil springs (because of the potential for gapping) and therefore could be considered limited in scope, modal analysis poses numerous issues with respect to such analysis. For example, because we are considering the vertical masses and we are modeling the entire gravity system including diaphragms, hundreds of eigenvalues corresponding to individual vibration of floor beams and girders are identified by the program that must be eliminated before the significant structural modes are identified and proper modal damping values are assigned to match recorded motions. Furthermore, extreme care must be taken to ensure that the excited modes include the numerous modes of vibration that should be present to model the behavior of hundreds of soil springs and dampers acting on the basement walls and on the mat foundation. After many trials the only viable solution was to use Ritz vectors instead of eigenvalue analysis in the following manner. First, the vertical masses were ignored and rigid diaphragms were assumed. Eignenvalue analysis was then performed to identify the lateral building modes which had a period of vibration longer than the longest period of vibration of the modes associated with horizontal soil springs. Second, these lateral mode shapes were introduced to the model as a set of Ritz vectors. Third, these Ritz vectors were introduced into the model with vertical masses and floor diaphragms and they were augmented with Ritz vectors representing possible horizontal and vertical displacements of the soil springs and global vertical motion of the building. Fourth, the damping values corresponding to various Ritz vectors were adjusted to match the recorded displacements at the location of sensors.

This modeling technique was successfully used to match recorded displacements throughout the building. However, the accelerations and forces reported by ETABS, particularly at the subterranean levels, were not reliable. As shown in Figure 8, ETABS routinely reported huge acceleration spikes at the first time-step of response history analysis, which was clearly non-physical. This spike is attributed to solution scheme convergence failure. Although this spike could be eliminated by ignoring the results reported for the first time-step of analysis, additional smaller spikes were usually present during the first several seconds of response that we also believe to be non-physical.

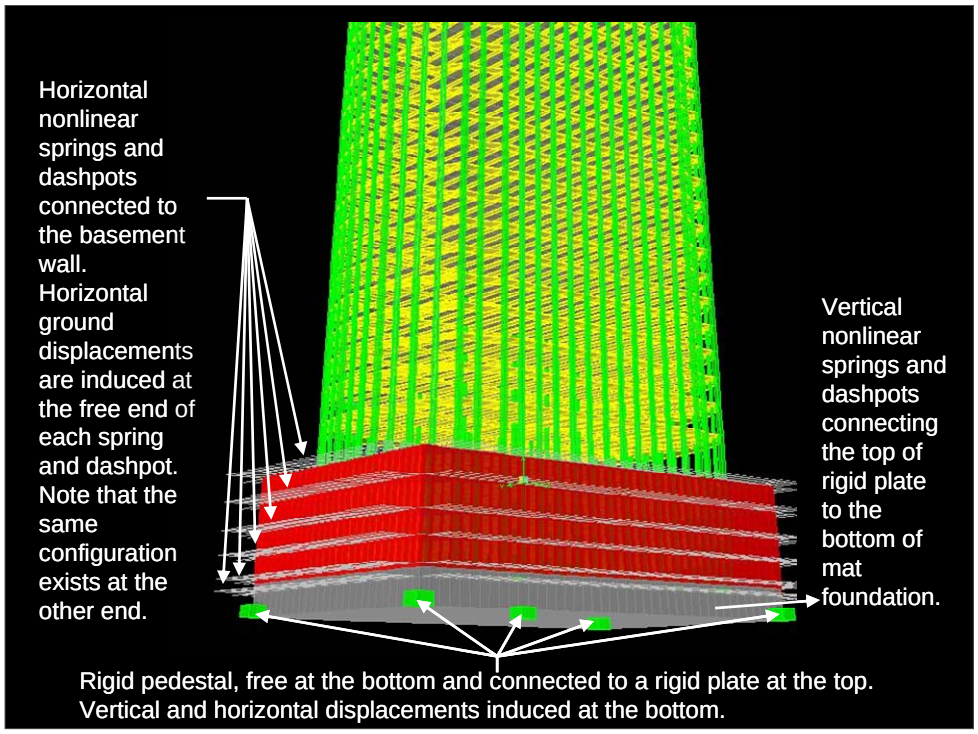

Figure 7. Soil-foundation-structure interaction modeling technique

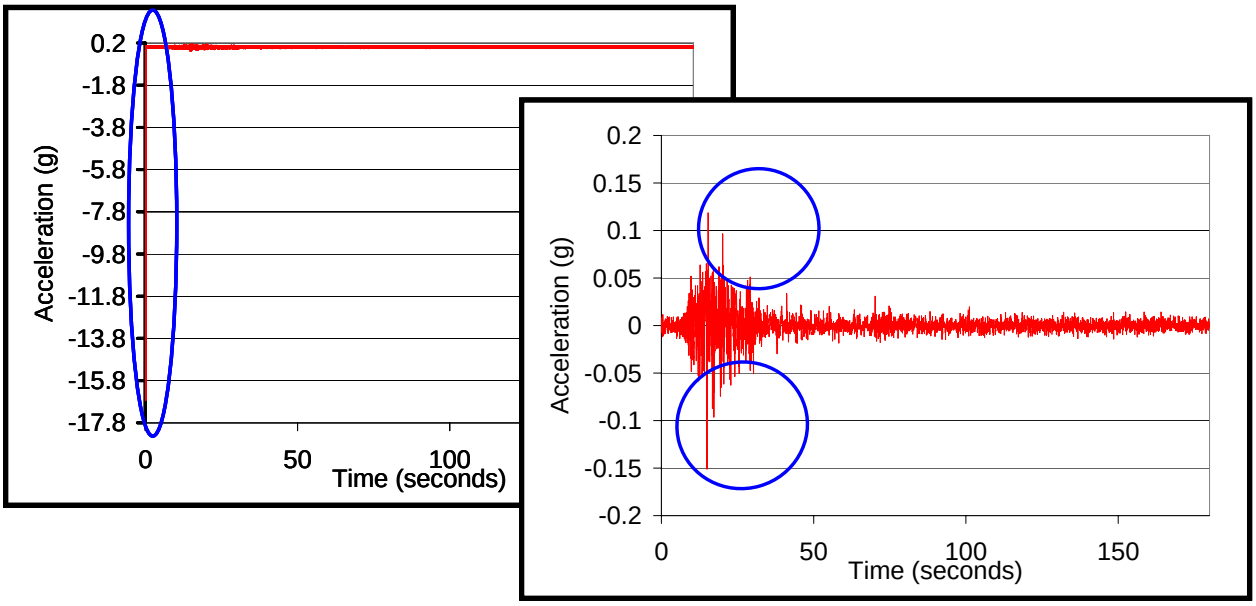

Figure 8. Issues related with computed accelerations obtained from the ETABS model. For models excited with base displacements as shown in Figure 7, ETABS reports an erroneous and huge acceleration spike at the first time step of response-history analysis (see trace to the left). If the spike at the first time step is removed, the trace shown on the right is obtained which still contains smaller spikes which in our opinion are not real and are caused by solution instability.

5.0 Results

6.1 Results for the MA Model

The best match of MA model to recordings was obtained with all modal damping values set to 1.0% of critical except for modes 1 and 4 where the damping values were set to 1.8%. The same damping values were used for all approximations. A summary of 50 Ritz vectors provided a level of accuracy that did not improve by inclusion of more vectors (up to 300 Ritz vectors were utilized to see if there is any significant difference in the results). A summary of the first five periods associated with Ritz vectors for various models is presented in Table 3. As indicated by Table 4 all five computed periods are very close to those identified from recorded data using the CSMIP-3DV software (Naeim, et al. 2005; 2006).

Table 3. Summary of periods associated with the first five Ritz vectors for various models.

Model	Reported vibration periods for first five Ritz vectors (sec.)				
	1	2	3	4	5
MA*	6.06	5.18	2.76	1.92	1.81
1	6.03	5.15	2.75	1.91	1.81
2A	6.06	5.18	2.76	1.92	1.81
2B	6.06	5.18	2.76	1.92	1.81
2C	6.06	5.18	2.76	1.92	1.81
3A	6.04	5.18	2.78	1.92	1.82
3B	5.79	4.99	2.76	1.92	1.82
3C	5.79	4.99	2.76	1.92	1.82
3D	5.63	4.90	2.74	1.89	1.80

Table 4. Comparison of MA model periods and those obtained from system identification

Direction	Identified Periods (sec.)		MA Model Periods (sec.)	
	Mode 1	Mode 2	Mode 1	Mode 2
E-W	6.07	1.95	6.06	1.92
N-S	5.12	1.86	5.18	1.81
Torsional	2.78		2.76	

Displacement histories obtained from the calibrated MA model are compared to recordings in Figure 9. Excellent agreement between recorded and computed vertical and horizontal displacements at the P-4 level (above the mat) may be observed in Figures 9a to 9d. The match in both horizontal directions at the ground level is also virtually perfect (Figures 9e and 9f). Elsewhere over the height of the building the quality of the match is generally better in the E-W direction than in the N-S direction. However, the matching of both maximum amplitudes and phasing are very good in both directions.

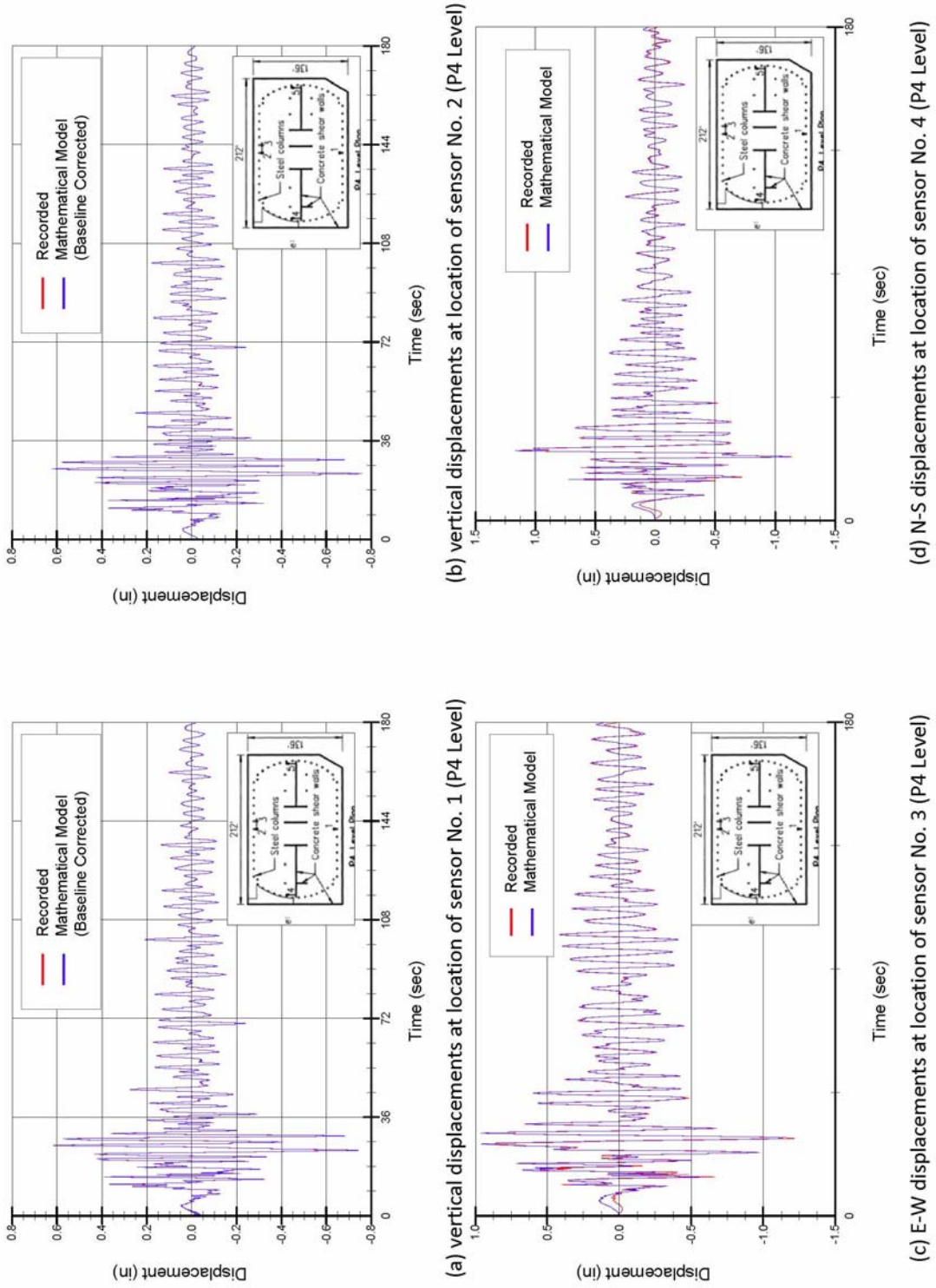

Figure 9. Comparison of recorded displacements with those computed for the MA model

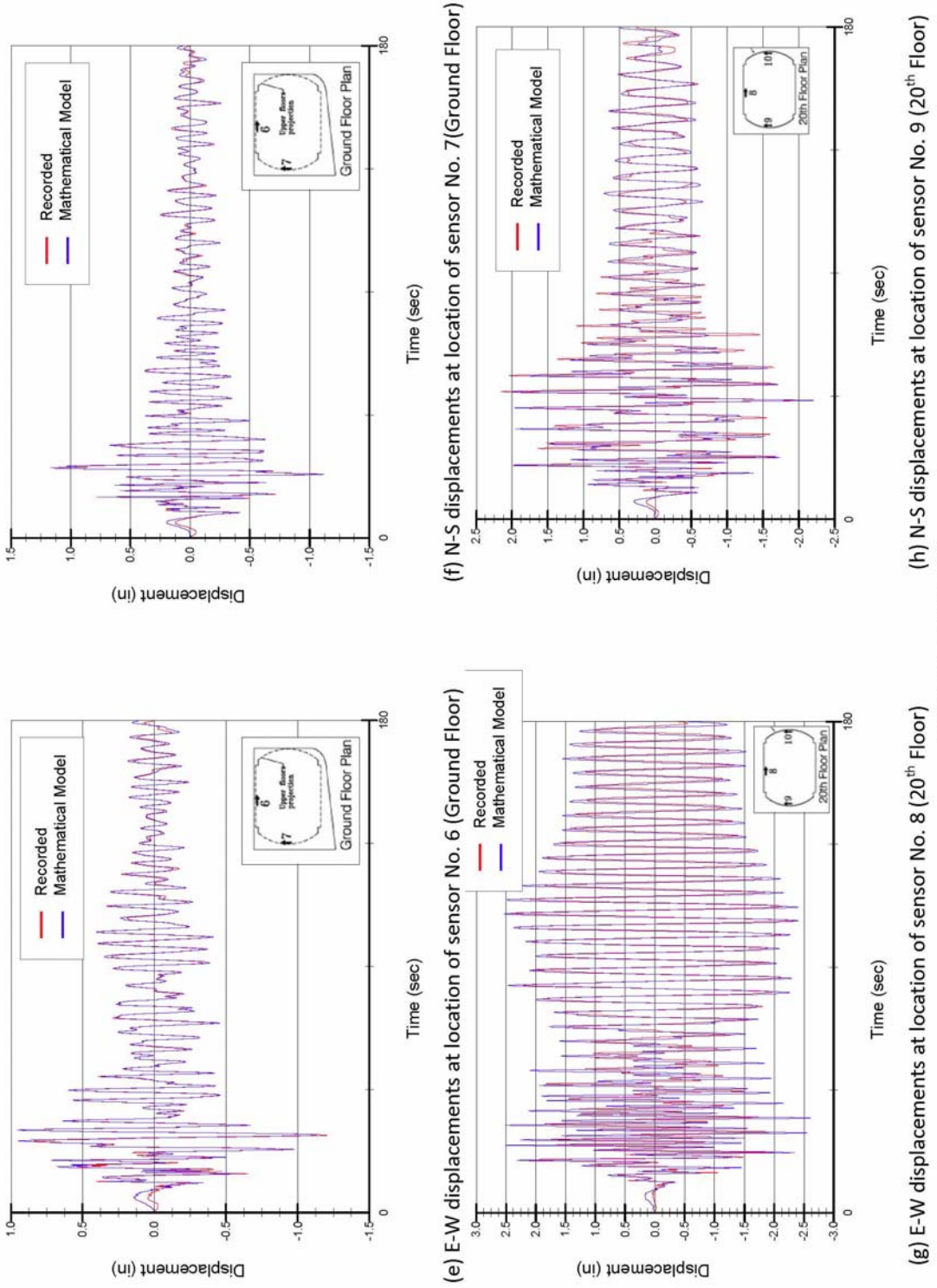

Figure 9. Continued

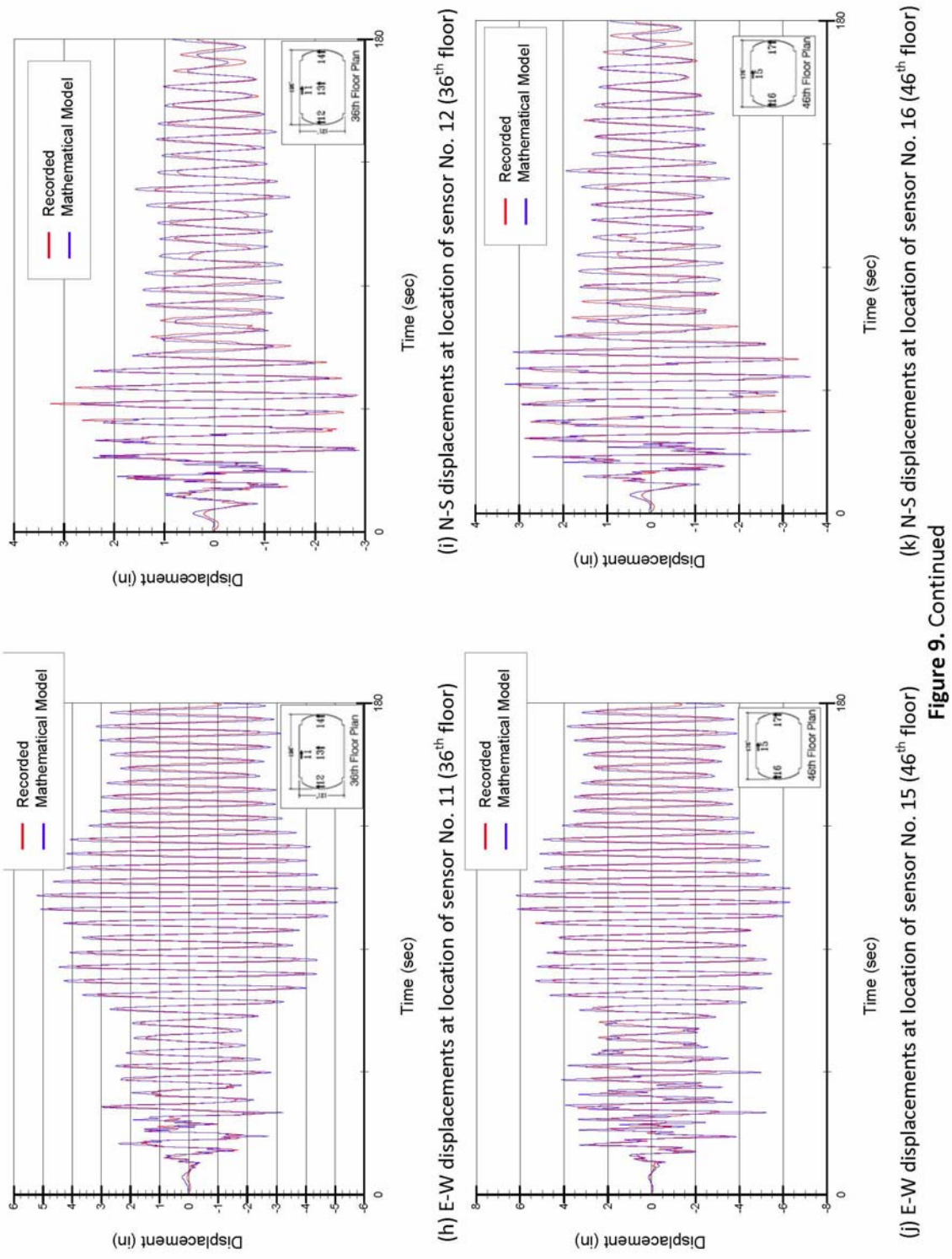

(h) E-W displacements at location of sensor No. 11 (36th floor)

(i) N-S displacements at location of sensor No. 12 (36th floor)

(j) E-W displacements at location of sensor No. 15 (46th floor)

(k) N-S displacements at location of sensor No. 16 (46th floor)

Figure 9. Continued

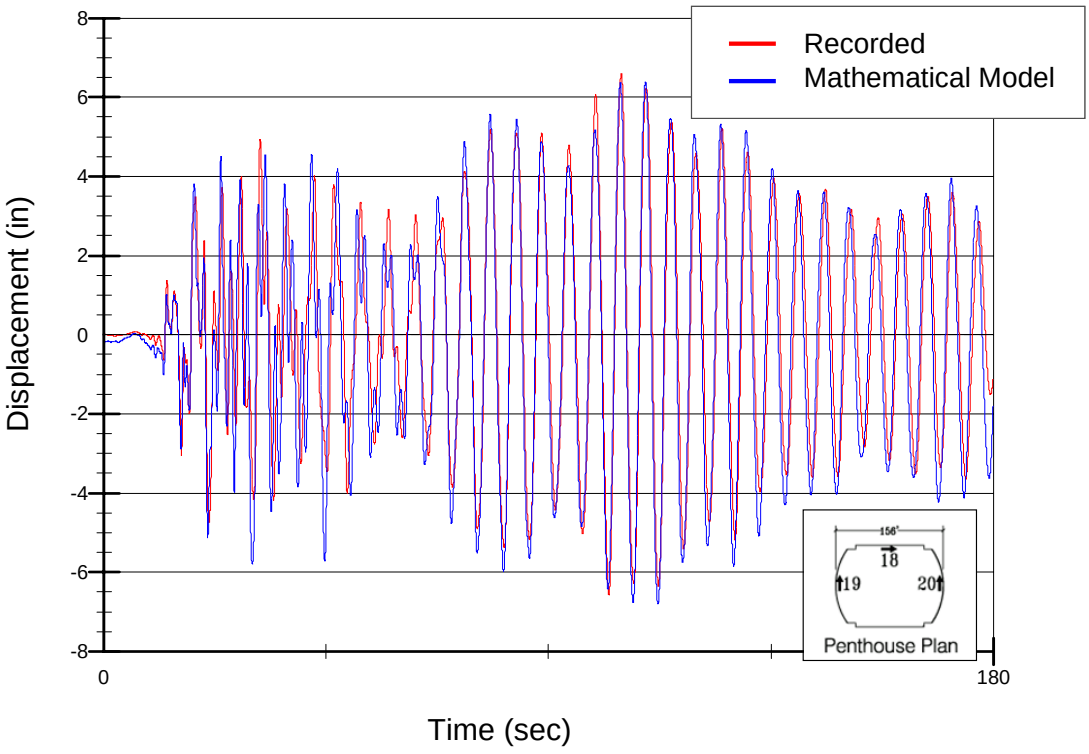

(l) E-W displacements at location of sensor No. 18 (Penthouse)

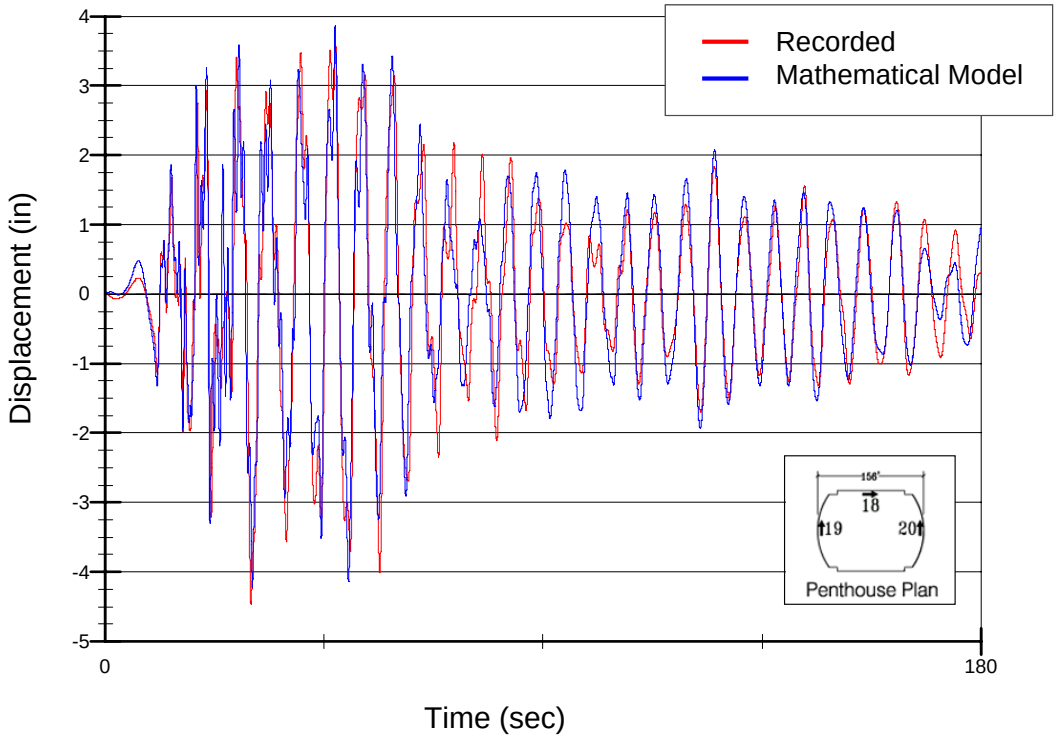

(m) N-S displacements at location of sensor No. 19 (Penthouse)

Figure 9. Continued

6.2 Results for Selected Approximations

Our analyses of the models that are simplified relative to MA are presented relative to the MA results instead of the recordings. This allows for a direct comparison of impact of changes in model attribute.

Allowing tension in the soil with no other changes (Model 3A) does not affect the results by much. Table 3 shows that the building vibration periods are very slightly affected and Figure 10 shows the errors induced in displacement history response throughout the height are negligible (e.g., less than 4% at roof level). As illustrated in Figure 11, error in maximum story drift ratios for floors above ground level are less than 10% and 5% in the E-W and N-S directions, respectively. The error in the maximum interstory drift ratios for subterranean floors are significantly larger at about 32% in the E-W direction and 46% in the N-S direction.

Ignoring the subterranean levels by assuming a rigid base at ground level (Model 3D) significantly alters the vibration periods of the building (see Table 3). As a result, many of the displacement history responses are out of phase with those of obtained for the MA model (see Figures 12b to 12d). The roof peak displacement in the E-W direction for the MA and 3D models while having similar amplitude occurs at very different times during the response (Figure 12c). The error in peak roof displacement is less than 20% (Figures 13a and 13b). Interestingly, the distribution of interstory drifts over the height of the structure is also significantly affected, with drifts increasing at lower levels and decreasing at higher levels of the building for Model 3D relative to MA.

Fixing the far ends of horizontal soil springs, and subjecting these fixed ends to free-field ground accelerations (Model 3B) is one of the two common methods used by engineering offices to bound the SFSI problem. As shown in Table 3, this approximation also significantly affects the dynamic characteristics of the model by shortening its period because the fixed-end springs provide more resistance to the below-ground structure. As shown in Figure 14a-b,the ground level displacements reported by this approximation are negligible compared to those reported by the MA model. Note that in this model the ground accelerations are used as input and ETABS does not calculate the displacements at the fixed ends of the horizontal springs. Therefore, the displacements reported at the ground line consist only of the in-plane displacements of the ground floor diaphragm which are very small. Figures 14c-d show that the displacement histories at roof level are very different from those obtained from MA model. Note that the peak roof displacement in the E-W direction happens to be close to that twice that of the MA model. This is reflected in the maximum displacement and drift charts presented in Figure 15 where the results in the E-W direction look deceptively close to that of MA model while the results in the N-S direction vary sharply from those obtained from the MA model.

Ignoring the embedment effect by running the structure down to the foundation level and ignoring the horizontal stiffness of the surrounding soil is another common assumption that is used in design offices to bound the SFSI problem (Model 3C). Many engineers will be surprised to see that the 3C model is stiffer and has a shorter fundamental period than the MA model (Table 3). As shown in Figure 16, the displacement time histories at the ground floor for the 3C and MA model are virtually identical (Figure 16)). The error in maximum roof displacement is small at less than 5% and 10% in E-W and N-S directions. Figure 17 shows that as with Model

3D, Model 3C story drift ratios increase relative to MA at lower levels of the building, although this effect is principally in the E-W direction.

If we retain all MA model characteristics but assume foundation structural elements (i.e, mat and basement walls) to be rigid (Model **1**), building periods are practically unaffected, as shown in Table 3. Figures 18a-b show that the displacement histories at the ground floor for the **1** and MA model are virtually identical. The frequency match with the MA model results for the displacement histories for are good throughout the height of the building. However, Model **1** overestimates the displacements of the upper portions of the building in the E-W direction in the first one-third of the response duration where the peak displacement in this direction occurs (Figure 18c) resulting in an overestimation of the maximum roof displacement in this direction by about 25% (Figure 19a). In the N-S direction, the reverse occurs. That is, the displacement amplitudes in the early part of the response where peak displacement occurs is very close to those obtained from the MA model but in the later part of the response Model **1** underestimates the amplitude of displacements (Figure 18d). As a result, the maximum story displacements in the N-S direction are much closer to the values reported by the MA model. The maximum error for displacements in this direction is less than 8%. The maximum error in interstory drifts in the E-W direction occurs at the 22nd floor and is about 28%. The maximum interstory drift errors at above ground floors in the N-S direction are significantly smaller at less than 5%. However, the same error in the subterranean levels in the N-S direction is significantly larger in the N-S direction compared to the E-W direction (65% compared to 20%).

Elimination of kinematic base rocking with no other changes (Model 2A) has negligible effect on the vibration periods of the building (Table 3). Moreover, as shown in Figure 20, the maximum displacements and interstory drifts throughout the height of the building, with the exception of subterranean drifts, are almost identical.

Eliminating kinematic loading from relative soil displacements adjacent to basement walls (Model 2B) virtually affects nothing as the displacement and inter-story drift histories and maximum values are nearly identical to those obtained from the MA model (Figure 21).

Finally, ignoring kinematic interaction effects on the base horizontal motion (Model 2C) produces results which are virtually identical to the MA model at all floor above the ground level (Figure 22). However, use of Model 2C results in significant underestimating of maximum interstory drifts in the subterranean levels (Figures 22c and 22d).

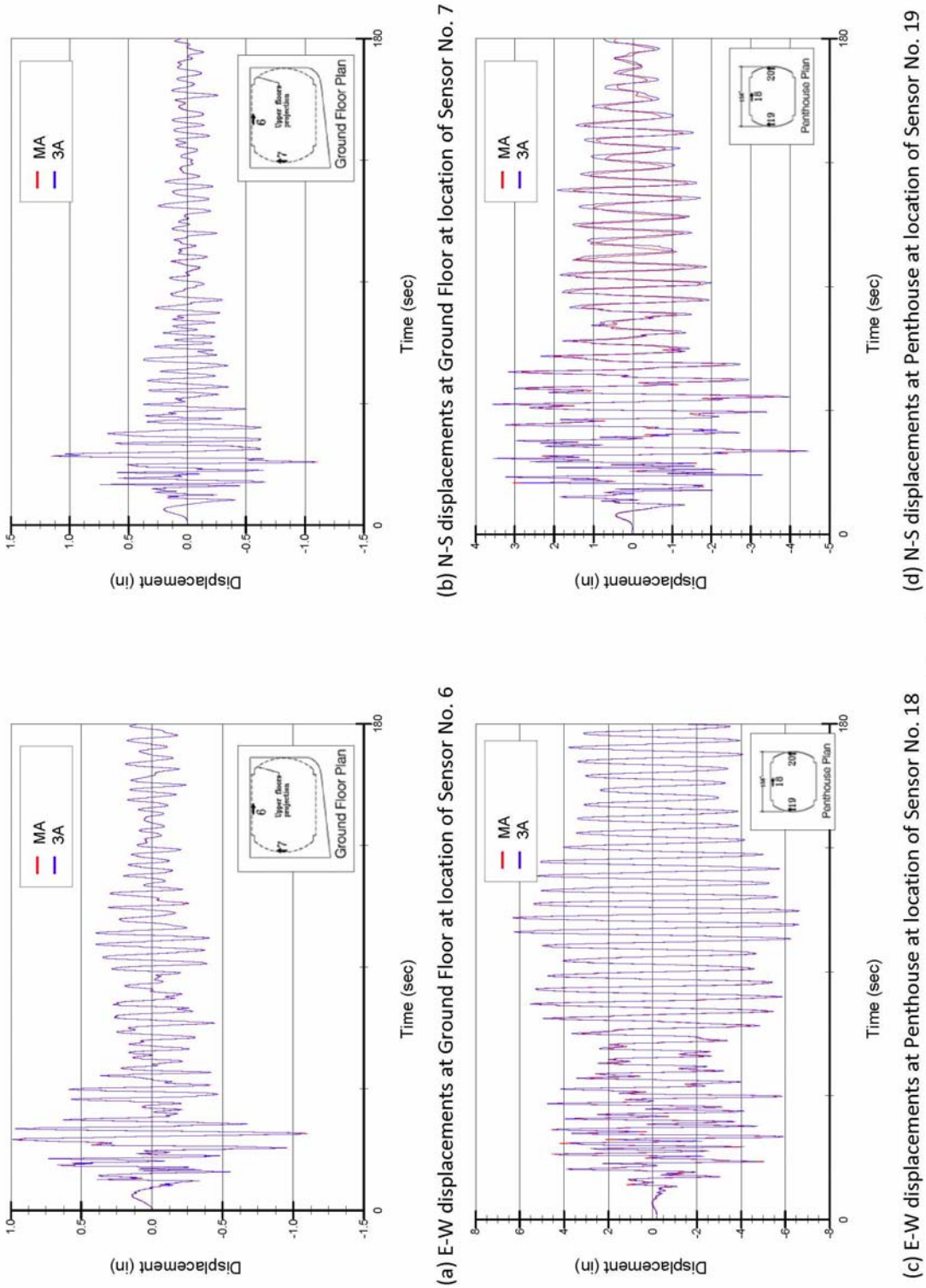

Figure 10. Comparison of displacement histories obtained from the MA and 3A models

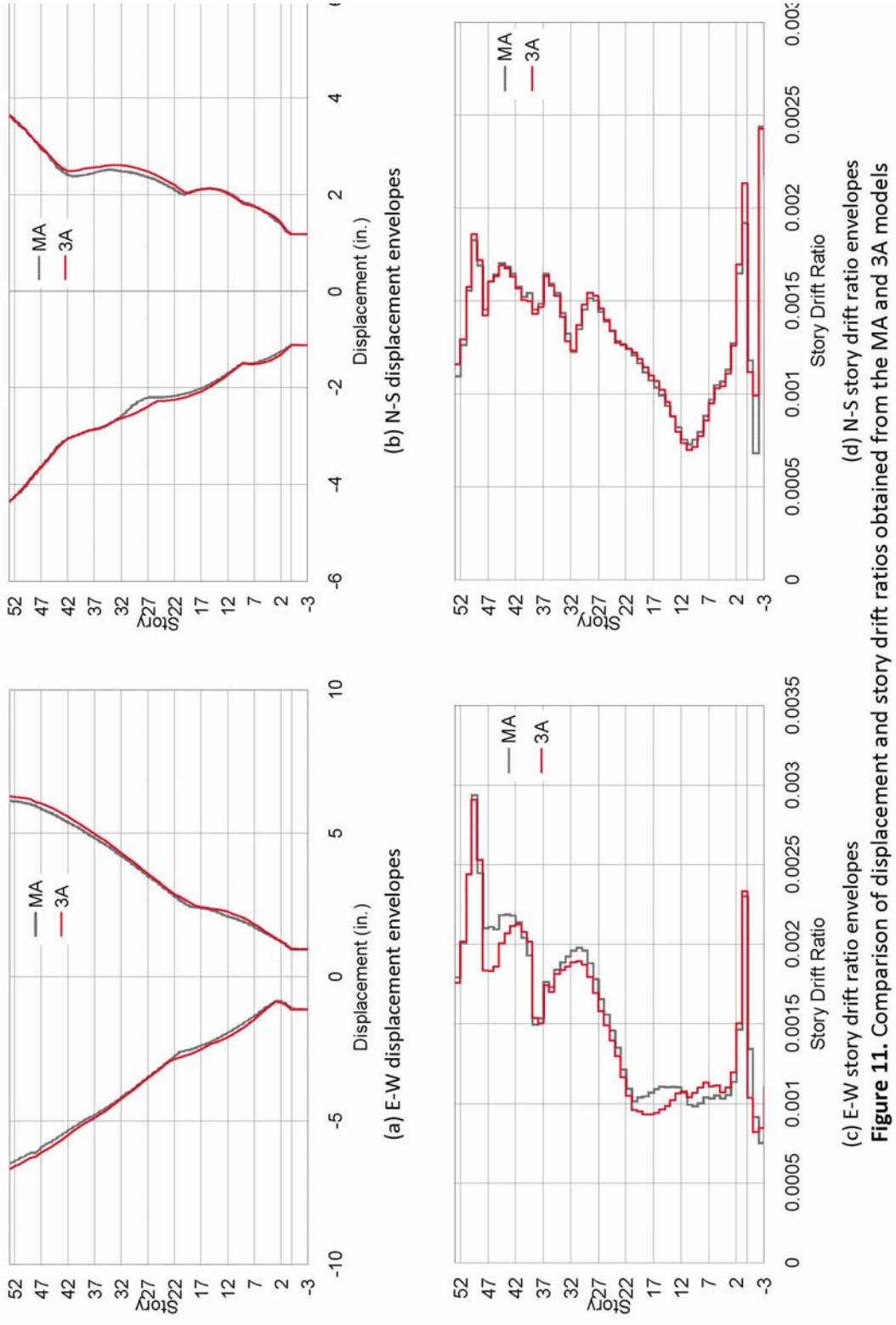

Figure 11. Comparison of displacement and story drift ratios obtained from the MA and 3A models

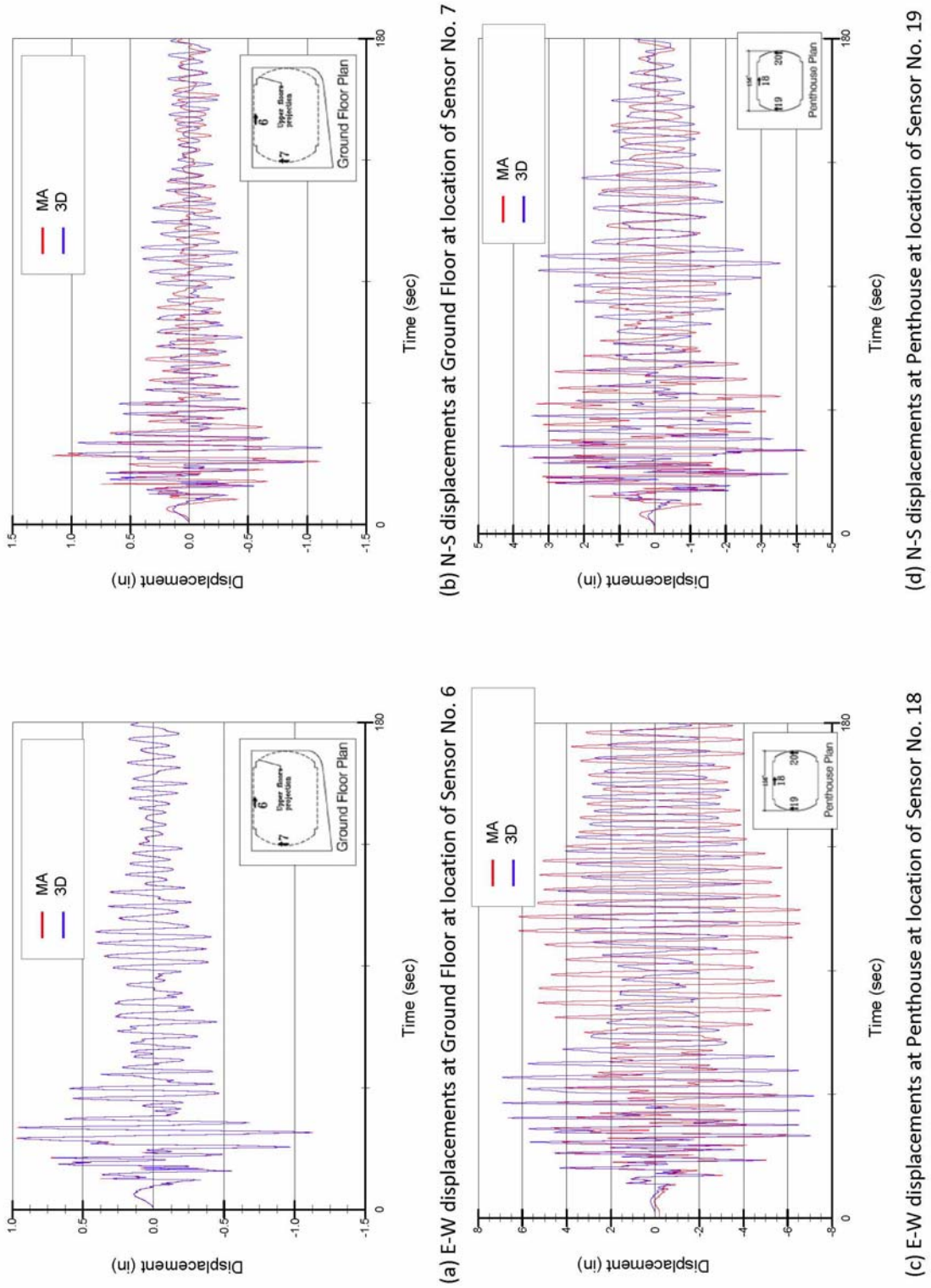

Figure 12. Comparison of displacement histories obtained from the MA and 3D models

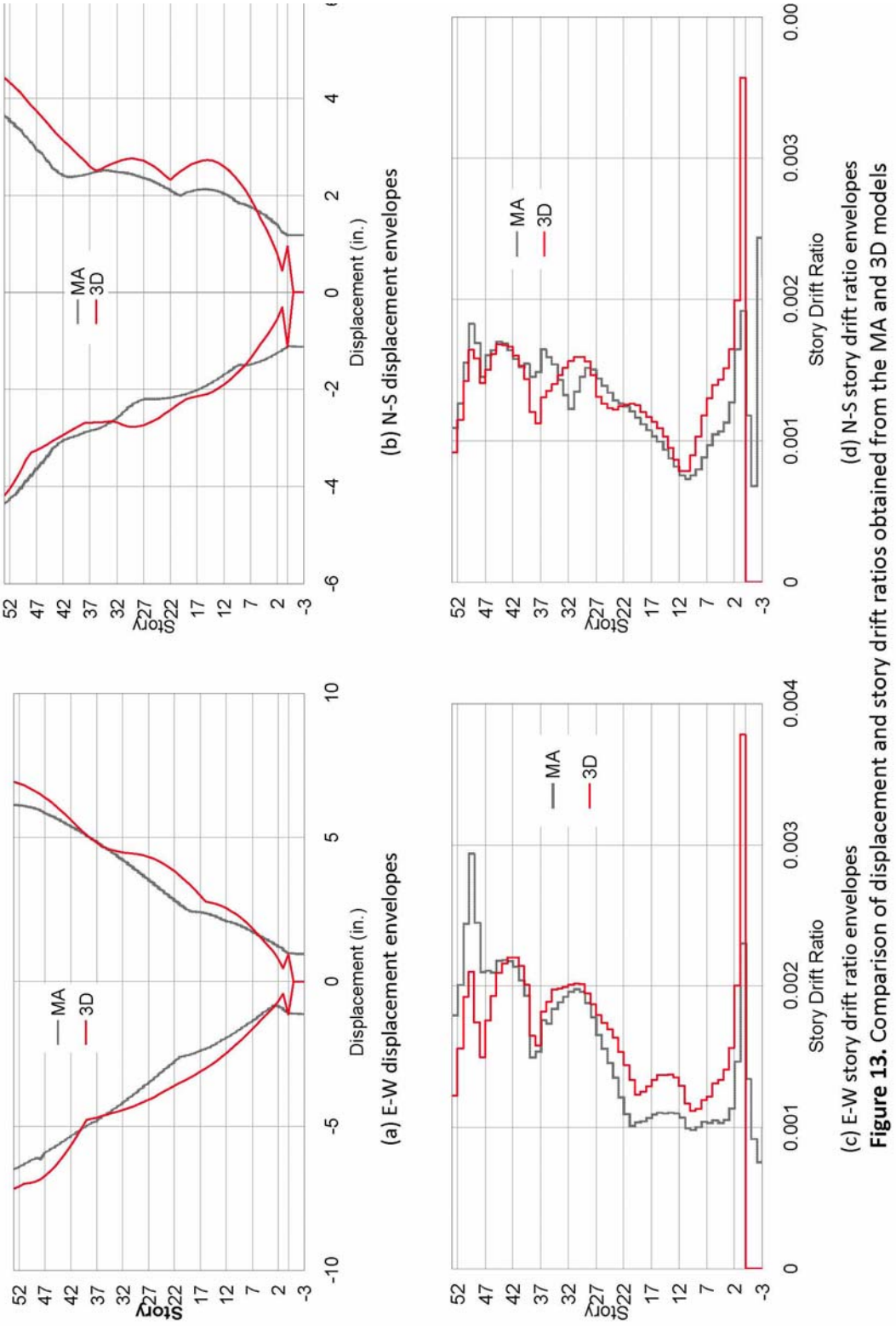

Figure 13. Comparison of displacement and story drift ratios obtained from the MA and 3D models

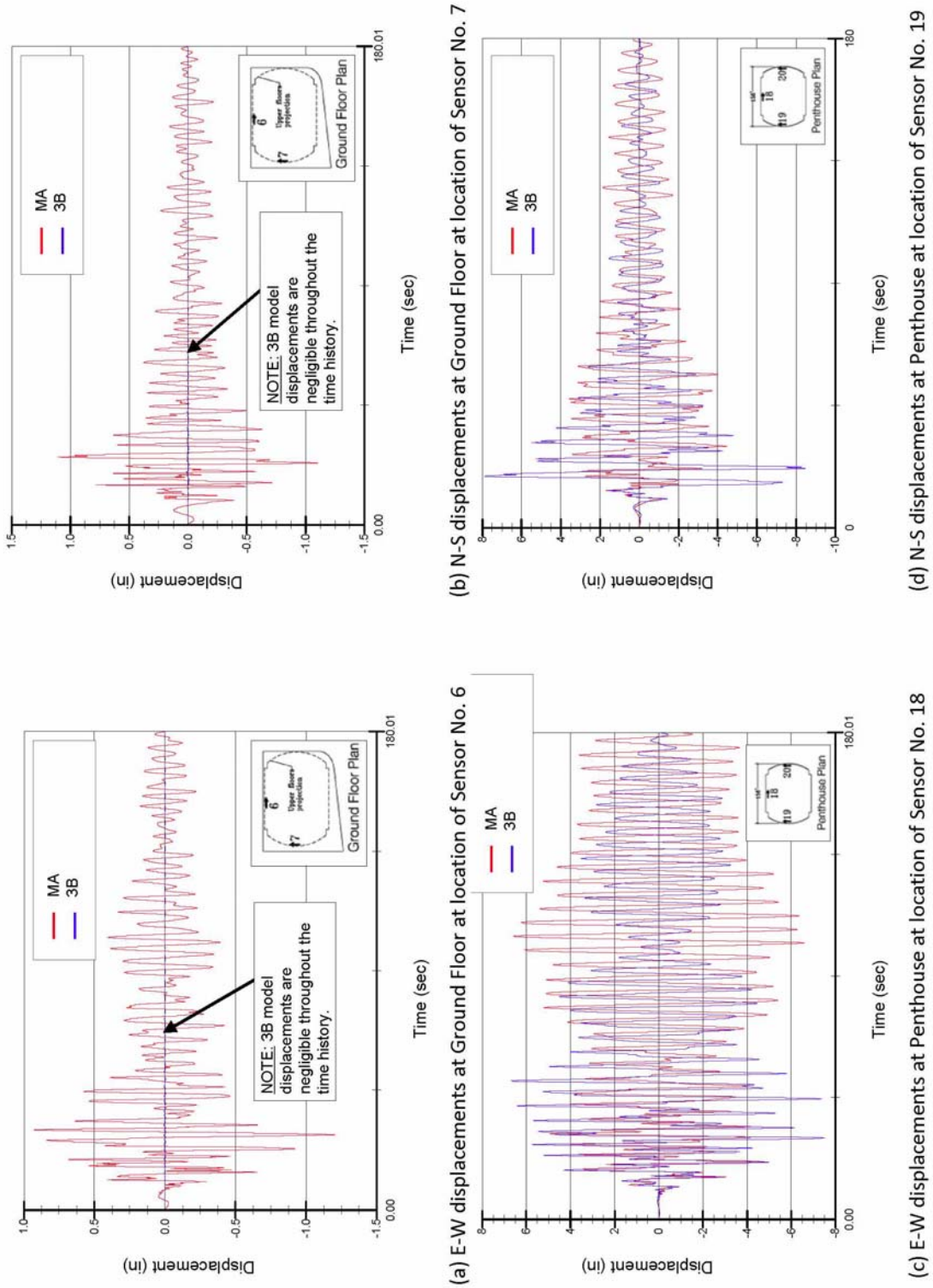

Figure 14. Comparison of displacement histories obtained from the MA and 3B models

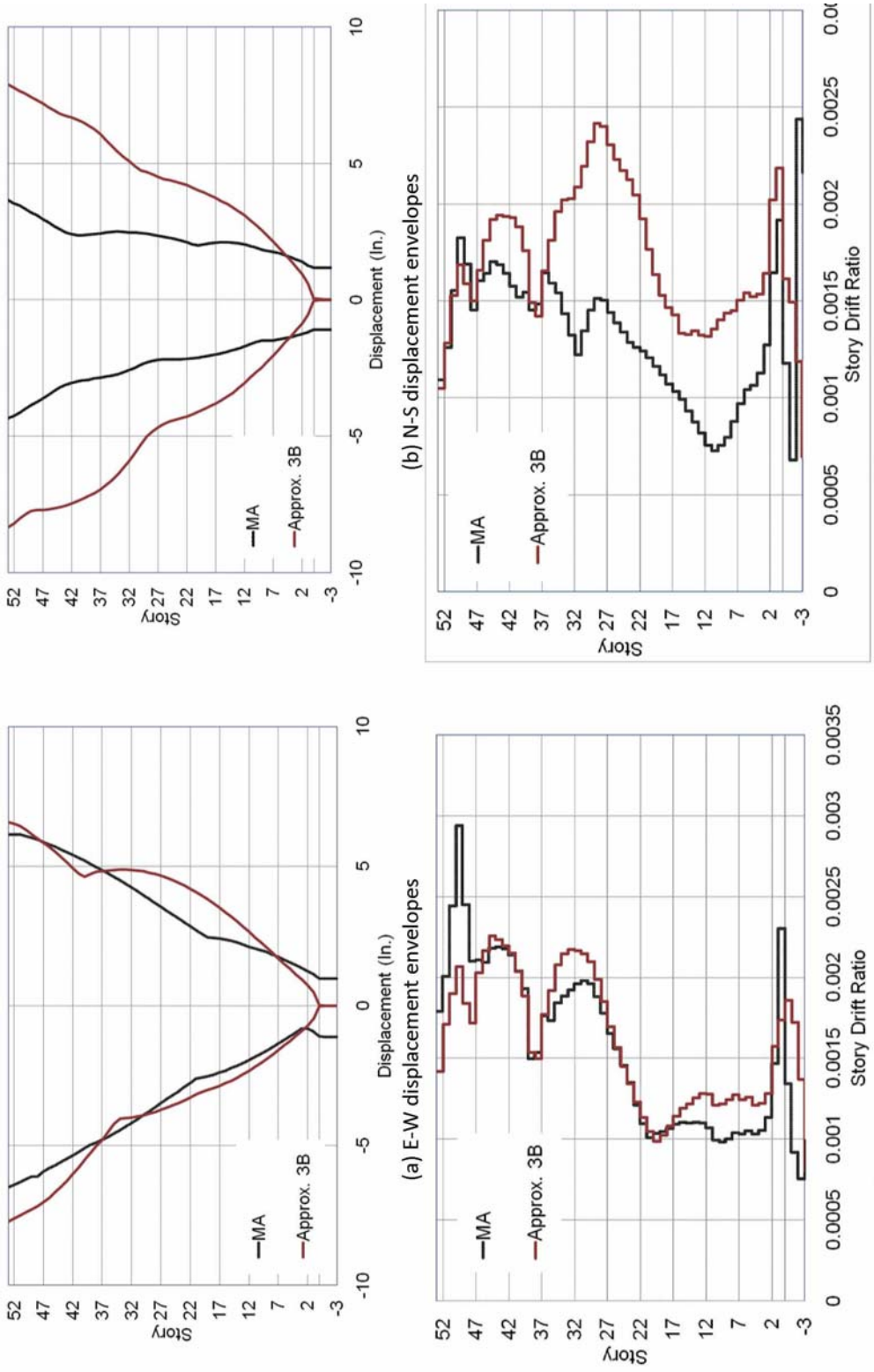

Figure 15. Comparison of displacement and story drift ratios obtained from the MA and 3B models

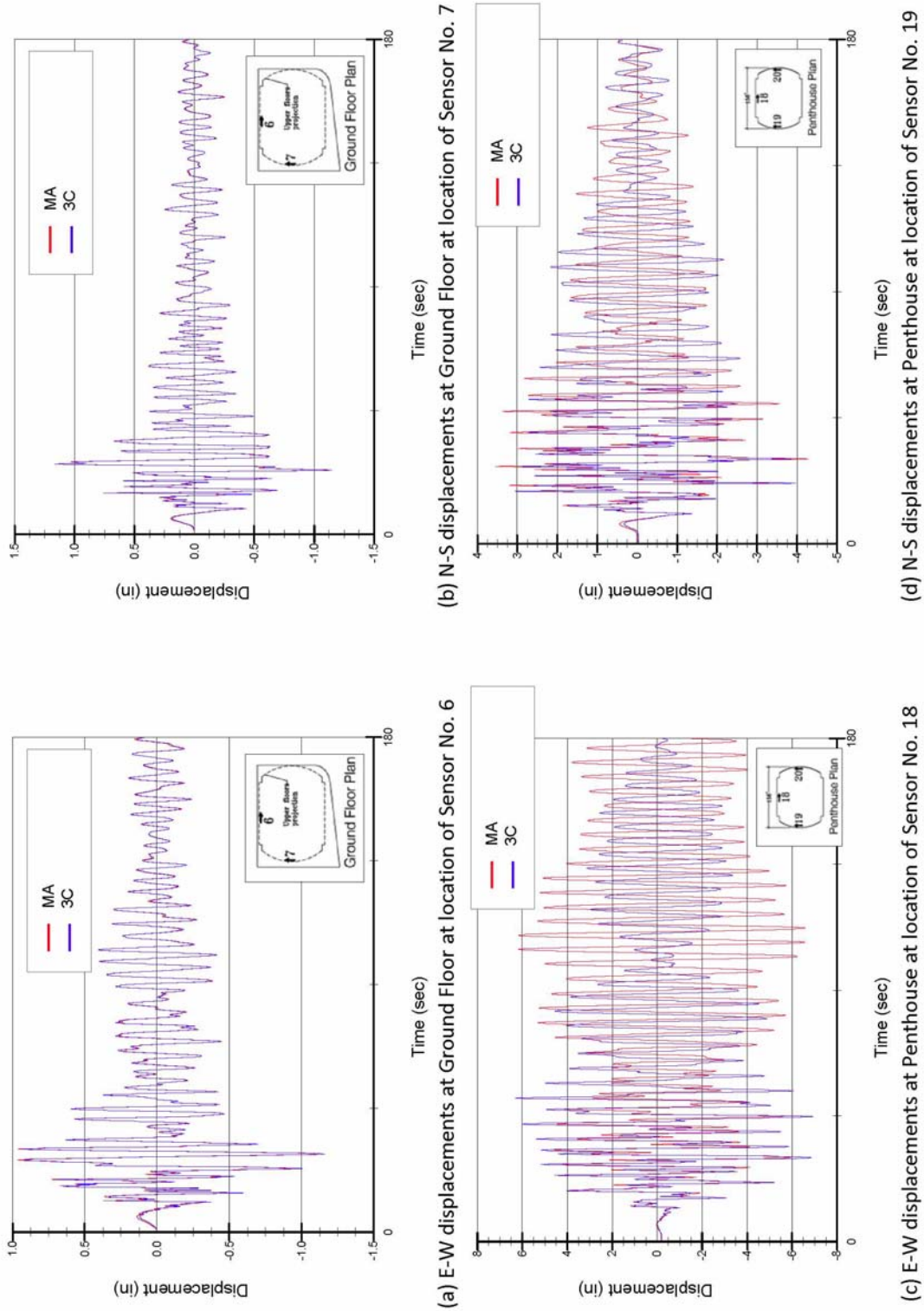

Figure 16. Comparison of displacement histories obtained from the MA and 3C models

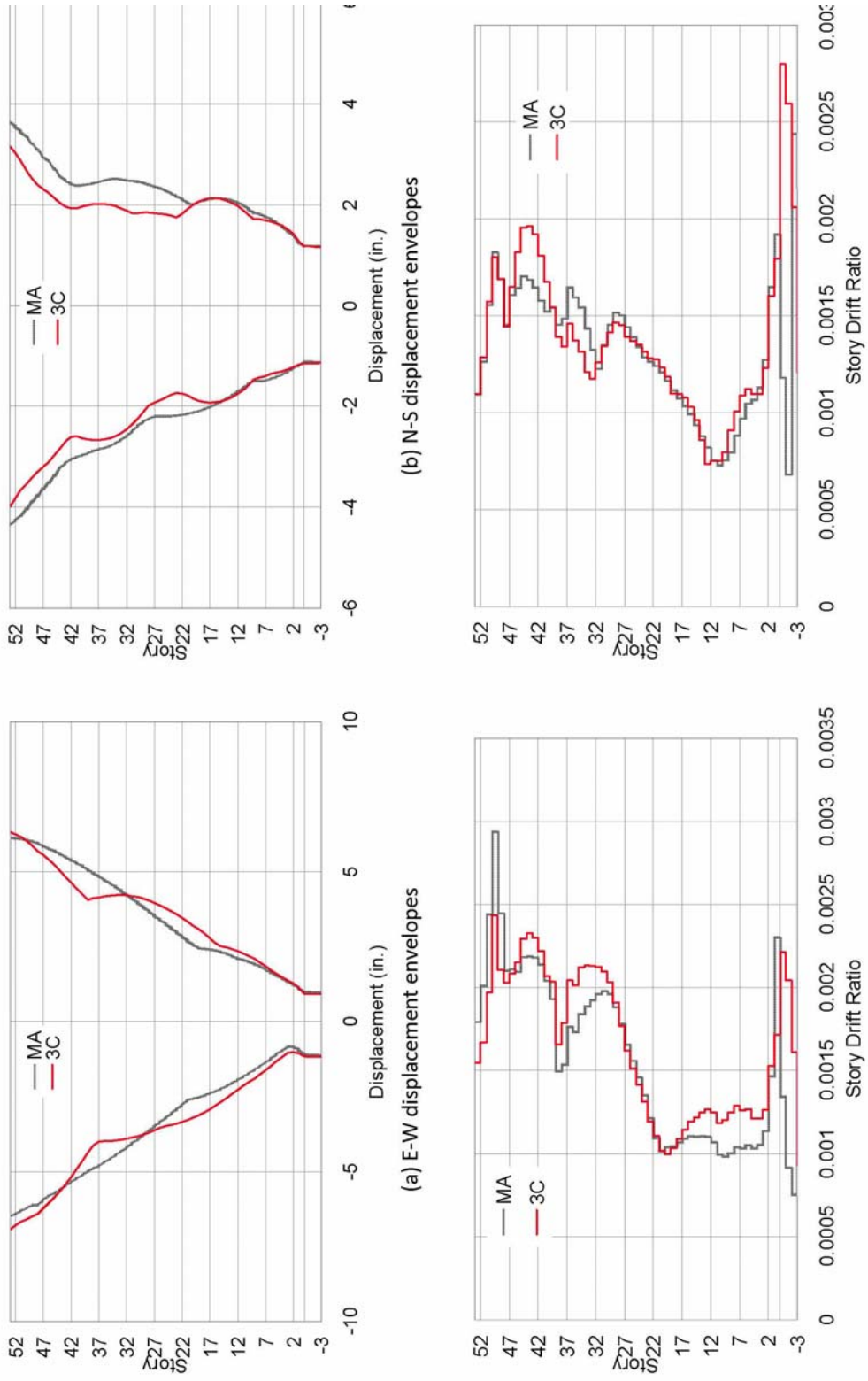

Figure 17. Comparison of displacement and story drift ratios obtained from the MA and 3C models

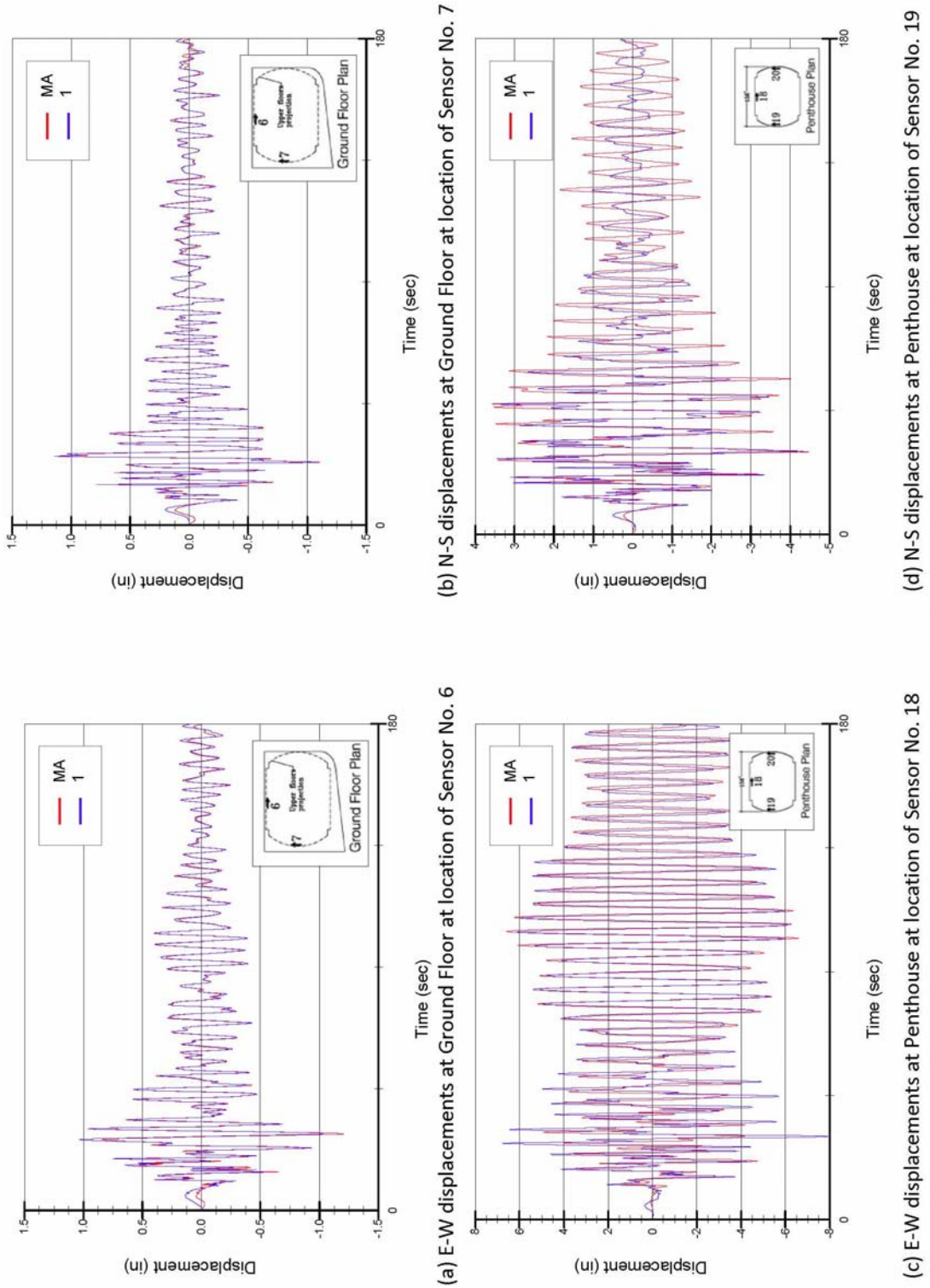

Figure 18. Comparison of displacement histories obtained from the MA and **1** models

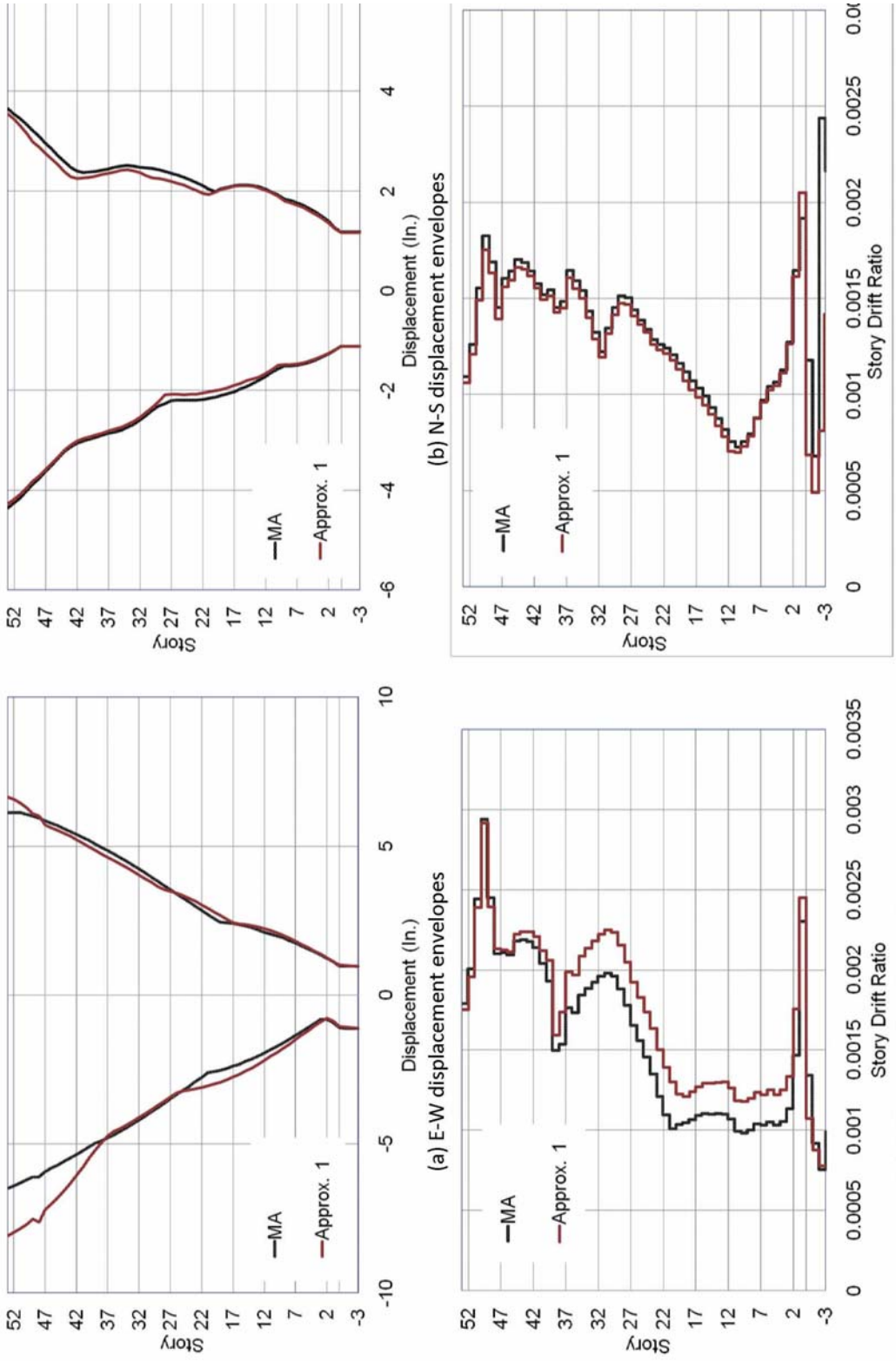

Figure 19. Comparison of displacement and story drift ratios obtained from the MA and **1** models

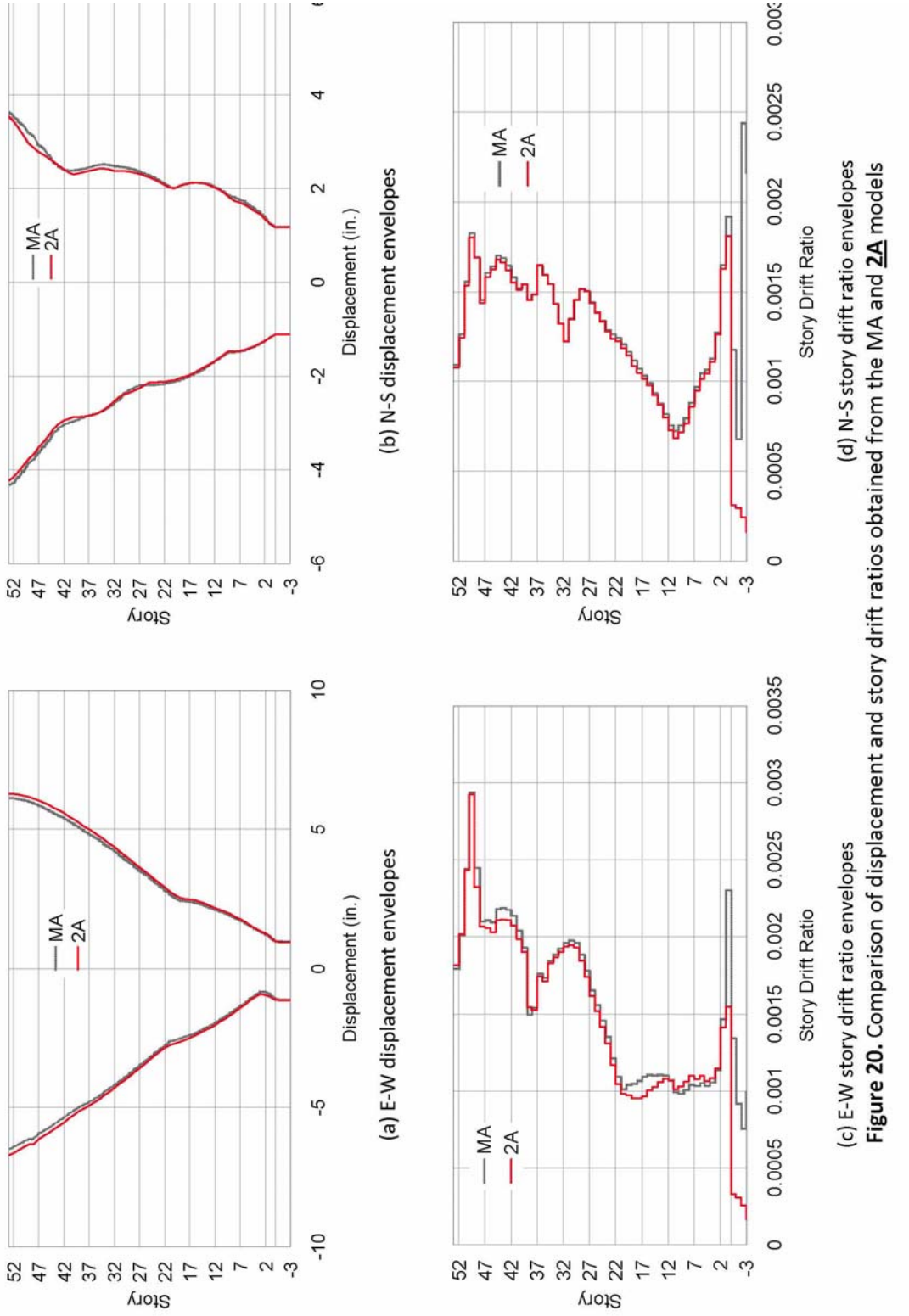

Figure 20. Comparison of displacement and story drift ratios obtained from the MA and **2A** models

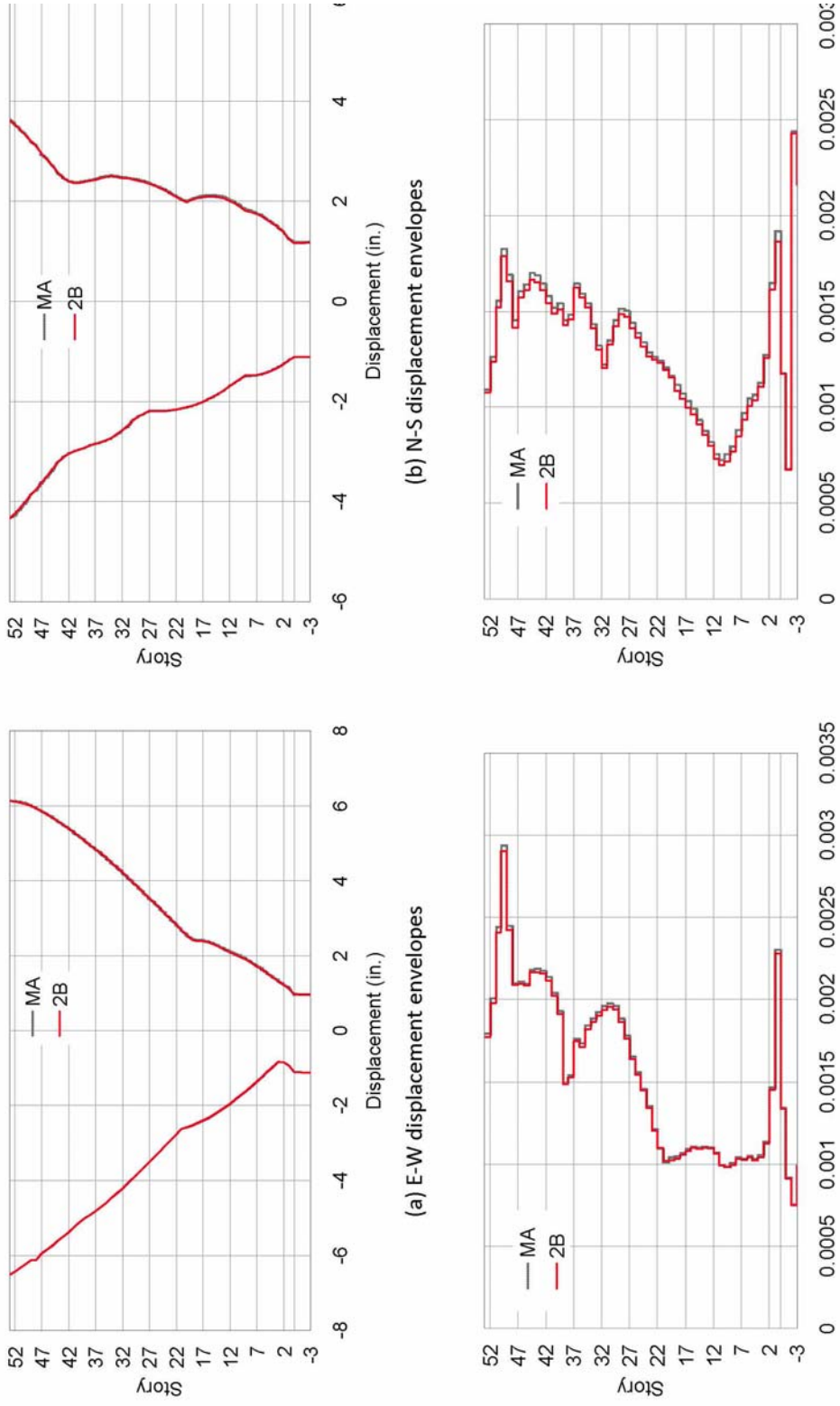

Figure 21. Comparison of displacement and story drift ratios obtained from the MA and **2B** models

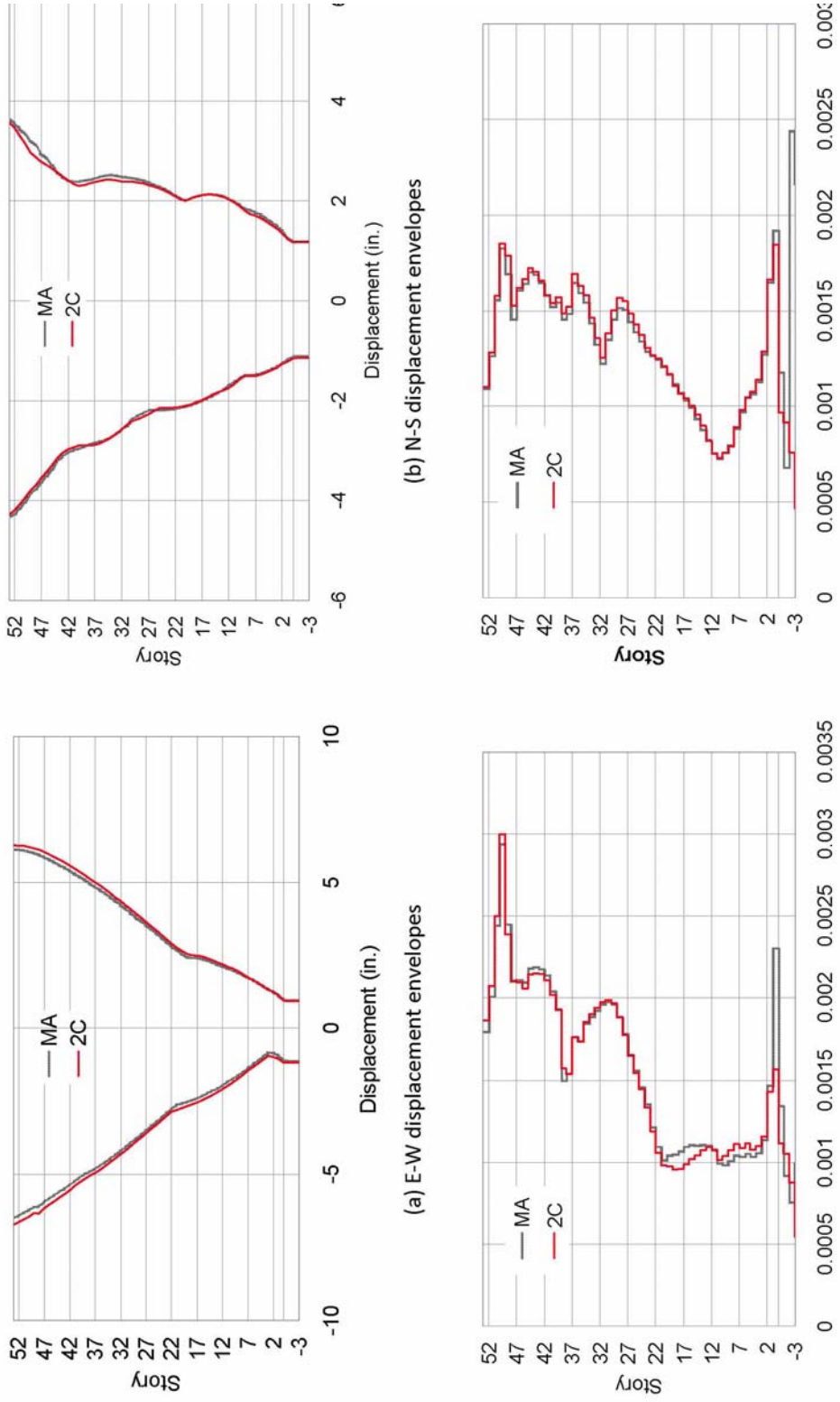

Figure 22. Comparison of displacement and story drift ratios obtained from the MA and **2C** models

7.0 Summary and Conclusions

Soil-structure interaction can affect the response of buildings with subterranean levels by modifying the characteristics of input motions relative to those in the free-field and through the added system compliance associated with relative foundation/free-field translation and rocking. While procedures are available to account for these effects, they are seldom utilized in engineering practice. Our objective is to examine the importance of these effects on the seismic response of a 54 story building with four subterranean levels. We first generate a "most accurate" (MA) model that accounts for kinematic interaction effects on input motions, depth-variable ground motions along basement walls, compliant structural foundation elements, and soil flexibility and damping associated with translational and rocking foundation deformation modes.

With reasonable tuning of superstructure damping, the MA model accurately reproduces the observed response to the 1994 Northridge earthquake. While the MA modeling exercise was ultimately successful, the process highlighted several major hurdles to the implementation of soil-structure interaction effects in practice for these types of structures. The principal implementation problems are lack of a direct integration scheme in ETABS and existence of nonphysical acceleration spikes in the acceleration results. These could be rather easily solved by code developers and we are told that such corrections are forthcoming in the near future.

We remove selected components of the MA model one-by-one to test their impact on building response. Factors found to generally have a modest effect on building response above ground level include compliance of structural foundation elements, kinematic interaction effects (on translation or rocking), and depth-variable ground motions applied to the ends of horizontal soil springs/dashpots. However, those factors did generally affect below-ground response as measured by interstory drift.

Properly accounting for foundation/soil deformations does not significantly affect vibration periods for this tall building (which is expected), but does impact significantly the distribution of inter-story drifts over the height of the structure. To our knowledge, the latter observation is new to this study.

Two approximations commonly used in practice are shown to provide poor results: (1) fixing the structure at ground line with input consisting of free-field translation and (2) fixing the structure at the base level, applying free-field motions as input at the base level, and using horizontal foundation springs along basement walls with their end condition fixed to the free-field ground motion.

References

Chajes, M. J. Finch, W. W., Jr., and Kirby, J. T. (1996). "Dynamic analysis of a ten-story reinforced concrete building using a continuum model," *Computers & Structures*, 58 (3), 487-498.

Computers and Structures, 2008, *ETABS version 9 User Manuals*, Berkeley, CA.

EPRI, Electrical Power Research Institute (1993). "Guidelines for determining design basis ground motions. Volume 1: Method and guidelines for estimating earthquake ground motion in eastern North America," *Rpt. No. EPRI TR-102293*, Palo Alto, CA.

Idriss, I.M. and Sun, J.I. (1992). "SHAKE91: A computer program for conducting equivalent linear seismic response analyses of horizontally layered soil deposits," Center for Geotech. Modeling, Univ. of California, Davis.

Kim, S. and Stewart, J.P. (2003). "Kinematic soil-structure interaction from strong motion recordings," *J. Geotech.. & Geoenv. Engrg.*, ASCE, 129 (4), 323-335.

Kunnath, S. K., Nghiem, Q., and El-Tawil, S. (2004). "Modeling and Response Prediction in Performance-Based Seismic Evaluation: Case Studies of Instrumented Steel Moment-Frame Buildings," *Earthquake Spectra*. 20 (3), 883-915.

LeRoy Crandall Associates, LCA (1981). "Report of Geotechnical Investigation, Proposed High Rise Development, Bounded by Harbor Freeway and 7th, 8th, and Figueroa Street, Los Angeles, California," *Job. No. ADE-81040.*

Liu, H., Yang, Z., and Gaulke, M. S. (2005). "Structural identification and finite element modeling of a 14-story office building using recorded data," *Engineering Structures*, 27 (3), 463-473.

Mylonakis, G., Gazetas, G., Nikolaou S., and Chauncey, A. (2002). "Development of Analysis and Design Procedures for Spread Footings" Technical Rpt MCEER-02-0003, City University of New York and the University of Buffalo, State University of New York, 246 pgs.

Naeim, F., Lee, H, Hagie, S., Bhatia,H. And Skliros, K. (2005), *CSMIP-3DV Technical Manual*, John A. Martin & Associates, Inc, Los Angeles, CA.

Naeim, F., Lee, H, Hagie, S., Bhatia,H., Alimoradi,A. and Miranda, E. (2006), "Three-dimensional analysis, real-time visualization, and automated post-earthquake damage assessment of buildings," *The Structural Design of Tall and Special Buildings*, 15, 1, pp. 105-138, Wiley InterScience, London.

PEER, 2008, Open system for earthquake engineering simulation (OpenSees) – development platform by the Pacific Earthquake Engineering Research Center (PEER). *http://opensees.berkeley.edu/.*

Seed, H.B. and Idriss, I. M. (1970). "Soil moduli and damping factors for dynamic response analyses," *Report EERC 70-10*, Earthquake Engineering Research Center, University of California, Berkeley.

Stewart, J.P. and Stewart, A.F. (1997). "Analysis of soil-structure interaction effects on building response from earthquake strong motion recordings at 58 sites," *Rpt. No. UCB/EERC-97/01*, Earthquake Engineering Research Center, University of California, Berkeley, February, 742 pgs.

Stewart, J.P. and Tileylioglu, S. (2007). "Input ground motions for tall buildings with subterranean levels," *Structural Design of Tall and Special Buildings*, 16(5), 543-557.

SOME MILESTONES IN STRONG MOTION MONITORING

W. D. Iwan

California Institute of Technology

Summary

This presentation describes some significant milestones in the development of strong motion monitoring of earthquakes as judged by the author. Strong motion earthquake monitoring was motivated by the Great Tokyo earthquake of 1923 and was strongly influenced by Prof. Romeo Martel in the US and Prof. Kyoji Suyehiro in Japan. Also greatly influential in the development of a strong motion instrument was John R. Freeman who became interested in earthquakes at age 70. The first strong motion instrument was constructed by the US Coast and Geodetic Survey in 1932 and the first significant strong motion record was obtained during the Long Beach earthquake of 1933. This presentation traces the development of strong motion instruments and the analysis of strong motion data from the era of the Wood-Anderson Seismograph to more recent digital recorders.

Early strong motion instruments were analog and data was recorded on photographic film. There were many challenges in getting the recorded data into a form that was useful to engineers and others studying strong earthquake motions. Initially, photographic records were examined visually to determine notable features of the motion including peak acceleration, duration of shaking, and the nature of the envelope of the time history of motion. But in 1934 Prof. Hugo Benioff of Caltech introduced the Response Spectrum of an earthquake. This concept was later refined for engineering use by his colleague Prof. George Housner. The Response Spectrum provided earthquake engineers with an easily applied tool that could be used to estimate the response of a structure to earthquake excitation. Computation of Response Spectra from early film records was no easy task and relied heavily on the use of analog computers. However, in spite of these difficulties, sufficient data were analyzed so that the first “Design” Response Spectrum was published by Prof. Housner in 1959. Later, Prof. Newmark and Prof. Hall of the University of Illinois produced a further refined Design Response Spectrum that was widely distributed in a 1982 monograph by EERI.

Due to a landmark program instituted by the City of Los Angeles which mandated the installation of strong motion instruments, a treasure trove of approximately 400 strong motion records was obtained during the San Fernando earthquake of 1971. It was also significant that this earthquake occurred at the time when analog computation was giving way to digital computation in many fields of engineering. Capitalizing on the convergence of these two events, the NSF funded a project at Caltech to digitize and distribute the time history and Response Spectra data for all of the San Fernando records as well as other key historical records. The process of digitization revealed certain base-line problems with the data and band-pass filtering algorithms were developed to eliminate drift in the integrated acceleration data. New digital programs were also developed to compute Response Spectra.

In 1976, the Great Tangshan earthquake occurred in China killing hundreds of thousands of people. The following year, at the 6WCEE in New Delhi, India, a new international committee was formed on strong motion instrumentation. At that time, there were about 5,000 strong motion instruments deployed worldwide, 3,000 of which were in the US. In 1978 an International Workshop on Strong-Motion Instrument Arrays was held in Hawaii. The participants of that workshop concluded that understanding strong ground motion was critical to earthquake safety, that there was a scarcity of engineering data near the source of destructive earthquakes, and that countries needed to make a concerted effort to deploy instrument arrays capable of resolving the nature of the source mechanism, wave propagation, and local site effects associated with earthquakes. As a result of this workshop, a number of digital strong motion arrays were deployed worldwide including in Taiwan (SMART-1) and China.

The digital strong motion array deployed in China was in the aftershock region of the Great Tangshan earthquake. This array recorded more than 1050 near-field accelerograms from more than 400 events. On October 19, 1982, nine digital instruments recorded the M_L=5.7 Lulong event with the closest instrument being only 5 km from the epicenter. After overcoming some processing challenges, this record showed an interesting new type of “pulse-like” ground motion that had not been previously reported. After some initial dispute over the validity of this record, it was gradually accepted as indication a real phenomenon. This result was further validated by the 1992 M_L=7.5 Landers earthquake. An analog instrument installed by the Southern California Edison Company was located within 2 km of the fault trace of that event. The instrument was retrieved from the field and subjected to extensive testing at Caltech. The integration algorithms developed for the Lulong record were then applied to the Landers record. What was revealed was a clear indication of the pulse-like near-field ground motions. The same techniques were applied to recorded data from the 1992 M_L=6.7 Erzincan earthquake and the results were very similar. By this time, there was no disputing the existence of near-field pulse-like ground motions.

The 1995 Hyogoken-Nambu (Kobe) earthquake in Japan triggered a significant expansion of strong motion networks in Japan as well as in other Asian countries. The 1999 Chi-Chi earthquake in Taiwan yielded accelerograms from more than 600 instruments. The State of California presently has over 2,000 strong motion instruments deployed on the ground and in buildings.

As strong motion networks have gone from analog instruments to digital instruments, data retrieval and processing has also changed. It is now possible to retrieve and process data in near or true real-time. This opens up many exciting opportunities for enhanced decision making using string motion data. The presentation gives an example of a currently operating real-time monitoring system in the Millikan Library Building on the Caltech campus. This system is capable of providing real-time inter-story hysteresis diagrams to assist in damage assessment. Other possible applications of decision making based on real-time string motion monitoring are also given. These applications address the needs of a broad spectrum of stakeholders throughout society including public officials, building owners, building occupants, and individual citizens.

Strong motion monitoring has reached a level of maturity where we no longer celebrate the good fortune of obtaining one additional ground motion record from a distant earthquake. Therefore, it is the position of the author that our efforts need to be refocused from the capture of isolated records to obtaining integrated real-time information that can be used for rapid decision making.

The 2008 Joyner Lecture

TRANSPARENT SEISMIC MITIGATION FOR COMMUNITY RESILIENCE

Chris D. Poland, SE

Chairman and CEO, Degenkolb Engineers

Summary

Healthy communities continuously grow by leveraging their intellectual capital to drive economic development while protecting their cultural heritage. Success, in part, depends on the support of a healthy built environment that is rooted in contemporary urban planning, sustainability and disaster resilience. In many parts of the country, the ability to rebound from major earthquakes is an important facet of community health, one that depends on the expertise of the nation's earthquake professionals. We, as earthquake professionals, have the responsibility to deliver that expertise in an understandable fashion that can be interwoven into public policy while recognizing the community's natural ability to rebound. No one else has the technical knowledge to bring that perspective to the policy table.

Earthquake professionals -- Emergency Response Planners, Earth Scientists, and Earthquake Engineers -- have made great strides toward understanding how to record, characterize, build for, and recover from major earthquake events. Today's seismic hazard maps, performance based building codes, and integrated emergency response plans all demonstrate remarkable progress in just the past 30 years. Seismic hazards nationwide are understood and procedures are available to adequately predict performance. EERI's *Securing Society Against Catastrophic Earthquake Losses* defined a research and outreach plan in 2003 that would arrest the growth of seismic risk nationwide to acceptable levels. In 2006, EERI, SSA, and California OES co-convened a conference commemorating the 1906 San Francisco Earthquake and published *Managing Risk in Earthquake Country;* an action plan for reducing losses, to acceptable levels in future earthquakes. Unfortunately, progress on implementing these plans appears to be stalled due to a lack of funding and political will caused by complacency, misunderstanding, and an absence of persistent lobbying by the earthquake experts.

Planners and policy makers are deeply concerned with all aspects of their communities, including its seismic safety. Their reluctance to implement the latest plans for achieving seismic safety is rooted in a misunderstanding of the hazard they face and the risk it poses to their built environment. Probabilistic lingo and public debate about how big the "big one" drives them to resort to their own experience and intuition. "It's never happened here before" is a common justification for setting aside policy changes that will improve safety and resilience. The usual misconception of how much damage the built environment will experience is based on the belief that the building official and their latest building codes assure protection in damage proof buildings. There is a fundamental lack of transparency related to what is expected to happen and it is partially blocking the policy changes that are needed.

The solution: craft the message in broad based, usable terms that name the hazard, defines performance, and establishes a set of performance goals that represent the resiliency needed to drive a community's natural ability to rebound from a major seismic event.

With the assistance of the local earthquake professional community, urban planners, policy makers, and local City officials, the San Francisco Planning and Urban Research Association (SPUR) has established three study groups to sort out the issues. We are in the process of determining options and developing policy recommendations to assure that San Francisco and the Bay Area will not fall to the dilemmas that are preventing the restoration of much of the Gulf Coast after Hurricane Katrina. SPUR, in its usual role as an advocate for thoughtful Urban Planning, choose to take a different tack than has been used in the past. We are using transparent goals and measures with an intuitive vocabulary for both performance and hazard, and the recommendations describe a state of resiliency that is needed to support response and recovery.

SPUR is in the process of defining performance goals, for the built environment in terms of three time frames. The first relates to the initial response and lasts seven days. The second extends to 30 days and focuses the restoration of workforce housing and meeting ongoing social needs. The third is a three-year period of long-term reconstruction. During the initial period, essential facilities such as hospitals, police stations, and emergency response facilities are needed, along with housing that can support shelter-in-place, and the infrastructure systems needed to support reconstruction. The focus of the next period is on restoring the living environment for the workforce that will reconstruct the city, by reestablishing their utilities, schools, and neighborhood businesses. The third phase expedites the achievement of a "new normal".

SPUR is in the process of defining the hazard in terms that are consistent with current San Francisco programs and policies. Three earthquakes are named and defined for use in the recommendations. The "routine" earthquake is a 70% in 50-year event and used to define the service levels of tall buildings. The "expected" earthquake is a 10% in 50-year event and is used as the basis for the policies related to performance. The third is the "extreme" earthquake that is a 2% in 50-year event, the basis of the 2006 International Building Code.

SPUR is defining five performance measures for buildings and three for lifeline systems in an effort to establish an intuitive understanding of the expected post-event performance. Each declares whether people will be safe inside, whether the building will be able to be repaired and whether usable during repairs. Lifeline systems are further defined in terms of the time intervals to restore 90%, 95%, and full service. These transparent categories are used in conjunction with the expected earthquake level to describe the standards needed for new buildings and lifelines and the rehabilitation programs needed for existing buildings and lifelines so that the performance goals are achievable, the cultural assets protected, and the economy able to rebound. Because the definitions apply to individual types of uses of buildings and allow various time frames for restoration, the needed programs should prove to be achievable and cost effective.

Many of us strive to contribute to the greater good while doing our everyday jobs. It is a passion for me and has lead to my personal devotion to seismic risk reduction advocacy nationwide. As earthquake professionals, we are very lucky to be able to contribute an expertise that can save lives as well as communities. In 30 plus years, I've learned that I can be effective when working with other structural engineers on buildings codes, pace setting when working with the larger family of earthquake professionals, and actually able to change public policy when providing my technical expertise to the broader community of policy makers while helping them craft the policies needed to instill change. It takes patience and a broad understanding of all the issues being faced. It's not unlike my trade, fitting a structure into a building. Here it is fitting seismic into my community and the results are worth the effort and frustration. I challenge each of you to do the same. Volunteer and work toward making your community healthier.

IDENTIFICATION OF THE BASELINE MODAL PARAMETERS OF THE CARQUINEZ SUSPENSION BRIDGE USING AMBIENT VIBRATION DATA

Raimondo Betti and Ah Lum Hong

Department of Civil Engineering and Engineering Mechanics
Columbia University, New York

Abstract

The identification of modal parameters has been performed for the New Carquinez suspension bridge in California. By using multiple ambient vibration data sets recorded through a wind-motion monitoring system in the bridge, the baseline modal parameters were obtained in order to investigate dynamic behavior of the bridge in operating conditions. For the modal parameters identification, the data-driven stochastic subspace identification technique was implemented. For each data set, the modal parameters for structural modes were estimated by examining the estimation error between measured data and reconstructed one from the identified modes. Based on the results, variability of the identified modal parameters was also investigated.

Introduction

The Newly built Carquinez suspension bridge (NCB) linking Vallejo with Crockett in California is located in a windy area and near three active earthquake faults (the San Andreas Fault, the Hayward Fault, and the Franklin Fault). For structural health monitoring of this bridge in operational condition, the Strong Motion Instrumentation Program (SMIP) has devised a wind-motion monitoring system as well as an earthquake monitoring system by installing accelerometers over the bridge. Since, in vibration based structural health monitoring, the evaluation of a structure's global dynamical behavior requires past or undamaged state information of the structure as a baseline, having precise baseline dynamic properties of the structure is important in order to assess such a structure's condition in the future.

When only structural responses are available for the characterization of a structure's dynamic properties, as it is in ambient vibration cases, stochastic system identification techniques are usually implemented to identify its modal parameters (natural frequencies, damping ratios, and mode shapes). Peeters and De Roeck [1] reviewed currently used stochastic system identification techniques in both frequency and time domains. Among such techniques, Frequency Domain Decomposition (FDD) technique in frequency domain and Stochastic Subspace Identification (SSI) technique in time domain are showing great promise, especially in detecting closely spaced modes [2]. However, despite of attempts to further improve efficiency of such techniques [3][4], they are still in need of improvement since results from both the techniques are quite sensitive to choices of certain parameters in their implementations. In comparing the FDD and SSI techniques, Brincker *et al*. [5] showed that the FDD technique has less uncertainty on damping estimates than the data driven SSI technique; however, the results from the FDD were significantly affected by the frequency resolution and so, consequently, by

the length of time histories. In fact, the authors concluded that at least 1 hour long time histories were required for a proper estimation of damping ratios.

In this study, the data driven SSI technique was implemented for modal parameters identification in order to build baseline modal parameters of the NCB using 17 ambient vibration data sets recorded from the bridge in operating condition. To this end, practical issues in the implementation of data-driven SSI technique were first investigated and an efficient way of identifying modal parameters from this technique was proposed. After that, certain bounds of modal parameter estimates for each identified mode were provided.

Ambient Vibration Data

Sensor Configuration

As a part of the SMIP monitoring of the NCB, 76 accelerometers were placed on towers, piers, abutments, anchorages, piles of the towers as well as on the bridge deck for monitoring earthquake induced motions of this bridge. Among such 76 accelerometers, a set of ten accelerometers on the northern half of the deck also belongs to the wind-motion monitoring system, with a supplement of an anemometer placed at the mid-span. Figure 1 displays the locations of such ten accelerometers (six in vertical, three in transverse, and one in longitudinal directions) in the wind-motion monitoring system. The purpose of this wind-motion monitoring system is to record the dynamic behavior of this bridge under ambient excitations (i.e. wind and traffic loadings).

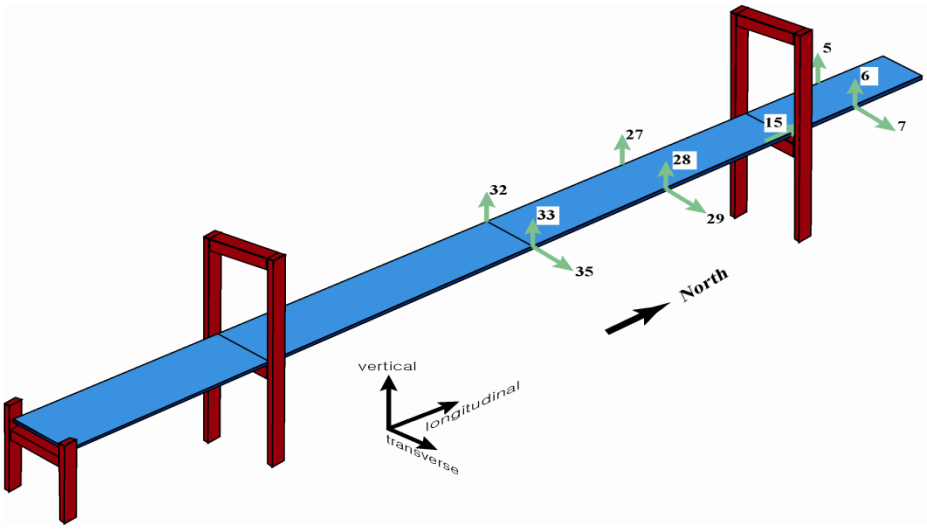

Figure 1. Locations of the sensors belonging to the wind-motion monitoring system

Measurement Properties

A total of 21 data sets of ambient vibration responses were recorded through either the wind-motion or earthquake monitoring systems. Table 1 indicates the recording date, start time,

and duration of each data set as well as wind information in terms of the mean wind direction (D_v) and the mean of wind speed (V_v) along the mean wind direction. Data sets #1 to 4 were measured on windy days and data sets #5 to 8 at the same time (10:00pm) for four days in February. Furthermore, in order to examine a change in modal parameters during the day and night time, data sets #9 to 21 were recorded at different times from afternoon to midnight for three days in May. The data sets also have various record lengths from 54 sec (data set #3) to 1068 sec (data set #10).

Among the 21 data sets, structural responses of data sets #3 and 8 were measured through the earthquake monitoring system with the sampling frequency of 200 Hz while the other sets through the wind-motion monitoring system with 20 Hz of the sampling frequency. Since the anemometer does not belong to the earthquake monitoring system, wind information was not provided for data sets #3 and 8.

In this study, only 17 data sets that have the record lengths of at least 10 minutes were considered for the identification of the NCB's modal parameters.

Table 1. Ambient vibration data information

Data Set #	Date	Time	Length	Wind	
				V_v [m/s]	D_v[^{o}]
1	27-Feb-06	19:18:55	350 sec	11.11	209.9
2	25-Mar-06	12:34:44	99 sec	11.58	244.3
3	20-Jun-06	18:31:16	54 sec	-	-
4	04-Jan-08	10:53:35	641 sec	13.81	196.0
5	22-Feb-08	21:59:38	797 sec	3.44	282.8
6	23-Feb-08	21:59:37	804 sec	3.63	180.2
7	24-Feb-08	21:59:42	776 sec	3.63	230.5
8	27-Feb-08	21:59:38	300 sec	-	-
9	14-May-08	13:11:03	607 sec	1.86	312.3
10		13:59:41	1068 sec	1.40	289.1
11		14:59:38	794 sec	1.46	339.6
12		15:59:38	789 sec	1.23	291.8
13		23:59:38	790 sec	1.29	258.8
14	21-May-08	13:59:38	779 sec	7.46	248.7
15		14:59:37	793 sec	9.18	267.9
16		15:59:37	793 sec	9.30	262.2
17		23:59:38	800 sec	6.43	297.5
18	22-May-08	13:59:37	799 sec	5.90	182.8
19		14:59:40	779 sec	6.46	170.2
20		15:59:38	782 sec	6.09	170.7
21		23:59:37	805 sec	7.25	261.3

Response Measurements

The 17 data sets analyzed in this study to build baseline modal properties of the NCB cover various characteristics of structural responses in time and frequency domains. For instance,

the peak accelerations of the data sets vary from 3.08 to 26.56 cm/sec^2 in vertical direction (at Ch 32 and Ch33) and from 0.41 to 4.16 cm/sec^2 in transverse direction (at Ch 35) at mid-span, and from 0.39 to 2.99 cm/sec^2 (at Ch15) in longitudinal direction.

Figures 2 and 3 present typical time histories of accelerations having different features. In comparison with the time histories from data set #4 in Figure 2, those from data set #21 in Figure 3 exhibit a nonstationary property of having time-varying mean square values. The appearance of such large peaks in a predominantly small amplitude signal is responsible for the nonstationarity of the signal and is linked to the high frequency contents in the signals. Figures 4(a) and (b), which displays normalized power spectral density estimates of the time histories in Figures 2 and 3, respectively, indicate that structural responses of data set #4 are characterized mostly by low frequencies of less than 1 Hz while those of data set #21 are under significant influence of the frequencies between 0 and 1Hz as well as between 3 and 5Hz.

In this study, since the analysis is focused on the identification of primary structural modes, usually in the frequency range of less than 1Hz, the measurements were filtered by using a Butterworth low-pass filter of the ninth order with a cutoff frequency of 1.1Hz.

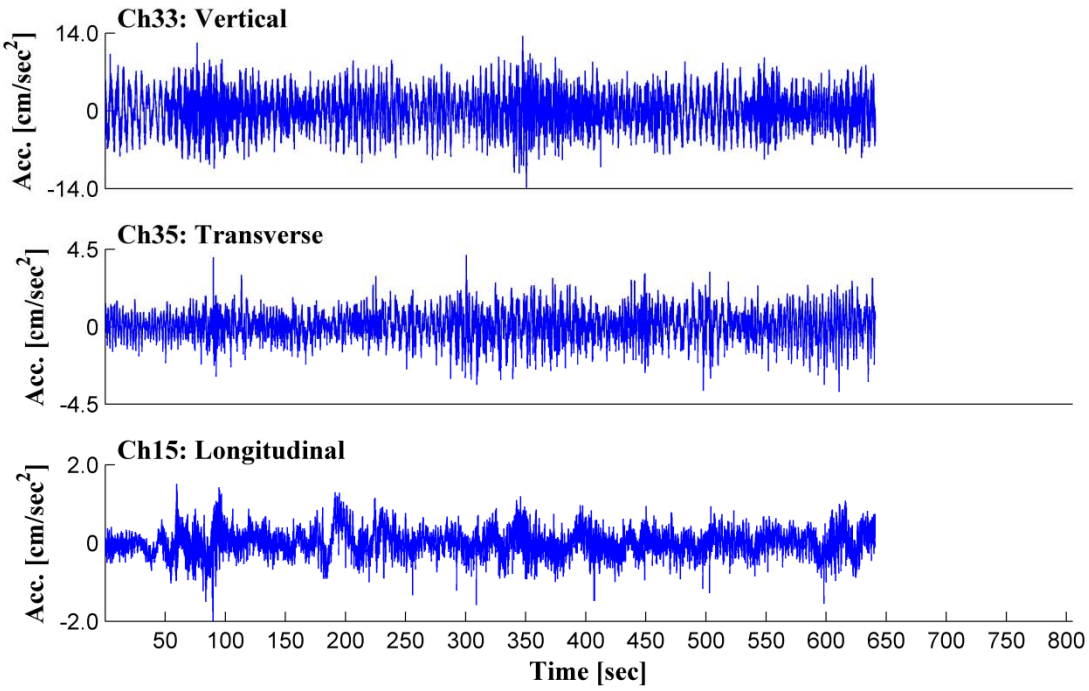

Figure 2. The time histories of acclerations in data set #4

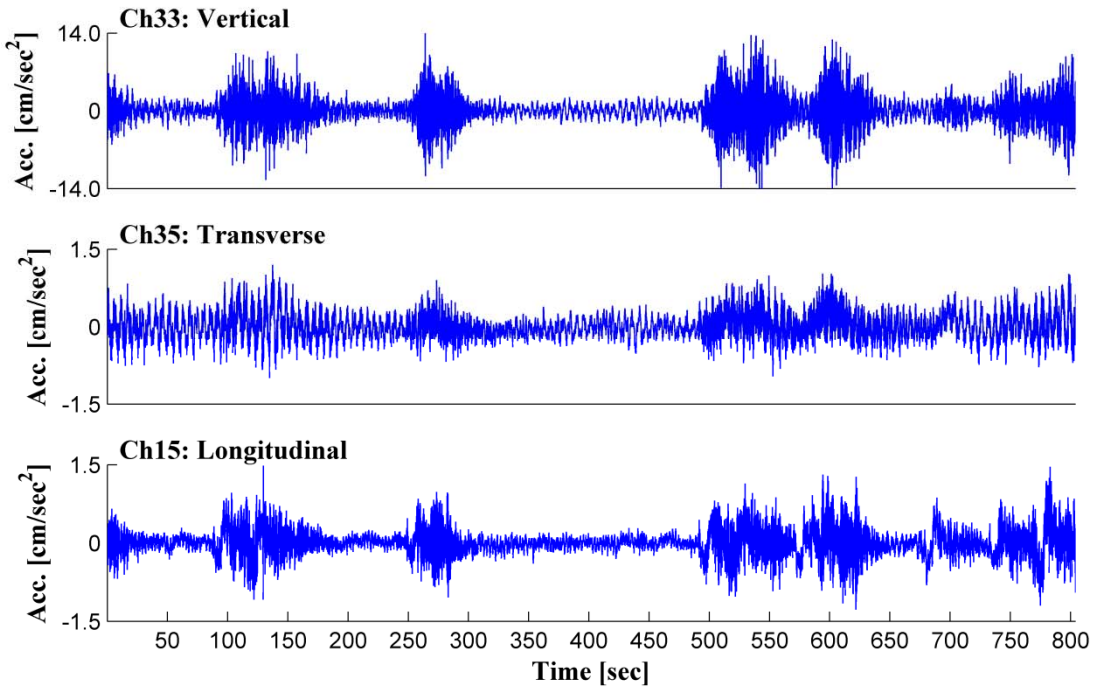

Figure 3. The time histories of acclerations in data set #21

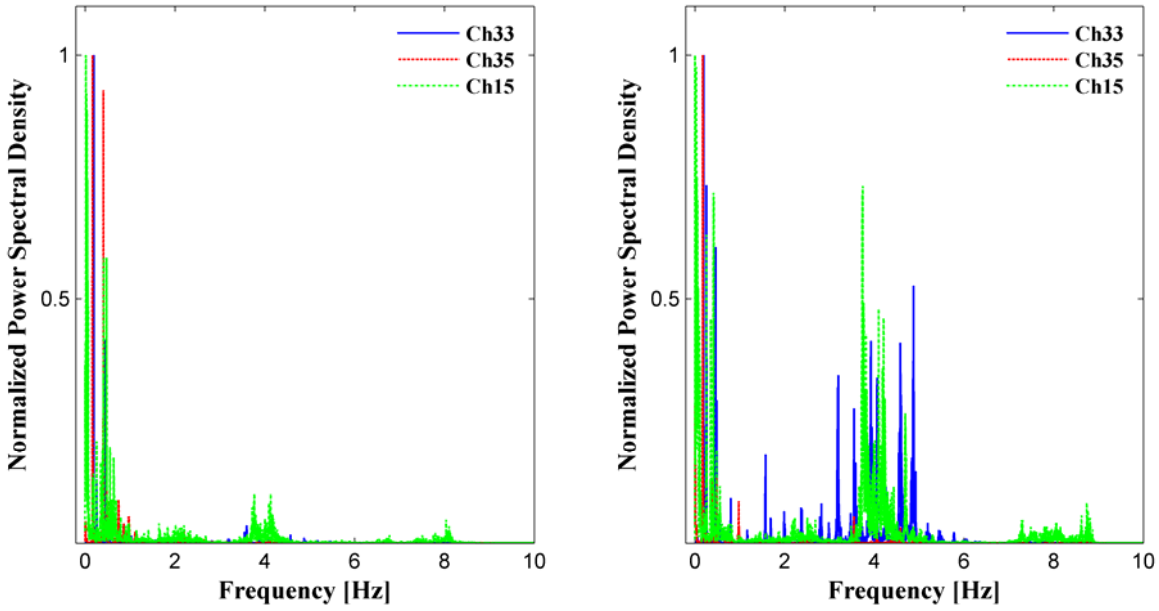

(a) data set #4 **(b)** data set #21

Figure 4. Normalized power spectral density

In addition, the statistical properties of the filtered output observations were examined since the SSI technique presumes that a structural process be Gaussian process. Figure 5 presents the peak acceleration, kurtosis, and skewness of Chs 33 (vertical), 35(transverse), and 15 (longitudinal). Based on the fact that for the Gaussian distribution, the kurtosis and skewness are supposed to be 3 and 0, respectively, vertical and transverse measurements generally show characteristics similar to those of a Gaussian distribution while longitudinal measurements appear to have large values of kurtosis. Since Ch 15 is placed on the deck, at a location where the deck is connected to the tower with the rocker links, it might induce noticeable outliers so to result in a large measure of kurtosis.

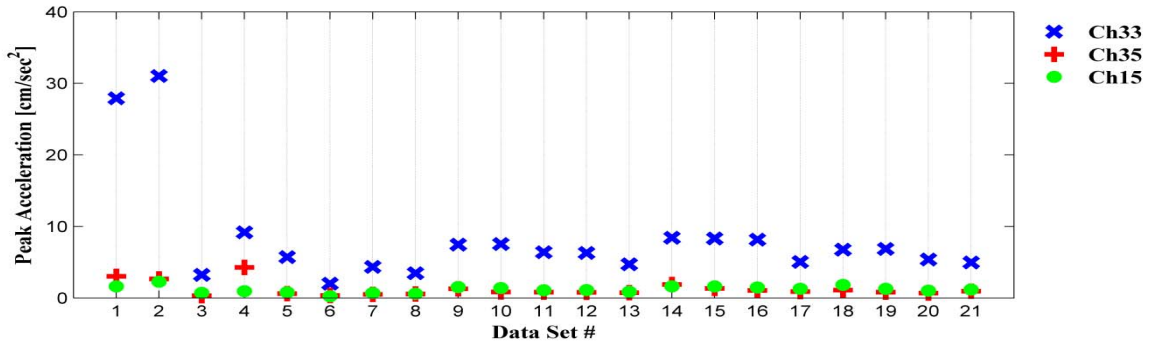

(a) Peak Acceleration

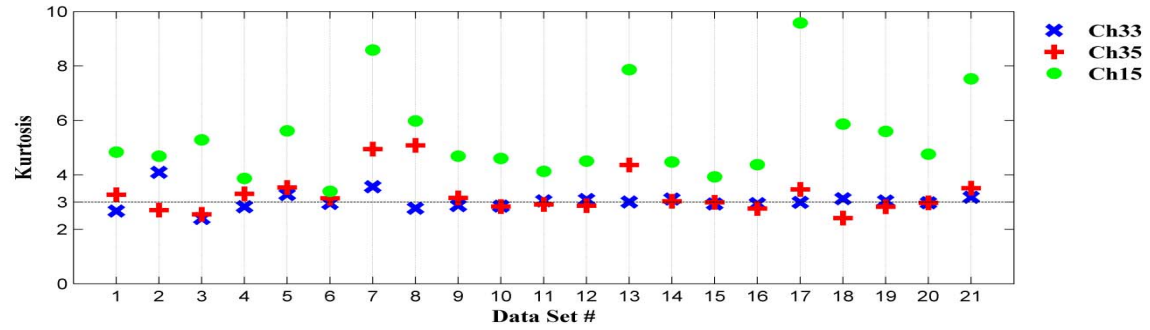

(b) Kurtosis

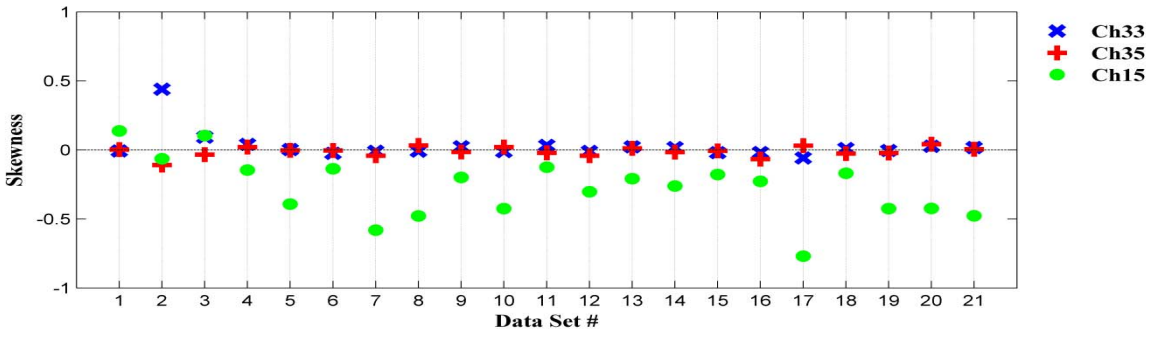

(c) Skewness

Figure5. Statistical properties of response measurements

Data-Driven Stochastic Subspace Identification

Mathematical Models

Stochastic subspace identification technique was established based on stochastic state-space and its innovation (Kalman filter) models. An n^{th}-order linear time-invariant stochastic system with m output observations can be represented in the form of a stochastic discrete-time state-space model such as

$$\begin{aligned} x(k+1) &= A\,x(k) + w(k) \\ y(k) &= C\,x(k) + v(k) \end{aligned} \tag{1}$$

where $x(k) \in \Re^{n\times 1}$ and $y(k) \in \Re^{m\times 1}$ are state and output vectors at time k, respectively, and $A \in \Re^{n\times n}$ and $C \in \Re^{m\times n}$ are, respectively, system and observation matrices. The vectors $w(k) \in \Re^{n\times 1}$ and $v(k) \in \Re^{m\times 1}$ represent process and measurement noises, respectively, and are assumed to be zero-mean white Gaussian processes with covariance matrices: $\mathbf{E}[w(k)w^T(j)]=Q\delta(k-j)$, $\mathbf{E}[v(k)v^T(j)]=R\delta(k-j)$, and $\mathbf{E}[w(k)v^T(j)]=S\delta(k-j)$, where $\delta(k-j)$ is an identity matrix when $k=j$ and zero when $k\neq j$.

When the state vector needs to be estimated with only output observations in the absence of input information, an optimal estimate of $x(k)$, denoted by $\hat{x}(k)$, might be the one that has the minimum variance with respect to $x(k)$. Such an optimal state estimate, can be derived by applying a Kalman filter to Eq. (1) in the following forms [6]

$$\begin{aligned} \hat{x}(k+1) &= A\hat{x}(k) + K\,e(k) \\ e(k) &= y(k) - C\,\hat{x}(k) \end{aligned} \tag{2}$$

where $K \in \Re^{n\times m}$ indicates a Kalman filter gain matrix and $e(k) \in \Re^{m\times 1}$ is the output residual vector having a property of being a zero-mean, white noise process. From Eq. (2), it can be readily observed that the Kalman state vector at the current time k is expressed by a linear combination of the past output vector sequence so to be defined on the past output space.

Data-driven Stochastic Subspace Identification

Considering that the Kalman state vector $\hat{x}(k)$ demands past i output observations (i.e. $y(j), j=k-1, k-2, \ldots, k-i$) for its estimation, past and future output block matrices can be formed [7], respectively, as

$$Y_p = \begin{bmatrix} y(0) & y(1) & \cdots & y(j-1) \\ y(1) & y(2) & \cdots & y(j) \\ \vdots & \vdots & \cdots & \vdots \\ y(i-1) & y(i) & \cdots & y(i+j-2) \end{bmatrix} \text{ and } Y_f = \begin{bmatrix} y(i) & y(i+1) & \cdots & y(i+j-1) \\ y(i+1) & y(i+2) & \cdots & y(i+j) \\ \vdots & \vdots & \cdots & \vdots \\ y(2i-1) & y(2i) & \cdots & y(2i+j-2) \end{bmatrix} \tag{3}$$

where the index j is assumed to be infinite because, in the derivation of the SSI method, certain statistical properties (e.g. output covariance) need to be computed directly from Y_p and Y_f under the assumption that the sequence of output observations in each row of both Y_p and Y_f be an ergodic process. Then, the orthogonal projection of the row space of Y_f onto the row space of Y_p can be formulated in terms of the so-called observability matrix (Γ_i) and the Kalman state vector sequence ($\hat{X}_i$) such as

$$O_i = Y_f / Y_p = \begin{bmatrix} C \\ CA \\ CA^2 \\ \vdots \\ CA^{i-1} \end{bmatrix} \begin{bmatrix} \hat{x}(i) & \hat{x}(i+1) & \cdots & \hat{x}(i+j-1) \end{bmatrix} = \Gamma_i \hat{X}_i \tag{4}$$

Eq. (4) implies that the rank of O_i is equal to the dimension of the state vector, the column space of O_i equal to the column space of Γ_i, and the row space of O_i equal to the row space of $\hat{X}_i$. Hence, the observability matrix and the Kalman state vector sequence can be identified by properly decomposing the projection matrix O_i.

Once the observability matrix Γ_i is obtained through the decomposition process of O_i, the system matrix A and the observation matrix C can be easily extracted from Γ_i for the modal parameter identification. In addition, when the Kalman filter gain matrix K needs to be identified in order to have an innovation model of Eq.(2) completed, the matrices A and C can be obtained in a least-square sense from the following

$$\begin{bmatrix} \hat{x}(i+1) & \hat{x}(i+2) & \hat{x}(i+3) & \cdots \\ y(i) & y(i+1) & y(i+3) & \cdots \end{bmatrix} = \begin{bmatrix} A \\ C \end{bmatrix} \begin{bmatrix} \hat{x}(i) & \hat{x}(i+1) & \hat{x}(i+3) & \cdots \end{bmatrix} + \begin{bmatrix} w' \\ v' \end{bmatrix} \tag{5}$$

where w' and v' are the Kalman filter residuals so to be able to estimate the Kalman filter gain from the covariances of w' and v'. By using the identified matrices A, C, and K, output observations can be reconstructed from the reformulated equation of Eq.(2) as

$$\begin{aligned} \hat{x}(k+1) &= (A - KC)\hat{x}(k) + K\, y(k) \\ \hat{y}(k) &= C\, \hat{x}(k) \end{aligned} \tag{6}$$

where $\hat{y}(k)$ represents reconstructed output sequence from the identified model.

Subsequently, from the state and observation matrices, modal parameters can be obtained by considering the continuous time equivalent state matrix. When output observations are not contaminated by noise, the dimension of the state matrix can be clearly indicated by singular values of O_i in Eq. (4) and so the modal parameters for the system's modes can be estimated just from a realized model. However, when output measurements are disturbed by noise, the projection matrix O_i has full rank and this makes it difficult to assign a certain order to an identified system model only based on the singular values distribution. Even though it is true

that having a higher order identified model helps in minimizing the error between the measured data and the reconstructed responses from the identified model, this error reduction could be due to noise modes that are now included to improve the fitting between the data sets. For this reason, in the application of the SSI technique using real measurements with noise, the extraction of modal parameters corresponding to structural modes is generally complemented by a Stabilization Diagram (SD). Such a diagram, which represents the identified frequencies as a function of the model's order, highlights modes whose properties do not change significantly when varying the dimension of the state vector; such modes are considered as structural modes. In order to form the SD, an observability matrix is repeatedly formulated from Eq. (4) varying the dimension of the state, which provides different pairs of state and output matrices of corresponding orders. The properties of poles in a model of a certain order are compared with those of a two order larger model and stable and unstable modes are determined on the basis of the identified frequencies, damping ratios and mode shapes.

Implementation of the SSI Technique

The SSI technique complemented by the SD, for modal parameter estimation, involves three practical issues that need to be addresses in its implementation: 1) the order of realized state-space models necessary for a certain number of stable modes to appear in the SD could be extremely high; 2) even when a mode is considered stable between certain orders of realized models, estimates of the mode's properties could vary depending on a selection of the model from which those are extracted; and 3) modal parameter estimates, especially damping ratios, are very sensitive to a choice of the number of block rows i in Eq. (3). In this section, we will discuss these issues and then propose an efficient way of implementing the SSI technique to accurately identify modal parameters from ambient vibration measurements.

The problem related to the dimension of the state required to detect stable modes, can be easily controlled, to some extent, if preliminary information about the range of interest for natural frequencies of the structure under consideration is given. In the case of suspension bridges, it is known that vibrational modes contributing to their global response to ambient excitation are mainly confined in the frequency range from about 0 to 1 Hz and so higher frequency contents in measured signals can be considered as trivial information for the characterization of such bridges' fundamental dynamical properties. Therefore, filtering out higher frequency contents and downsampling time histories (to reduce the Nyquist frequency) lead to a reduction of the order of a realized model to represent signal properties. In addition, applying a proper weighting matrix to the projection matrix in Eq. (3) also can help lowering the necessary dimension of the state vector. In fact, the SSI technique considers three different algorithms (the principal component, canonical variate, and unweighted principal component algorithms) which differ from the set of weighting matrices multiplied by the projection matrix. From a comparative study of the three algorithms in the analysis of two suspension bridges (Vincent Thomas Bridge and the New Carquinez Bridge), it was revealed that the principal component algorithm showed the best performance determining the smallest dimension model capable of properly representing the structure's properties [8].

After distinguishing structural modes from noise modes using the SD, one needs to extract modal parameters of structural modes (i.e. stable modes) from realized models: such

parameters can be computed either at once from one specific model which includes all the stable modes, or from different models for each individual mode. However, it is not always easy to find one specific model with all the stable modes. Indeed, modal parameter estimates, especially damping ratios, are significantly affected by the selection of a model's order.

Figure 6(a) presents a stabilization diagram (with i=100 in Eq. (3)) using the six time histories of vertical accelerations from data set #4 as well as the Power Spectral Density (PSD) plots of the measurements. Such a diagram was built by comparing frequencies, damping ratios,

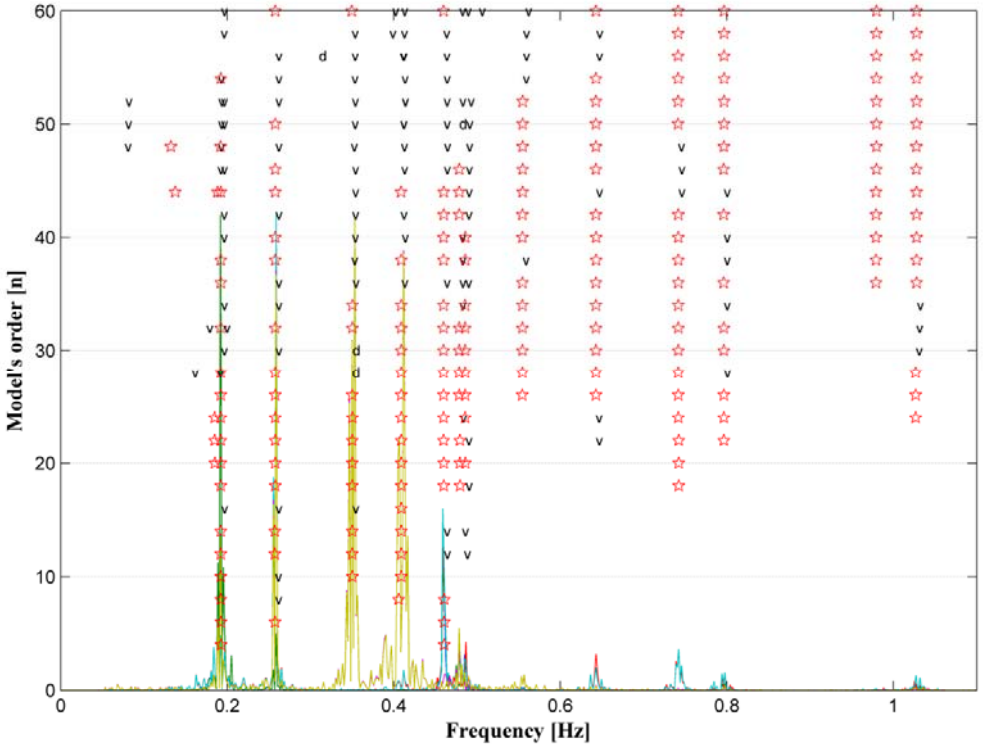

(a) Stabilization diagram

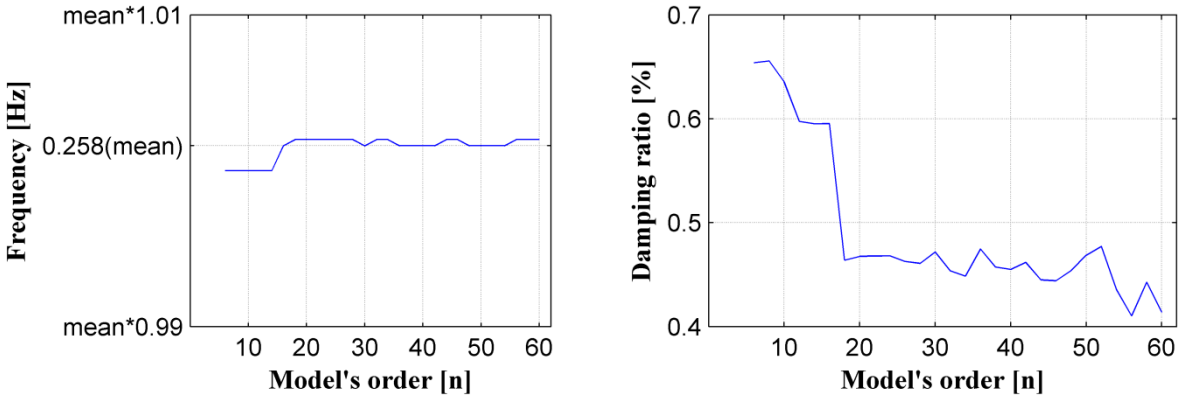

(b) Variations in frequency and damping ratio estimates along model's order

Figure 6. Stabilization diagram and variation in modal parameter estimates

and modes shapes, for each model order, with the corresponding values of a two-order higher model: the frequencies are first compared and modes that have differences of 1% or less in the identified frequencies are retained. Then, the corresponding damping factors and mode shape vectors are compared with stability criteria of 3% difference for the damping and 1% for the mode shape (i.e. MAC>0.99), respectively. In Figure 6(a), a mode that satisfies all the criteria is represented with a 'star', a mode that only satisfies the frequency and mode shape criteria with a 'v', and a mode that only satisfies the frequency and damping ratio criteria with a 'd'. Even though the SD in Figure 6(a) clearly displays modes that are consistent with the frequency peaks of the PSD plots, there is no specific model that includes all the stable modes appearing in Figure 6(a). Moreover, even when modal parameters of stable modes are estimated from different models, a proper selection of a specific model should be made for each mode since the selected model's order can results in large variations of the identified parameters, especially the damping. To explain this, let's consider Figure 6(a) that shows that the mode with the corresponding frequency of about 0.258 Hz is a structural mode. When modal parameters are calculated for such a mode, any model of order ranging between 6 and 56 will provide consistent values of frequency as well as mode shape vector, but not of the damping ratio. Figure 6(b) shows a significant variation in the identified damping ratios ranging from 0.41% to 0.66% as the order of the model decreases. Because damping ratio estimates are more affected by the model's order than the frequency and mode shape, a less restrictive stability criterion is generally assigned to the damping ratio. In this way, the SD is capable of detecting stable modes that satisfy all the criteria; however, because of the loose criterion on the damping, there is an increased possibility of identifying less accurate damping ratios.

For the selection of the order of a realized model for the estimation of the modal parameters, realized system models of different orders were divided into groups, for each mode, in each of which all the modal parameters, including the damping ratio, were consistently stabilized. Among the group covering the largest range of models' orders, the model with the largest dimension of the state vector was selected for the parameter estimation.

With regard to the selection of the number of block rows i, Pridham and Wilson [9] showed that significant variations occurred in the damping ratio estimates for different pairs of i and j in Eq. (3) in the ambient vibration analysis of the Vincent Thomas suspension bridge and also remarked that no definite rule to find an optimal pair of them could be derived from the analysis. For the optimal estimation of damping ratios, the same authors [10] proposed a method that consists in optimizing realized state-space models from the SSI technique through the expectation maximization algorithm. In order to select the best initial models, they found ten models that contain the maximum number of stable modes by taking into account possible combinations of i, j, and n (the system's order).

In this study, rather than obtaining clearly stable modes on the SD by changing the value of i, a relatively simple way of selecting i is proposed based on the error between measured data and reconstructed one from the identified structural modes. Note that, in the theoretical implementation of the SSI technique, the number of block columns j is assumed to be infinite. However, data sets analyzed in this study have record lengths of about 10 min., which cannot be considered long in the ambient vibration analysis, and, consequently, j is automatically determined by the value of i ($j=nd-2\times i+1$ where nd is the number of data points); hence, only an

effect of change in *i* was examined in this study.

The error between measured data and reconstructed one from the identified structural modes can be calculated in the following way. Eq. (6) can be restated in modal coordinates such as

$$\hat{y}(k) = C(\Psi\ \Psi^{-1})\hat{x}(k) = C_m\hat{x}_m(k) \tag{7}$$

where Ψ is the eigenvector matrix of the state matrix A (A= $\Psi\ \Lambda\Psi^{-1}$) and C_m and $\hat{x}_m(k)$ denote $C\Psi$ and $\Psi^{-1}\hat{x}(k)$, respectively. This equation allows us to decompose the reconstructed signal from an identified triple of A, C, and K into each mode's contribution: a contribution of the q^{th} mode to the output observations can be computed as

$$\hat{y}(k)_q = C_m(:,q)\hat{x}_m(k)_q \tag{8}$$

where $\hat{x}_m(k)_q$ represents the q^{th} element of the transformed state vector $\hat{x}_m(k)$ while $C_m(:,q)$ indicates the q^{th} column of the matrix C_m. $\hat{y}(k)_q$ represents the contribution to the total response by the q^{th} mode. From this formulation, the contribution from each specific mode to the overall response can be obtained from the model selected among the models in which this mode is stable. The contributions from different modes can be easily obtained from models of different order, depending on the stability of each mode. Then, the sum of the contribution signals extracted from different models yields the reconstruction of the measurements which is attributed to only structural modes and so the measurement error $\boldsymbol{\varepsilon}(k)$ can be calculated as

$$\boldsymbol{\varepsilon}(k) = y(k) - 2\times\sum_{q=1}^{ns}\hat{y}(k)_q \tag{9}$$

where *ns* denotes the number of stable modes and the number 2 is associated to the fact that modes come in complex conjugate pairs. Based on this error estimate, the optimal value of *i* and, consequently, modal parameter estimates that produce the smallest error can be obtained. Furthermore, a relatively large amount of error could also indicate that some of structural modes that are contained in the measurements fail to be identified in the analysis.

To show this process, consider the analysis which used the same measurements (six vertical accelerations) from data set #4 as those for the SD in Figure 6. In order to examine the effect of a change in *i* on the estimated errors, the value of *i* varied from 20 to 200. The errors obtained at Channels 33, 28, and 6 are presented in Figure 7 in terms of the relative Root Mean Square (RMS) values as a function of *i*. Such a figure implies that values of *i* smaller than 50 cannot be used for a successful implementation of the SSI technique. It also points out that having a larger value of *i* does not guarantee a better result. In fact, the errors between 140 and 200 of *i* are shown to be larger than those between 70 and 130 in Figure 7. In the case of this analysis for data set #4, the optimal value of *i* was selected to be 80 which produced the smallest error on the average of the relative RMS errors at the six channels. Figure 8 exhibits one of the

reconstructed signals with i=80.The reconstructed signal shows a good match with the measured one with the error of 11.97% (0.29 cm/sec^2). It might be worth noting that the optimal is for the analyses of the other data sets also turned out to be between 70 and 130.

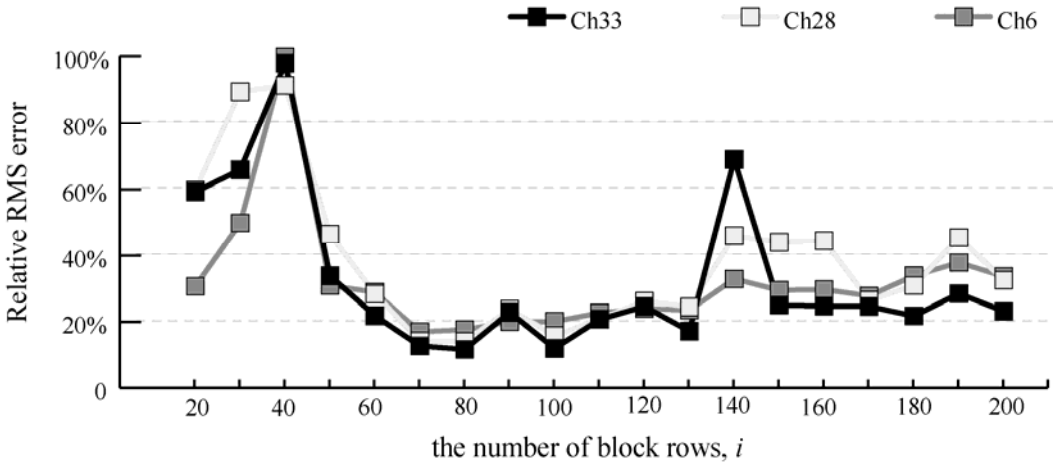

Figure 7. The effect of a change in the number of block rows, i, on relative RMS errors

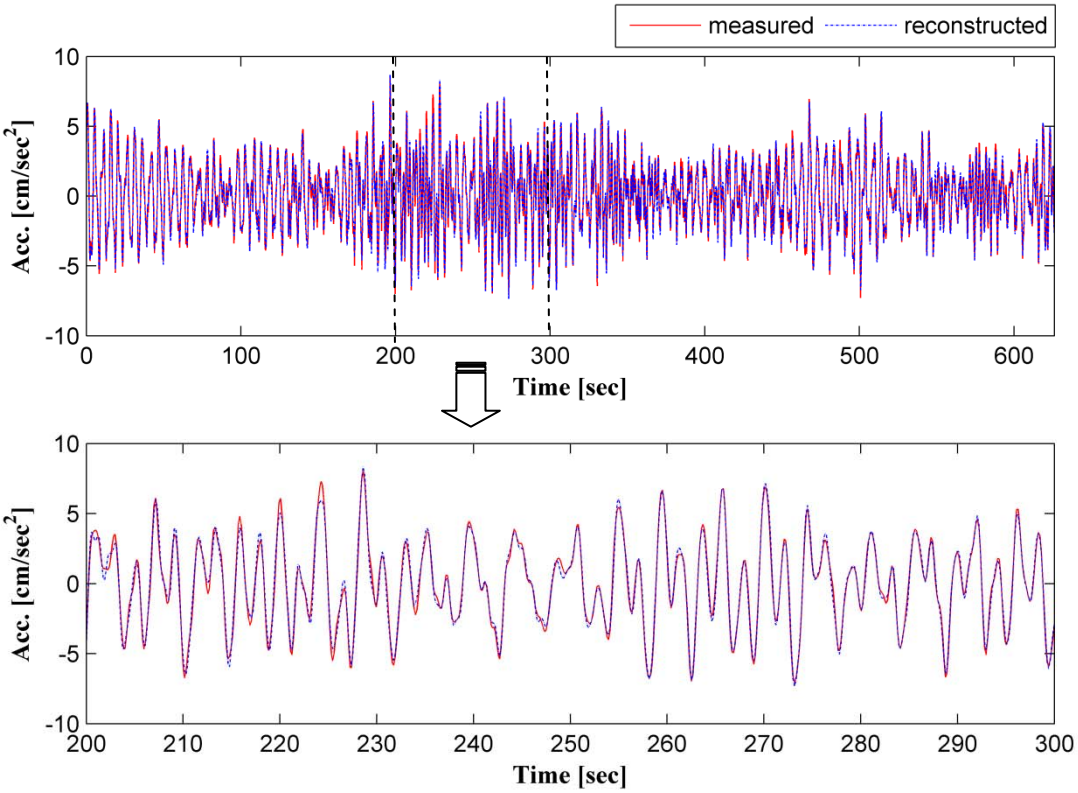

Figure 8. Measured and reconstructed accelerations (at Ch 33) with i=80

Identified Modal Parameters

In this study, structural modes of the Carquinez suspension bridge were classified into four groups: vertical, torsional , transverse, and torsion/transverse (hybrid) modes. Modal properties for vertical and torsional modes were estimated from the analysis using the six time histories of vertical accelerations while those for transverse modes were computed from the analysis using the three time histories of transverse accelerations. For modal parameter estimates of torsion/transverse modes, on the other hand, the six vertical and three transverse acceleration measurements were considered together. Although vertical, torsional, and transverse modes could also be identified when all the measurements in different directions were considered at the same time, it was difficult to obtain, from all the data sets, results as accurate as those obtained when measurements in each direction were separately analyzed. Hence, vertical, torsional, and transverse modes were analyzed using acceleration time histories in the corresponding directions while hybrid modes were identified using all the measurement together making allowances for uncertainty.

In order to classify the identified modes into such groups, it is a priority to characterize such modes' shapes. The identified mode shape vectors are complex and so, at each sensor location, they are characterized by an amplitude and by a phase, which is different from location to location. Hence, because of the phase variation, it is very difficult to plot schematic representation of each mode shape. In addition, since the mode shape vectors are extended to the entire structure by connecting the identified value at the sensors locations by straight lines, the use of the small number of sensors located only on half of the deck made it hard to visualize whether a particular mode is symmetric or anti-symmetric; hence, previous experimental [11] as well as numerical [12] studies on the NCB were cited to help with such a distinction.

With regard to the characterization of hybrid modes, data set #4 was first analyzed, as a representative data set using all the ten measurements in the three directions (vertical, transverse, and longitudinal). Since, among those available, data set #4 was recorded when the NCB experienced the strongest wind, a relatively large number of structural modes including hybrid modes was well excited to be clearly identified. Based on these mode shapes identified from data set #4, it was possible to distinguish torsional and transverse modes from hybrid torsional/transverse modes when measurements in the vertical and transverse directions were separately used in the analysis. Furthermore, considering the measurement in the longitudinal direction also allowed us to represent a hybrid longitudinal/vertical mode. In fact, there was a specific mode which displayed a longitudinal displacement while exhibiting a symmetric shape in the vertical direction. Such a mode was classified neither symmetric nor anti-symmetric in the study by Conte *et al*. [11] since, in the identification, the authors utilized only the time histories of the vertical response on the main deck.

Tables 2 and 3 present the natural frequencies and damping ratios, identified from the 17 data sets, for vertical modes and for torsional, transverse, and torsion/transverse modes, respectively, with those presented in the studies by Conte *et al*. [11] and Scanlan and Jones [12]. The identified mode shapes that correspond to those in Tables 2 and 3 are displayed Figures 9 and 10, respectively. Note that not all the modes were consistently identified from all the data sets because the only modes that could be identified were those that were contained in the

measurements and not all of them were equally excited. The identified frequencies in this study show a good agreement with those from the other studies, except one corresponding to the first anti-symmetric mode (V1 in Table 2). While the mode occurred with the frequency of 0.15 Hz in the numerical study [12], higher frequencies were identified for such mode in the experimental studies including the current study: 0.201Hz in the study by Conte *et al*. [11] and between 0.179 and 0.197 Hz in this study. With regard to damping ratios, the damping ratios identified in this study appear to be, in general, larger than those in the study by Conte *et al*. [11]. One of the reasons for such a discrepancy might be in the difference in the analyzed data: 20 min long ambient vibration data was used in Conte *et al*. [11], which is almost twice as long as the ones used in this study.

Variability of Modal Parameters

Modal parameters represent a structure's dynamic properties and could be used to detect structural damage. In fact, the appearance of damage could be reflected by a change in such parameters. However, since the estimates of modal parameters can also vary because of different environmental and operational conditions (such as temperature, wind, humidity, and traffic flow), it is important, for a given structure, to understand the variability of such parameters with the environmental factors so to distinguish their effects from those induced by structural damage.

Recently, various studies have been performed about effects of different environmental and operational conditions on the variability of modal parameters, especially fundamental natural frequencies of long-span bridges such as suspension and cable stayed bridges. With regard to temperature effect, Sun *et al.* [13],with continuously monitored data for 8 months from Donghai cable-stayed bridge in China, and Kang *et al.* [14], with continuously monitored data for 5 years from Seohae cable-stayed bridge in Korea, showed that fundamental frequencies of such long span bridges decreased when the temperature increased. Using 288 data sets for weekdays and 123 for weekends recorded from Vincent Thomas suspension bridge in the United States, Yun *et al*. [15] presented differences in the identified frequencies and damping ratios between weekdays and weekends. Also, Abe *et al*. [16] pointed out, from the analysis using continuously measured data over 100 hours from Hakucho suspension bridge in Japan, that the identified natural frequencies were reduced as wind velocity became higher while the identified damping ratios started to increase when wind velocity reached at a certain level.

In this study, from the investigation of effects of wind speed on the identified frequencies and damping ratios, it was observed that when wind speed increased, the identified natural frequencies for certain modes decreased while the identified damping ratios increased, as presented in Abe *et al*. [16]. Also, in comparing the results from the data sets recorded at different times on the same days (data sets #9 to 13, data sets #14 to 17, and data sets #18 to 21), variations in the identified frequencies and damping ratios during a day were found. Nevertheless, because of the limited number of the data sets used in this study, it was difficult to clearly define such effects on the identified modal parameters. Additional data sets continuously or periodically recorded would help to investigate the variability of such modal parameters, reducing uncertainties in the estimates.

Table 2. Identified natural frequencies and damping ratios for vertical (V) modes

Mode	Frequencies (Hz)			Damping ratios [%]		Description
	This study	[1]*	[2]†	This study	[1]*	
V1	0.179 - 0.197	0.201	0.15	2.25 - 6.97	1.36	Anti-symmetric
V2	0.192 - 0.196	0.193	0.19	0.26 - 1.49	0.21	Symmetric
V3	0.257 - 0.259	0.258	0.25	0.04 - 0.96	0.23	Symmetric
V4	0.347 - 0.352	0.350	0.36	0.07 - 0.57	0.20	Anti-symmetric
V5	0.402 - 0.413	0.414	0.39	0.47 - 2.17	0.13	Anti-symmetric: north-span
V6	0.476 - 0.485	0.483	0.48	0.30 - 0.49	0.21	Symmetric
V7	0.555 - 0.563	0.561	0.54	0.35 - 1.05	0.15	Symmetric/longitudinal
V8	0.638 - 0.648	0.645	0.68	0.15 - 0.55	0.11	Anti-symmetric
V9	0.789 - 0.801	0.799	-	0.13 - 0.53	0.23	Symmetric

*: the study by Conte et al. [11]; and †: the study by Scanlan and Jones [12]

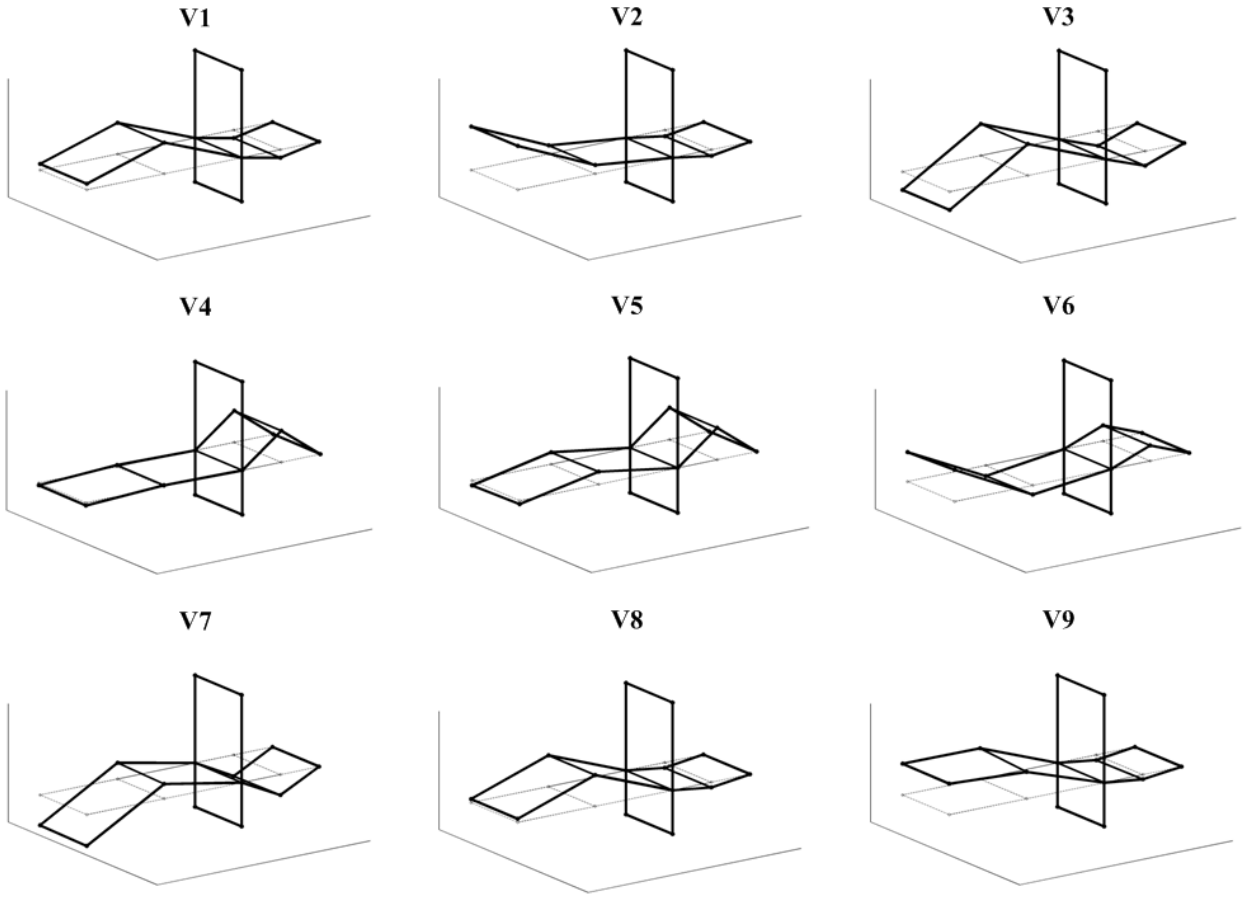

Figure 9. Identified mode shapes for vertical (V) modes

Table 3. Identified natural frequencies and damping ratios for torsional (T), transverse (Tr), and torsion/transverse (TTr) modes

Mode	Frequencies [Hz]			Damping ratios [%]	
	This study	[1]*	[2]†	This study	[1]*
T1	0.458 - 0.469	0.471	0.47	0.05 - 1.18	0.17
T2	0.735 - 0.744	0.741	0.75	0.03 - 0.58	0.34
T3	1.022 - 1.038	-	1.03	0.10 - 0.53	-
Tr1	0.162 - 0.177	-	0.17	0.36 - 1.39	-
Tr2	0.365 - 0.375	-	0.31	0.16 - 1.06	-
Tr3	0.520 - 0.538	-	-	0.23 - 0.58	-
TTr1	0.475 - 0.490	-	-	0.05 - 0.24	-
TTr2	0.500 - 0.510	-	0.58	0.23 - 0.41	-
TTr3	0.940 - 0.978	-	-	0.55 - 0.89	-

*: the study by Conte et al. [11]; and †: the study by Scanlan and Jones [12]

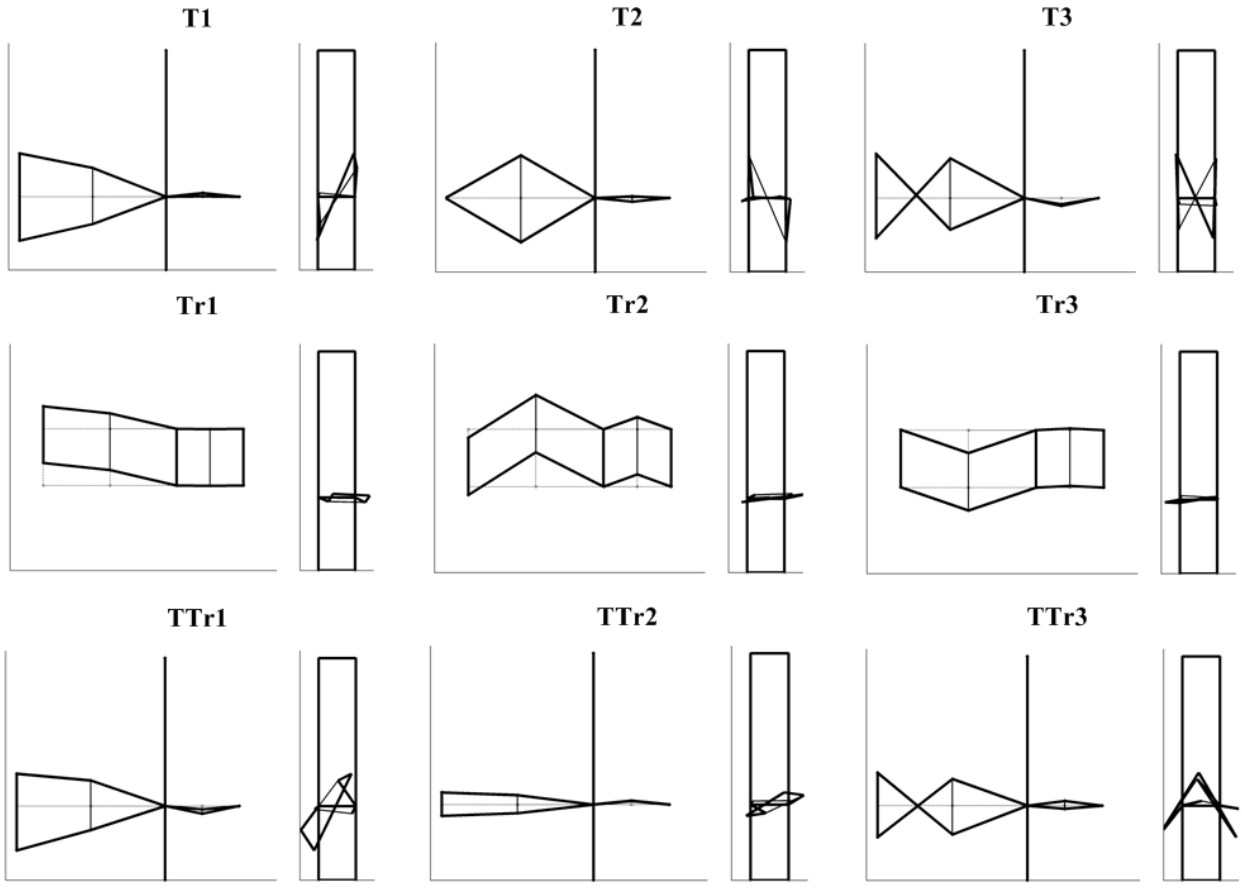

Figure 10. Identified mode shapes for torsional (T), transverse (Tr), and torsion/transverse (TTr) modes

Conclusions

The characterization of dynamic properties of the New Carquinez suspension bridge has been performed by identifying its natural frequencies, damping ratios, and mode shapes, using 17 ambient vibration data sets recorded through the wind-motion monitoring system. By presenting certain bounds of modal parameter estimates for each structural mode identified from the 17 data sets, baseline modal parameters of the bridge were provided for the evaluation of its dynamical behavior in operating condition.

To this end, the data-driven SSI technique was implemented for modal parameters identification, complemented by a stabilization diagram. In the implementation of such technique, three practical issues were first investigated: 1) the dimension of the state needed for a certain number of stable modes to appear in SD; 2) the selection of the order of a realized state-space model to extract stable modes' modal parameters; and 3) the selection of the number of block rows *i* for the projection matrix. After that, the modal parameters for structural modes were identified, for each data set, by examining the estimation error between measured data and reconstructed one from the identified modes.

The identified structural modes of the NCB were represented, in this study, by four groups of modes (vertical, torsional, transverse, and hybrid torsion/transverse modes). Using the acceleration measurements in three orthogonal directions together in the analysis made it possible to characterize the hybrid modes' shapes as well. The frequencies and damping ratios identified in this study showed a good agreement with those presented by the other studies on this bridge. Even though it was observed that the identified frequencies and damping ratios were affected, in a certain way, by the change of wind speed, it was difficult to clearly define such effects because of the limited number of data sets used in this study. For a more in-depth investigation of the variability of damping ratios as well as natural frequencies, additional data sets are needed.

Acknowledgements

The authors would like to acknowledge the support of the California Strong Motion Instrumentation Program (Award number: 1006-903, Project Manager: Dr. Moh Huang) in providing data and resources for the completion of this study.

References

[1] Peeters, B. and De Roeck, G. (2001). "Stochastic system identification for operational modal analysis: a review." *Journal of Dynamic Systems, Measurement, and Control*, **123**: 659-667.

[2] Peeters, B. and Ventura, C.E. (2003). "Comparative study of modal analysis techniques for bridge dynamic characteristics." *Mechanical Systems and Signal Processing*, **17**(5): 965-988.

[3] Zhang, L. Wang, T. and Tamura, Y. (2005). "Frequency-spatial domain decomposition (FSDD) technique for operational modal analysis." *Proceedings of the 1st International Operational Modal Analysis Conference*, Copenhagen, Denmark.

[4] Yu, D.J. & Ren, W.X. (2005). "EMD-based stochastic subspace identification of structures from operational vibration measurements." *Engineering Structures*, **27**: 1741-1751.

[5] Brincker, R., Frandsen, J.B., and Andersen, P. (2000). "Ambient response analysis of the Great Belt Bridge." *Proceedings of the 18th International Modal Analysis Conference*, San Antonio, Texas.

[6] Juang, J. (1994). *Applied System Identification*. Upper Saddle River: Prentice Hall PTR.

[7] Van Overschee, P. and De Moor, B. (1996). *Subspace Identification for Linear Systems – Theory, Implementation, Applications*. Boston: Kluwer Academic Publishers.

[8] Hong, A.L. & Betti, R. (2008). "Identification of the dynamic characteristics of long span bridges using ambient vibration measurements." *Proceedings of the 4th International Conference on Bridge Maintenance, Safety and Management*, Seoul, Korea.

[9] Pridham, B.A. & Wilson, J.C. (2003). "An application example illustrating the practical issues of subspace identification." *Proceedings of the 21st International Modal Analysis Conference*, Kissimmee, Florida.

[10] Pridham, B.A. & Wilson, J.C. (2005). "A reassessment of dynamic characteristics of the Quincy Bay Bridge using output-only identification techniques." *Earthquake Engineering and Structural Dynamics*, **34**: 787-805.

[11] Conte, J.P., He, X., Moaveni, B., Masri, S.F., Caffrey, J.P., Wahbeh, M. Tasbihgoo, F., Whang, D.H and Elgamal, A. (2008). "Dynamic Testing of Alfred Zampa Memorial Bridge." *Journal of structural engineering*, **134**(6): 1006-1015.

[12] Scanlan, R.H. and Jones, N.P. (1998). *Wind Response Study Carquinez Strait Suspended Span*, Report for West Wind Laboratory, Inc. and OPAC Consulting Engineers.

[13] Sun, Z., Min, Z.H. and Zhou, Z.F. (2008). "Baseline knowledge discovery from one-year structural monitoring measurements of Donghai Bridge." *Proceedings of the 4th International Conference on Bridge Maintenance, Safety and Management*, Seoul, Korea.

[14] Kang, S.G., Kwon, J.B., Lee, I.K., and Lee, G.H. (2008). "Structural behaviors of Seohae cable-stayed bridge affected by temperature." *Proceedings of the 4th International Conference on Bridge Maintenance, Safety and Management*, Seoul, Korea.

[15] Yun, H.B., Masri, S.F., Nayeri, R.D., Tasbihgoo, F, Kallinikidou, E., Wahbej, M., Wolfe, R.W., and Sheng, L.H. (2008). "Long-term monitoring of the stochastic characteristics of a full-scale suspension bridge." *Proceedings of the 4th International Conference on Bridge Maintenance, Safety and Management*, Seoul, Korea.

[16] Abe, M. Fujino, Y., Yanagihara, M., and Sato, M. (2000). "Monitoring of Hakucho suspension bridge by ambient vibration measurement." *Proceedings of SPIE*, **3995**:237-244.

GROUND MOTION TASKS IN THE TALL BUILDINGS INITIATIVE

Yousef Bozorgnia and Jack P. Moehle

Pacific Earthquake Engineering Research Center (PEER),
University of California, Berkeley, CA 94720-1792

ABSTRACT

The Tall Buildings Initiative (TBI) is a major multidisciplinary program coordinated by the Pacific Earthquake Engineering Research Center (PEER) in collaboration with numerous local, state and federal organizations. The goal of TBI is to address critical technical issues on seismic analysis and design of new tall buildings located in coastal California. This paper provides an overview of the TBI tasks on ground motion issues.

INTRODUCTION

The west coast of the United States is seeing a surge in the design and construction of tall buildings (defined here as buildings 240 feet, 73 meters, or taller). For example, at the time of this writing, there are more than 100 tall buildings under construction or in various planning stages in San Francisco and Los Angeles. Many of these buildings use high-performance materials and framing systems that have not been commonly used for building construction, or that fall outside the height limits, of current buildings codes. Increasingly, nonlinear dynamic analysis is being used in a performance-based design approach to demonstrate the seismic performance of buildings that do not satisfy all the prescriptive provisions of the building code. To carry out such nonlinear dynamic analyses, input ground motions representative of the regional and local seismic hazards are needed.

The Pacific Earthquake Engineering Research Center (PEER) is leading the *Tall Buildings Initiative* (TBI) to coordinate and fund a range of short to intermediate-term projects. The final product will be a set of written guidelines containing principles and specific criteria for tall building seismic design. The document is intended to support ongoing guidelines and code-writing activities of collaborating organizations, as well as being a stand-alone reference for designers of high-rise buildings.

The TBI has formulated projects to address key ground motion issues for analysis of tall buildings. This paper provides an overview of the on-going research on ground motion issues for tall buildings.

GROUND MOTION TASKS IN TALL BUILDINGS INITIATIVE

Selection and modification of ground motion time series to represent a specific hazard at a site has a large impact on the results of nonlinear response history analyses using these input motions, indicating the need to establish rational procedures for ground motion selection, scaling and modification. Validated seismological methods may be used to generate ground motion time

series that incorporate near-fault rupture directivity effects and basin effects, and appropriately represent the duration and long period energy content of these large design events.

In the TBI, there are various tasks related to ground motion issues for tall buildings. The related TBI tasks and their progress are summarized below.

TBI Task 3 – Assessment of ground motion selection and modification procedures

In this task, comprehensive nonlinear response analyses of realistic tall building computer models are carried out (Moehle, *et al.*, 2007). The models include various reinforced concrete core wall as well as reinforced concrete moment frames. Each building model has its own unique floor dimension and building height. The computer models are subjected to a large number of un-scaled and scaled earthquake ground motions to determine the native statistics of the responses. For example, Figure 1 shows story shears in a building model subjected to numerous ground motions. The results are also compared with those obtained using various proposed Ground Motion Selection & Modification (GMSM) procedures, and recommendation will be made about appropriate GMSM. This task is conducted in coordination with the PEER GMSM program, a separate research program dealing with GMSM for various structural systems.

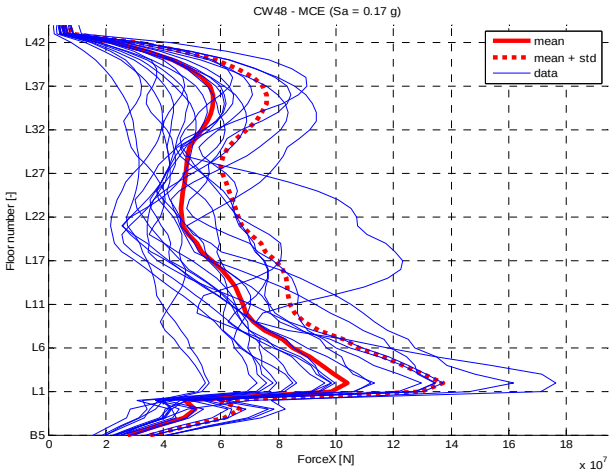

Figure 1 – Story shears in a case study core-wall building, from nonlinear response history analysis, for ground motions scaled so the first-mode spectral acceleration matches the uniform hazard level value at the MCE hazard level (Moehle, *et al.*, 2007)

TBI Task 5 - Synthetically generated ground motions

Using validated broadband ground motion simulation procedures, ground motion time series are being simulated for San Francisco and Los Angeles sites for large earthquakes on the major faults in the region. The time series will be simulated for geographic areas of specific interest in San Francisco and Los Angeles. These simulated broadband time series are to contain long period effects such as rupture directivity effects and basin effects that are specific to the fault geometry and geological structure of the regions.

As an example, Figure 2 shows the results of broadband ground motion simulations (Graves and Somerville, 2006; Bozorgnia, *et al.*, 2007) for a large earthquake occurring on the Puente Hills fault system in Los Angeles (Shaw *et al.*, 2002). The top left side shows a map view of the Los Angeles region indicating the location of one segment of the Puente Hills fault. The right side shows snapshots of the wave field at times of 6, 15, and 24 seconds after the origin time of the earthquake. At 6 seconds, the main feature of the ground motion is the strong rupture directivity pulse, directed updip toward the west-southwest toward downtown Los Angeles from the hypocenter, which is located at the northwest corner near the bottom of the fault plane. The

ground motions are far weaker in other directions around the fault. At 15 seconds, this directivity pulse has propagated into the Los Angeles basin, becoming trapped within the basin and giving rise to large ground motions. This basin effect is progressively accentuated at 24 seconds. The lower set of time histories at the bottom left of Figure 2 shows the long duration and long period nature of these basin waves in Long Beach, in contrast with the much briefer and shorter period motions in downtown Los Angeles caused by the rupture directivity pulse.

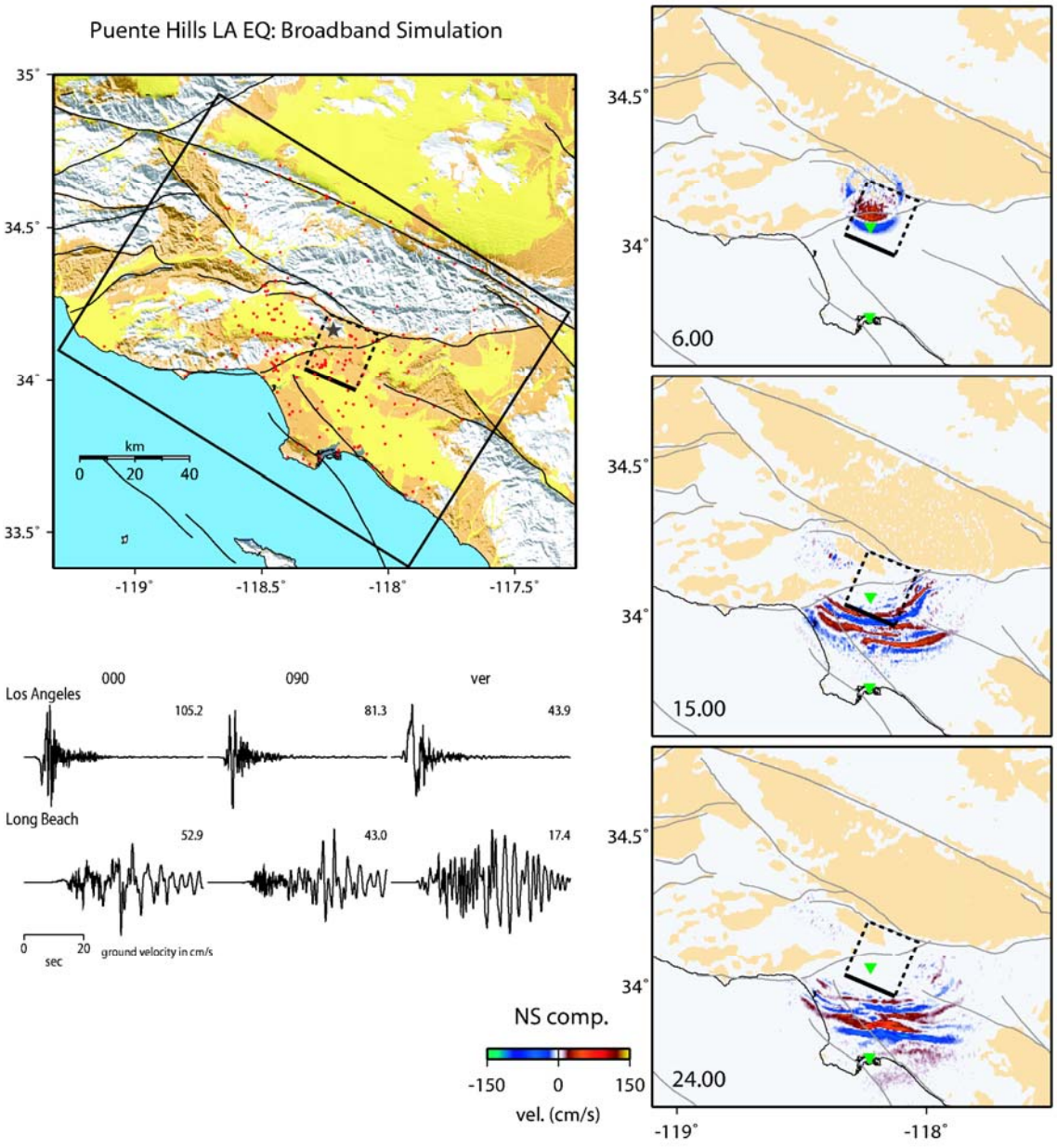

Figure 2. Snapshots of the simulated ground motion wave field (right) from a scenario earthquake on the Puente Hills Blind Thrust fault shown as a black square (top left). The simulated ground motion velocity waveforms in downtown Los Angeles (green triangle above the fault) and in Long Beach (green triangle on the southern shore) are shown on the bottom right (Graves and Somerville, 2006).

TBI Task 6 – Review and validation of synthetically generated ground motions

A review of procedures and results obtained in Task 5 is carried out with the purpose of establishing a validated reference set of synthetically generated broadband ground motions. Working closely with researchers in Task 5, the goal is to ensure that the final results are based on the best available technologies and assumptions, and are properly interpreted. The review will be carried out by both seismologists and engineers.

In this task comprehensive comparisons of the simulated ground motions with the results of Next Generation Attenuation (NGA) are carried out. The NGA models are mainly based on the recorded ground motions (Power, *et al.*, 2008); therefore, this task will reveal the differences between the recorded and simulated ground motions. Example results of NGA model developed by Campbell and Bozorgnia (2007, 2008) are presented in Figure 3.

Elastic and inelastic spectra for thousands of simulated ground motions for the Puente Hills blind Thrust Fault have been computed. The on-going task is to compare the characteristics of these spectra with those of the NGA recorded motions (e.g., as presented in Figure 3). Recently Stewart, *et al.,* (2008) compared characteristics of the simulated ground motions for the Puente Hills scenario and those of the NGA. Figure 4 shows "event terms" for the simulated Puente Hills event (Stewart, *et al.,* 2008). The results are shown for spectral accelerations at several periods ranging from 0.1 to 10 sec. The dashed lines shown in Figure 4 indicate ± one inter-event standard deviation. The simulation event terms generally fall within a reasonable range, mostly within one standard deviation (Stewart, *et al.,* 2008). Figure 5 presents the intra-event residual (versus distance) between the Puente Hills simulated ground motions and Campbell & Bozorgnia (2008) NGA empirical model. The figure shows slightly faster distance-attenuation of the simulated data relative to the NGA model (Stewart, *et al.,* 2008). The apparent bias in the distance scaling is much smaller for the Puente Hills event than for a previously investigated large magnitude southern San Andreas fault rupture.

The same process of comparison between simulation motions and NGA models will be repeated for the northern and southern San Andreas Fault and Hayward Fault in California. In addition to the elastic spectra, inelastic response spectra of the NGA database (Bozorgnia, *et al.,* 2006, 2008) will be compared with those of simulated ground motions.

TBI Task 7 - Guidelines on selection and modification of ground motions for design

Using findings from Tasks 5 and 6, a team of scientists and engineers will write practical guidelines for the selection and modification of ground motions for analysis of tall buildings. The recommended procedures will be applied to virtual sites in San Francisco and Los Angeles to both demonstrate the procedures and establish a sample set of validated ground motions that can be used in subsequent research or for tall-building design.

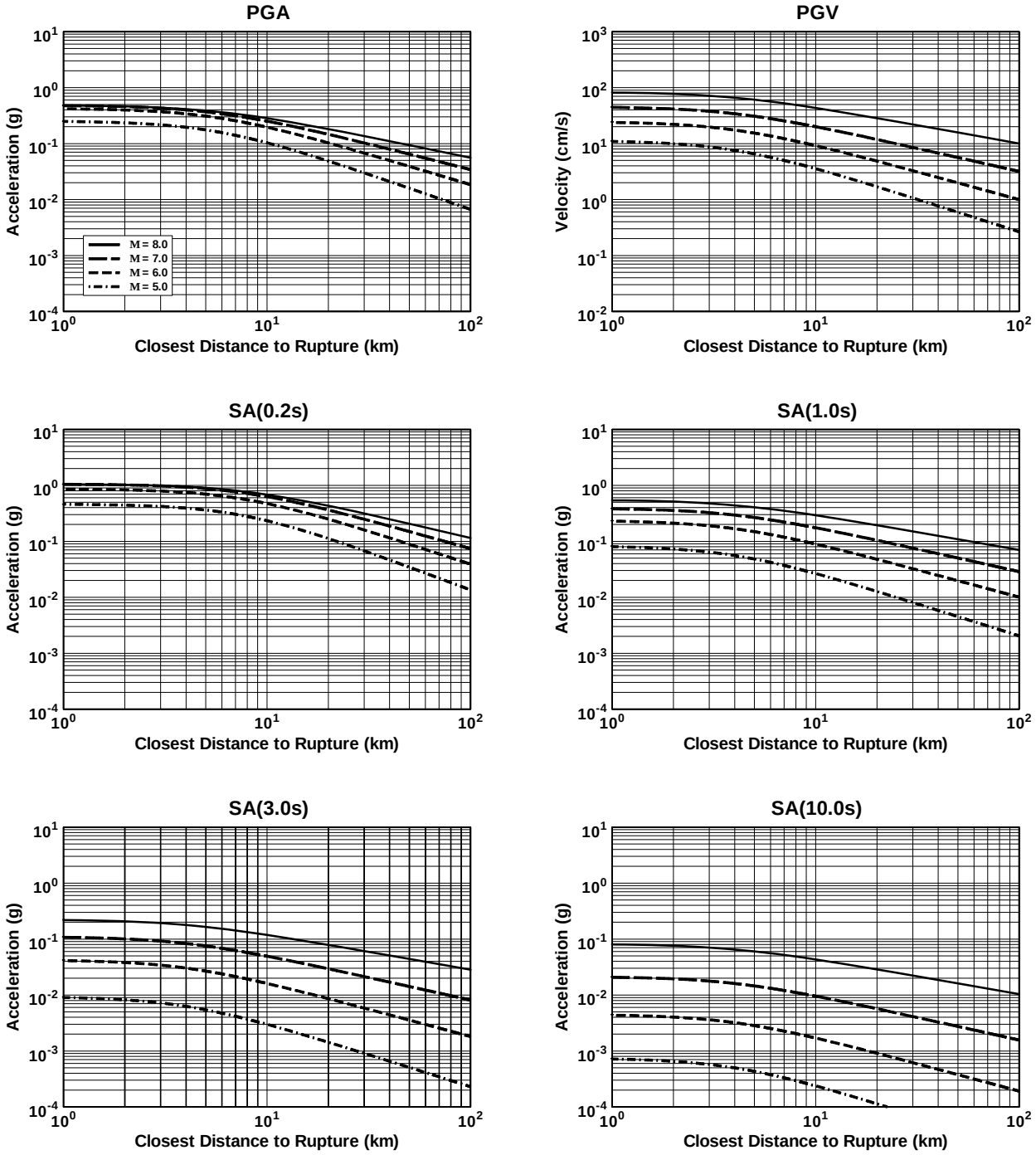

Figure 3. Example results of NGA model by Campbell and Bozorgnia (2007, 2008).

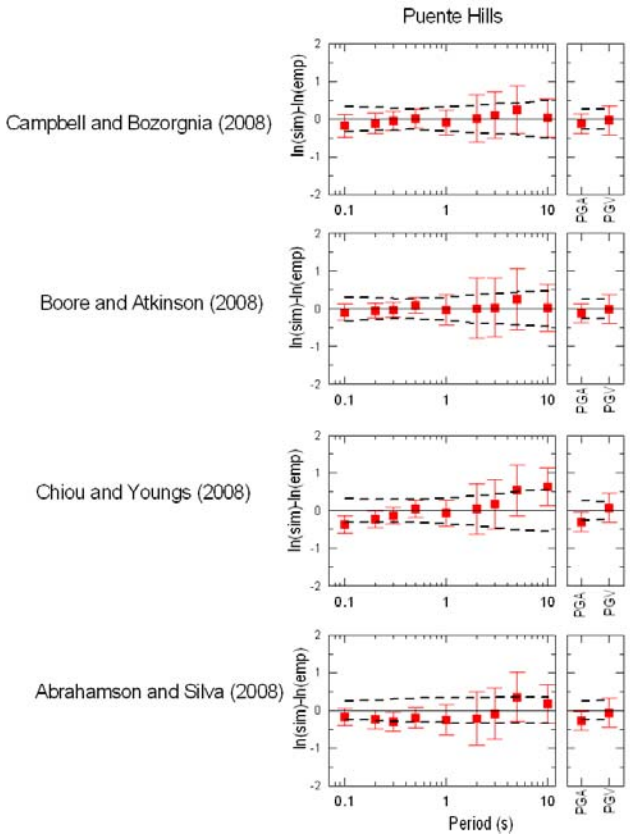

Figure 4. Event terms for the simulated Puente Hills earthquake as compared with those of NGA empirical models. The error bars indicate one standard deviation for the residuals. The heavy dashed line represents the inter-event standard deviations from the empirical model (Stewart, *et al.*, 2008).

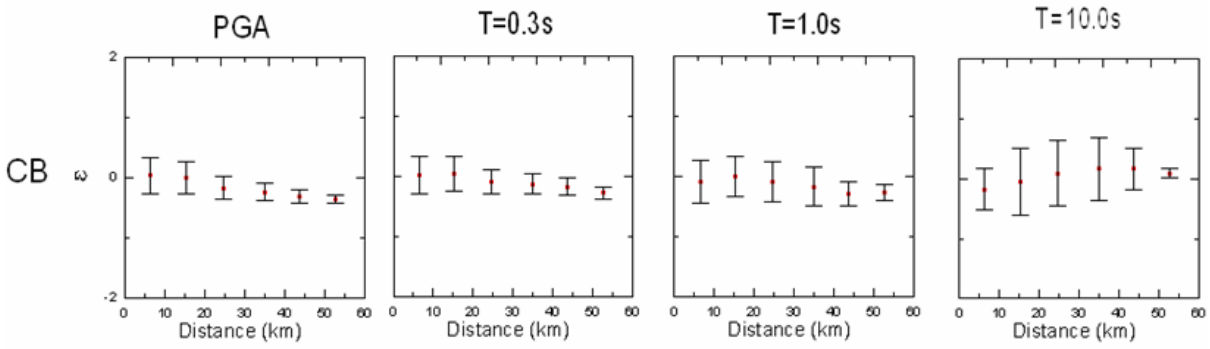

Figure 5: The intra-event residuals of the Puente Hills simulated motions relative to the Campbell & Bozorgnia (2008) NGA model for PGA and spectral ordinates at periods *T*=0.3, 1.0, and 10.0 sec versus rupture distance (Stewart, *et al.*, 2008).

ACKNOWLEDGEMENTS

TBI involves numerous partners and sponsors including (alphabetically): Applied Technology Council, California Office of Emergency Services, California Seismic Safety Commission, California Strong Motion Instrumentation Program, Charles Pankow Foundation, Federal Emergency Management Agency, Los Angeles Department of Building and Safety, Los Angeles Tall Buildings Structural Design Council, National Science Foundation, San Francisco Department of Building Inspection, Southern California Earthquake Center, Structural Engineers Association of California, U.S. Geological Survey, and several practicing professionals. Supports and cooperation of all organizations and individuals are gratefully appreciated.

REFERENCES

Bozorgnia, Y., Hachem, M. and Campbell, K.W., 2006. "Attenuation of Inelastic and Damage Spectra", *Proceedings of the 8th National Conference on Earthquake Engineering*, San Francisco, CA, April 2006, Paper 1127.

Bozorgnia, Y., Hachem, M. and Campbell, K.W., 2008. "Direct Hazard Analysis of Inelastic Response Spectra," *Proceedings of the 14th World Conference on Earthquake Engineering*, Beijing, China, October 12-17, 2008.

Bozorgnia, Y., Campbell, K.W., Luco, N., Moehle, J.P., Naeim, F., Somerville, P., and Yang, T.Y. 2007. "Ground Motion Issues for Seismic Analysis of Tall Buildings: A Status Report,' *The Structural Design of Tall and Special Buildings*, **16**, 665-674.

Campbell, K.W. and Bozorgnia, Y., 2007. "Campbell-Bozorgnia NGA Ground Motion Relations for the Geometric Mean Horizontal Component of Peak and Spectral Ground Motion Parameters", *Report PEER 2007/02*, Pacific Earthquake Engineering Research Center (PEER), University of California, Berkeley, May 2007.

Campbell, K.W. and Bozorgnia, Y., 2008. "NGA Ground Motion Model for the Geometric Mean Horizontal Component of PGA, PGV, PGD and 5% Damped Linear Elastic Response Spectra for Periods Ranging from 0.01 to 10 s", *Earthquake Spectra*, **24**, 139-171.

Graves, R.W. and Somerville, P.G., 2006. "Broadband Ground Motion Simulations for Scenario Earthquakes on the Puente Hills fault." *Proceedings of the Eighth National Conference on Earthquake Engineering*, San Francisco, California, U.S.A., Paper No. 1052, Earthquake Engineering Research Institute.

Moehle, J.P., Bozorgnia, Y. and Yang, T.Y., 2007. "The Tall Buildings Initiative", *Proceedings of the 2007 Convention of the Structural Engineers Association of California*, September 26-29, 2007, South Lake Tahoe, California.

Power, M., Chiou, B., Abrahamson, N.A., Roblee, C., Bozorgnia, Y. and Shantz, T., 2008. "An Introduction to NGA" *Earthquake Spectra*, **24**, 3-21.

Shaw, J.H., Plesch, A., Dolan, J.F., Pratt, T.L. and Fiore, P., 2002. "Puente Hills Blind-Thrust System", Los Angeles, California", *Bull. Seism. Soc. Am.* **92**, 2946-2960.

Stewart, J.P., Star, L.M., and Graves, R.W., 2008. "Validation Against NGA Empirical Model of Simulated Motions for M7.15 Rupture of Puente Hills Fault," *Final Report* to Pacific Earthquake Engineering Research Center (PEER), University of California, Berkeley.

PRELIMINARY SUMMAY OF STRONG-MOTION RECORDS FROM THE M8.0 SICHUAN, CHINA EARTHQUAKE OF MAY 12, 2008

Xiaojun Li[1], Zhenghua Zhou[1] and Moh Huang[2]

[1]Institute of Engineering Mechanics, China Earthquake Administration, Harbin, China
[2]California Geological Survey, Sacramento, USA

Summary

At 14:28 on May 12, 2008 (Beijing and Sichuan Time), a great earthquake occurred in Sichuan province, China, with a surface wave magnitude of 8.0. The earthquake epicenter was located in Wenchuan County at latitude 31.021°N and longitude 103.367°E, and a focal depth of 14 km. The associated fault rupture is mainly thrust with a strike-slip component on the Longmenshan fault belt. However, the source mechanism is quite complex. The rupture process is mainly unilateral with the main rupture spreading to the northeast about 300 km from the epicenter The post-earthquake geological studies found a 200 km long surface rupture along the central branch of the Longmenshan fault belt (i.e Yingxiu-Beichuan fault) and a rupture of 60 km along the front branch (i.e. Guanxian-Jiangyou fault). As of August 29, 2008, a total of 261 aftershocks with magnitude larger than 4.0 have occurred. Among them, 31 aftershocks were larger than 5.0, and 8 aftershocks larger than 6.0. The largest aftershock occurred on May 25 with a magnitude of 6.4.

The China Digital Strong Motion Observation Network was completed in March 2008 after nearly five years of construction and trial operation, resulting in a broad distribution of observation stations in China and intensive distribution in some local areas. During the Wenchuanearthquake of May 12, strong-motion records were obtained from about 460 permanent ground stations and three arrays for topographical effect and structural response observation. After the main shock, 59 mobile instruments were quickly deployed in the hard hit areas to record ground motions generated by strong aftershocks.

A total of about 1,400 components of ground motions from the main shock were recorded, and as of 1 August 2008, over 20,000 components from strong aftershocks have been recorded. For the mainshock records, there are more than 500 components with peak acceleration larger than 10 gal (cm/sec/sec), 200 larger than 50 gal, 115 larger than 100 gal, 42 larger than 200 gal, 16 larger than 400 gal, and 7 larger than 600 gal, and no records over 1000 gal.

The largest peak ground acceleration from the main shock is 958 gal recorded at Wolong station in Wenchuan County, Sichuan. Recorded peak accelerations and preliminary peak velocity values from some key stations along the fault are listed below:

Wolong station in Wenchuan County:
Epicentral distance = 19 km; Distance to Yingxiu-Beichuan fault = 23 km
PGA (gal) - 957.7 (EW), 652.9 (NS), 948.1 (UD)
PGV (cm/s) - 51.5 (EW), 41.7 (NS), 30.4 (UD)

Bajiao station in Shifang City:
Epicentral distance = 67 km; Distance to Yingxiu-Beichuan fault = 10 km
PGA (gal) – 556.2 (EW), 581.6 (NS), 633.1 (UD)
PGV (cm/s) – 62.7 (EW), 89.8 (NS), 49.6 (UD)

Qingping station in Mianzhu City:
Epicentral distance = 88 km; Distance to Yingxiu-Beichuan fault = 3 km
PGA (gal) – 824.1 (EW), 802.7 (NS), 622.9 (UD)
PGV (cm/s) – 133.0 (EW), 65.3 (NS), 39.6 (UD)

Zengjia station in Guanyuan City:
Epicentral distance = 314 km; Distance to Yingxiu-Beichuan fault = 86 km
PGA (gal) – 424.5 (EW), 410.5 (NS), 183.3 (UD)
PGV (cm/s) – 44.0 (EW), 25.8 (NS), 24.6 (UD)

Preliminary analysis of these strong-motion records shows the following characteristics of ground motion from the earthquake, especially for near-fault ground motion:

（1） Large peak accelerations are recorded from stations located along the fault, and the distance to the rupturing fault, rather then the epicentral distance, clearly controls the ground motion attenuation.

（2） Peak accelerations at stations in the fault rupture propagation direction are relatively large, consistent with the fault rupture propagation or directivity effect.

（3） In the near-fault records, peak acceleration in the EW direction is in general larger than that in the NS direction.

（4） Peak accelerations at stations on hanging wall of the thrust fault are generally larger than those from stations on footwall, which shows hanging wall effect on ground motion.

（5） The area with large accelerations seems to be relatively larger near the northeast segment of the fault than the southwest segment of the fault.

（6） For some near-fault records peak acceleration is larger in the vertical direction than in one or two horizontal directions.

（7） Large velocity pulses of the ground motion appear in some near-fault records.

Peak ground accelerations for both horizontal components from the main shock versus the distance to the fault were compared with other ground motion attenuation relationships. The peak horizontal ground accelerations of the Wenchuan Earthquake decrease much more slowly than those from other attenuation relationships, especially in the fault distance ranging from 100 to 300 km. Some recorded peak values are about 100 gal even at the fault distance of about 400 km. The peak ground acceleration is highly varied in the fault distance ranging from 100 to 500 km.

IMPRESSIONS FROM A FIELD INVESTIGATION OF THE WENCHUAN, SICHUAN PROVINCE, EARTHQUAKE OF MAY 12, 2008

Marshall Lew, David A. Friedman and Laurie A. Johnson

Members of the Earthquake Engineering Research Institute (EERI)
Field Investigation Team

INTRODUCTION

A team of earthquake researchers, sponsored by the Earthquake Engineering Research Institute (EERI) and the Geo-Engineering Earthquake Reconnaissance (GEER) Association, carried out a field investigation in conjunction with Chinese colleagues from August 4th to 10th to document scientific and engineering effects of the devastating earthquake (moment magnitude 7.9 according to the USGS) that occurred in Wenchuan County of Sichuan Province, China, on May 12, 2008. The EERI field investigation was conducted as part of the Learning from Earthquakes Program with funding from the National Science Foundation (NSF).

The EERI-GEER field investigation team was invited by Prof. Zifa Wang, Director of the Institute of Engineering Mechanics-China Earthquake Administration (IEM-CEA), to investigate the effects of the Wenchuan earthquake. During the short period of one week in the field, the EERI-GEER team could only get a small sample of the effects of the great earthquake. Prof. Junwu Dai of the IEM-CEA accompanied the team during the field investigation.

The research team, under the leadership of Dr. Marshall Lew of MACTEC Engineering and Consulting in Los Angeles, California, included experts in structural, lifelines, and geotechnical engineering as well as disaster response and recovery. In addition to Dr. Lew, EERI team members were David Friedman and Dennis Lau of Forell/Elsesser Engineers, Inc., and Laurie Johnson, an urban planning consultant, all of San Francisco, California; Prof. Tricia Wachtendorf of the Disaster Research Center at the University of Delaware in Newark; and Prof. Jian Zhao of the University of Wisconsin at Milwaukee. The GEER team consisted of Prof. David Frost of the Georgia Institute of Technology in Savannah, Prof. J. P. Bardet of the University of Southern California in Los Angeles, and Prof. Tong Qiu of Clarkson University in Potsdam, New York.

This paper presents observations made during the EERI-GEER field investigation in Sichuan Province as well as observations made by other investigators who have visited the earthquake-affected region. Information from other sources have also been incorporated.

EARTHQUAKE SETTING

The May 12, 2008 Great Wenchuan Earthquake is the worst earthquake to strike China since the magnitude 7.8 Tangshan event of July 27, 1976 that claimed an estimated 242,000

lives. The May 12 earthquake affected more than 100,000 square miles and about 30 million people. It caused the deaths of 69,226 people (as of August 21, 2008) with 17,923 missing, injured almost 375,000 others, caused almost 1.5 million to be relocated (Xinhua, 2008). The earthquake also caused destruction of more than 216,000 buildings in Sichuan Province, including approximately 6,900 school buildings, whose collapses buried thousands of students and teachers. The location of the May 12, 2008 earthquake and major aftershocks through May 28, 2008 are shown in Figure 1.

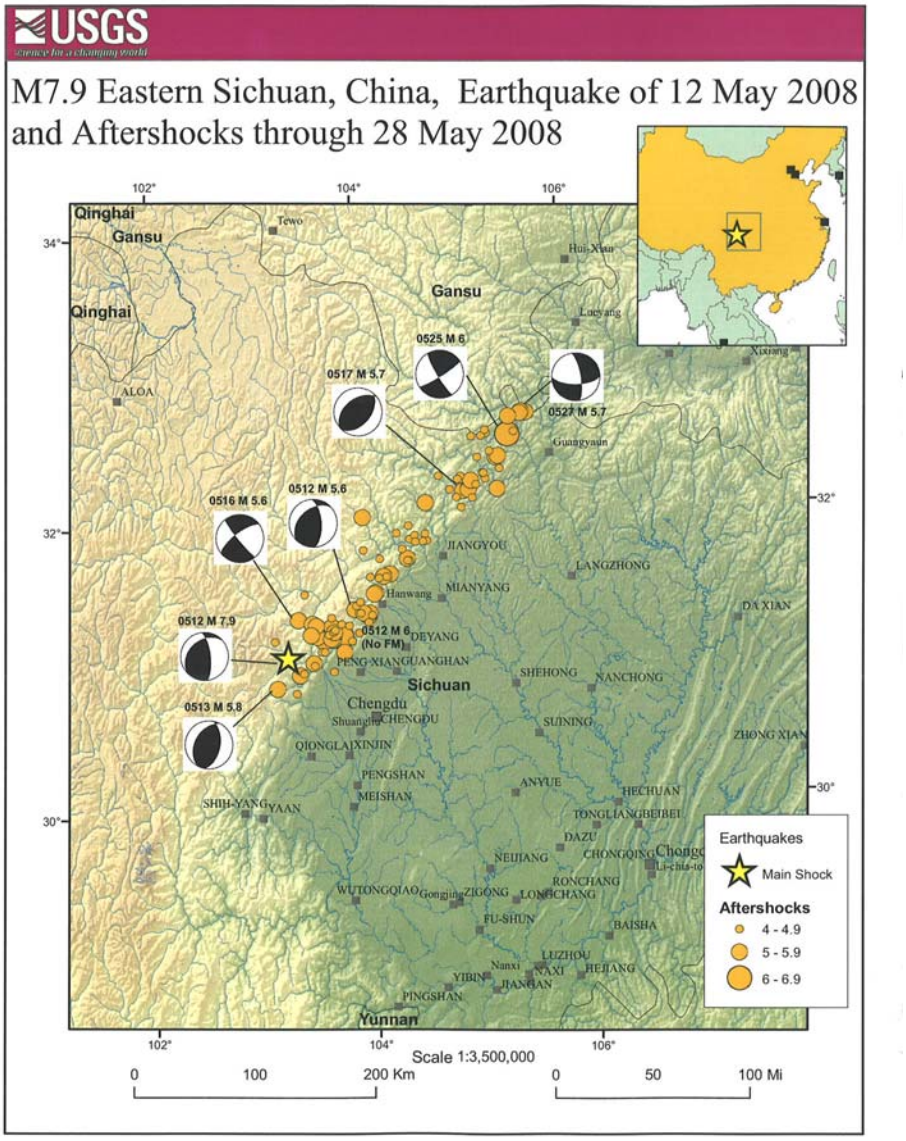

Fig.1 Locations of Wenchuan Earthquake May 12, 2008 Mainshock and Aftershocks through May 28, 2008 (United States Geological Survey, 2008)

The earthquake originated on the Longmenshan fault, a northeastern striking thrust fault that ruptured for almost 300 kilometers. The fault is the result of convergence of crust from the high Tibetan Plateau to the west, against the strong and stable crust block underlying the Sichuan

Basin and southwest China to the east. On a continental scale, the seismicity of central and eastern Asia is a result of northward convergence of the Indian plate against the Eurasian plate. This convergence of the two plates is broadly accommodated by uplift of the Asian highlands and by the motion of crustal material to the east away from the uplifted Tibetan Plateau. Thus India is moving northward pushing into central Asia and pushing Tibet eastward, overriding the Sichuan basin. The tectonic setting is shown in Figure 2. The geology of the Wenchuan earthquake area and the Longmenshan fault zone are shown in Figure 3. A cross section across the Longmenshan fault zone is shown in Figure 4.

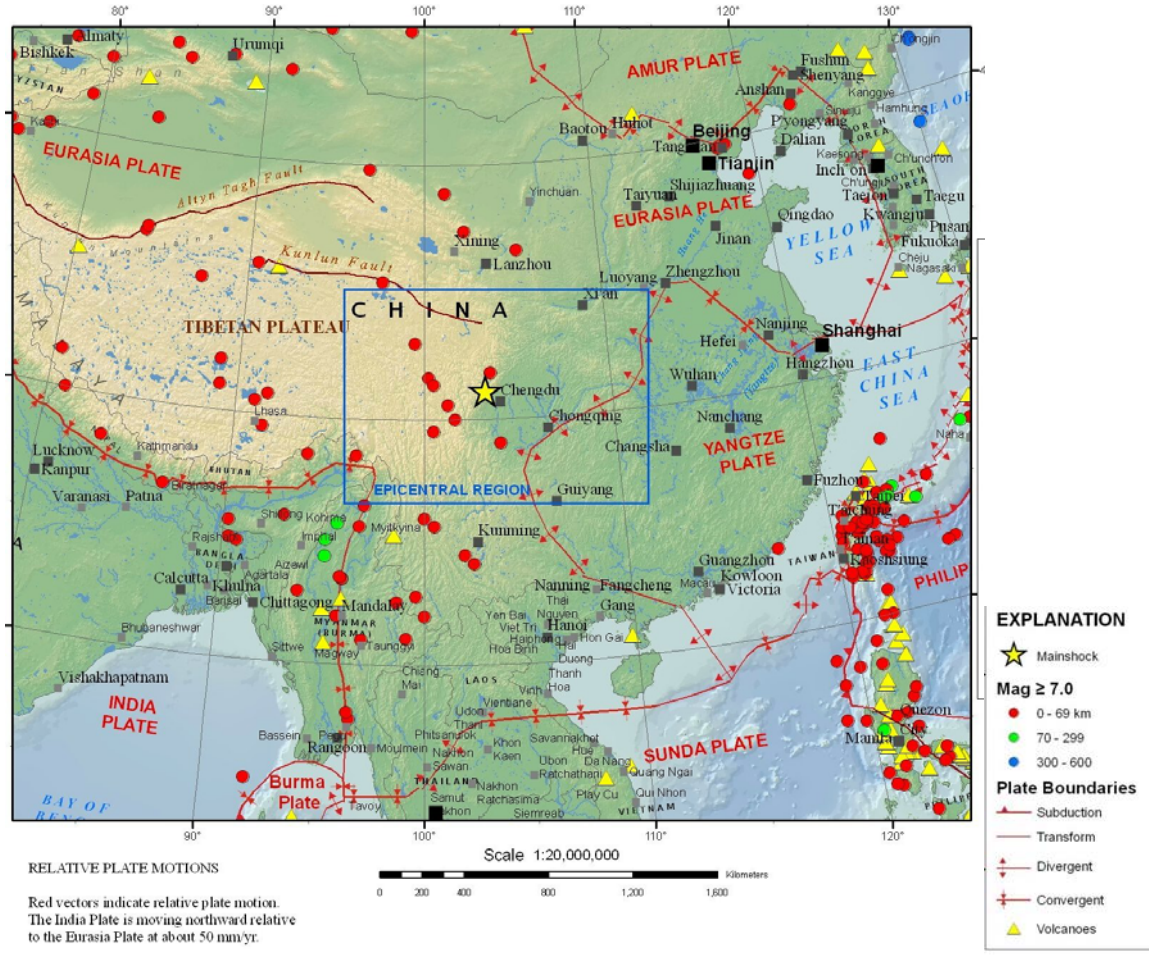

Fig. 2 Tectonic Setting of the Wenchuan Earthquake (United States Geological Survey, 2008)

Previous earthquakes have been experienced along the northwestern margin of the Sichuan Basin. On August 25, 1933, a magnitude 7.3 earthquake resulted in over 6,800 deaths with another 2,500 persons perishing later as a result of the failure of a “quake lake” dam caused by an earthquake-induced landslide. The Wenchuan earthquake occurred within the context of long-term uplift and eastward enlargement of the Tibetan plateau; the average recurrence interval of the Wenchuan earthquake has been estimated to be in the general range of 2,000 to 10,000 years by Burchfiel et al. (2008).

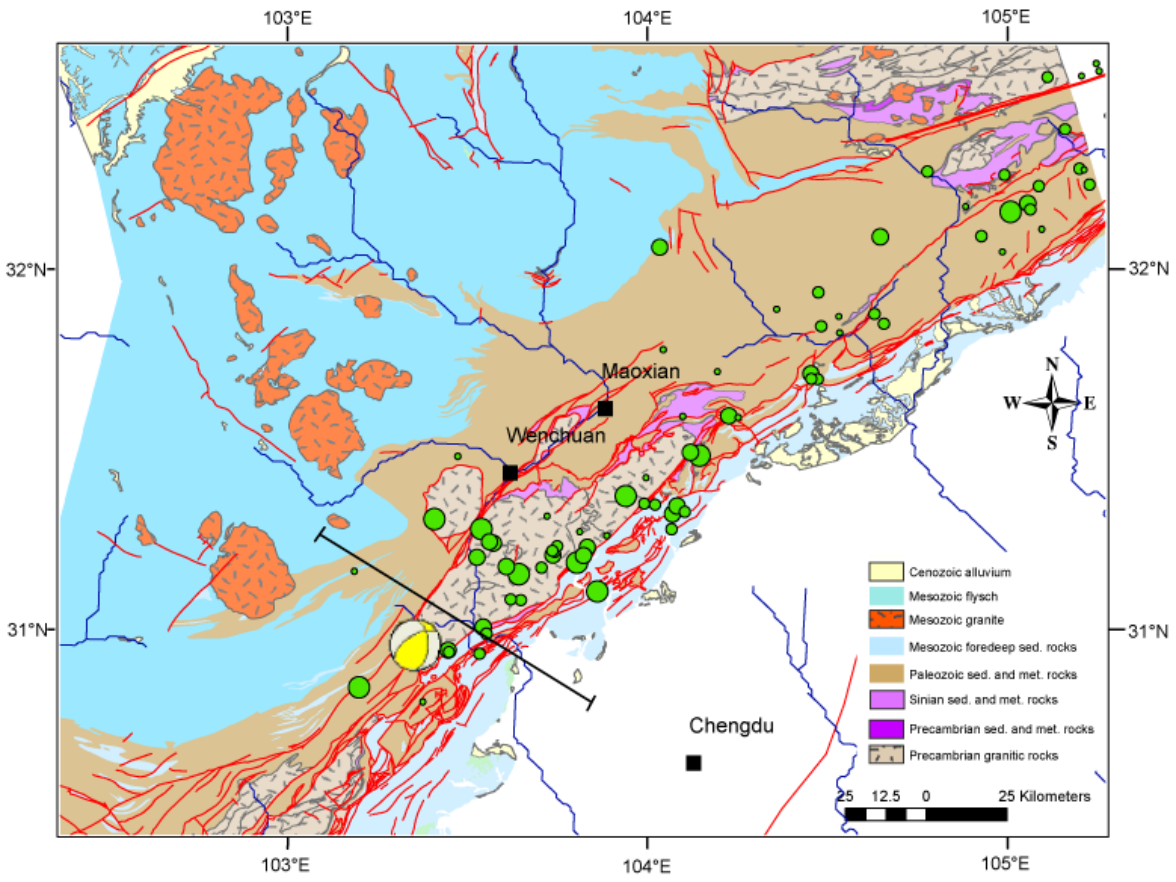

Fig. 3 Geologic Map of the Wenchuan Earthquake Area (Massachusetts Institute of Technology Department of Earth, Atmospheric, and Planetary Sciences, 2008)

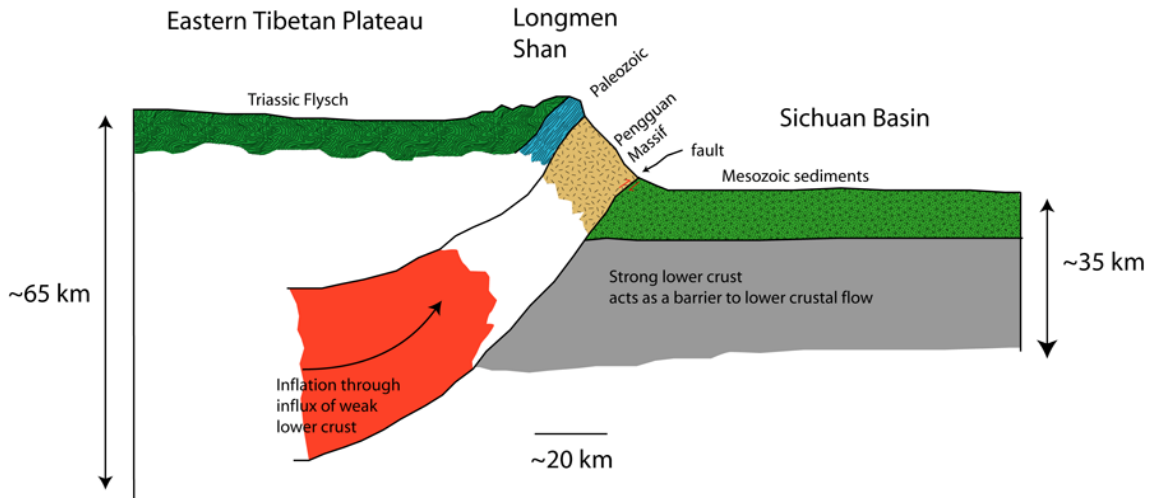

Fig. 4 Cross Section of Longmenshan Fault Zone (Massachusetts Institute of Technology Department of Earth, Atmospheric, and Planetary Sciences, 2008)

Because large earthquakes were rare before the May 12 earthquake, basic design levels in the Sichuan region were established at Intensity VII (Modified Mercalli Scale). School buildings were considered as Category C buildings, which is the same as for regular buildings.

GROUND MOTIONS

Strong ground motion was measured at about 200 stations established by the China Earthquake Administration. The strong motion time histories have not yet been made available to the research community. Three recordings were shown to the EERI-GEER team during our China investigation. One record was obtained at a distance of 22 km from the epicenter and 1.0 km from the fault had a peak ground acceleration (PGA) of around 957 gal and a duration of nearly 60 seconds. In a recording made 88 km from the epicenter, and 1.0 km from the fault, the PGA was 802 gal and had a strong ground shaking duration of 90 seconds. At 150 km from the epicenter, and 75 km from the fault, a third recording gave a PGA of 550 gal with a strong shaking duration of 150 seconds.

Plots of the PGA contours developed by CEA are shown in Figures 5, 6, and 7 for the north-south, east-west, and vertical components.

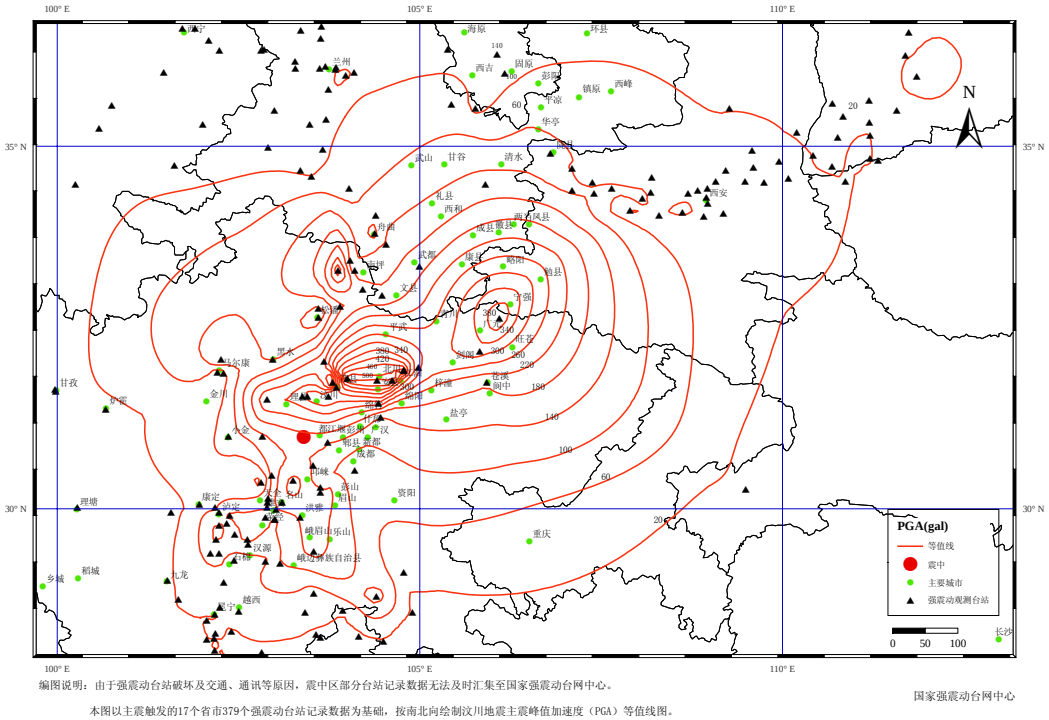

Fig. 5 Distribution of North-South Peak Ground Accelerations (Courtesy of the Institute of Engineering Mechanics-China Earthquake Administration)

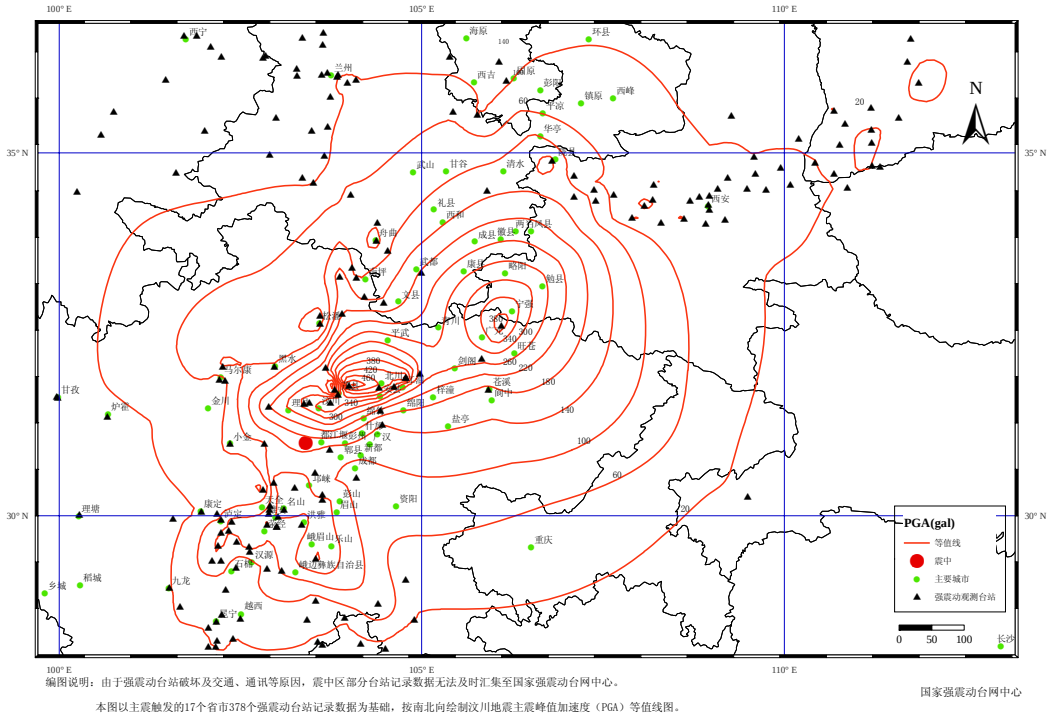

Fig. 6 Distribution of East-West Peak Ground Accelerations (Courtesy of the Institute of Engineering Mechanics-China Earthquake Administration)

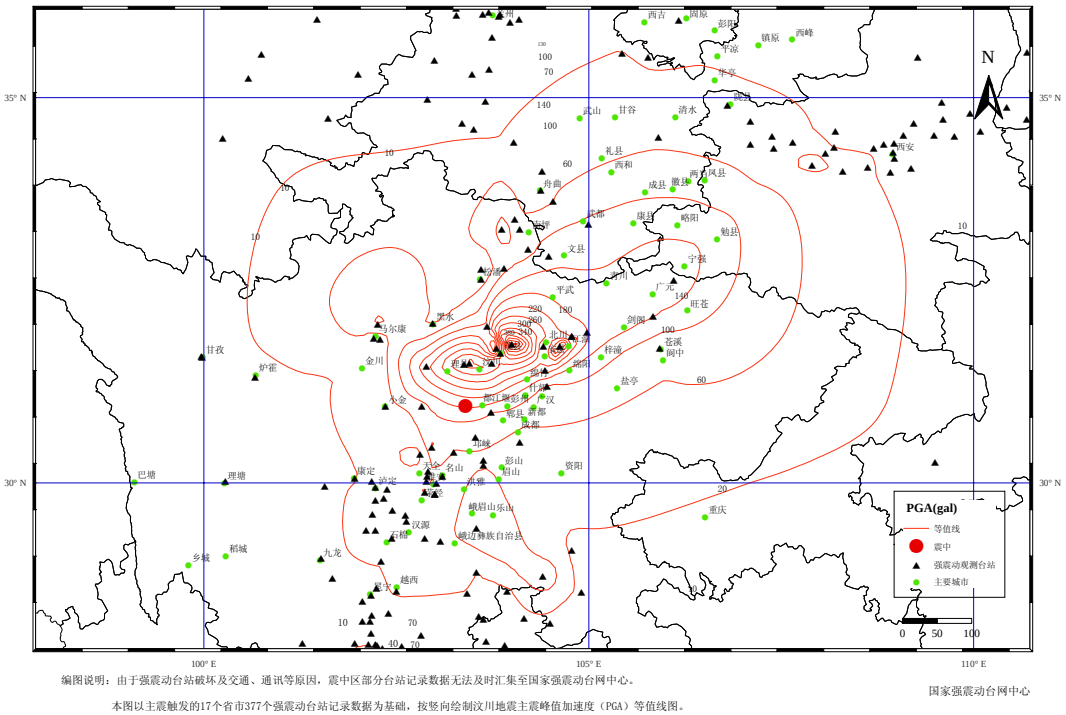

Fig. 7 Distribution of Vertical Peak Ground Accelerations (Courtesy of the Institute of Engineering Mechanics-China Earthquake Administration)

GEOTECHNICAL OBSERVATIONS

The major geotechnical effects in the Wenchuan earthquake were: the numerous landslides triggered by the mainshock and aftershocks; and the complex fault rupture. Soil liquefaction was not a prominent feature of this earthquake as it was in previous events such as the 1999 Kocaeli, Turkey or Chi-Chi, Taiwan earthquakes.

Landslides

The Longmenshan Mountains are prone to numerous landslides just due to the topography and steepness of the mountains under normal conditions. The earthquake is reported to have caused almost 10,000 landslides. Some 26 landslides are believed to have volumes exceeding 10 million cubic meters of material. Landslides and rockslides buried villages and towns resulted in numerous fatalities, with two landslides killing about 2,500 persons in the Beichaun area. Landslides near Beichuan also dammed the river and created the Tangjiashan Quake Lake, which was a threat to downstream towns and villages should the landslide mass be breached or overtopped; see Figure 8. The China People's Liberation Army deployed troops to cut channels through the slide to stop the rising water and reduce the risk of a catastrophic failure of the landslide dam and resulting flooding downstream.

Fig. 8 Tangjiashan Quake Lake near Beichuan (source: National Survey Bureau)

Figure 9 shows the foot of a landslide that originated from the top of the mountains and buried a village of about 70 persons near Yinchanggou. Figure 10 shows massive rockslides near Shenxigou. Figure 11 shows a typical large rock from a rockslide on a road into the Longmenshan Mountains. Figure 12 shows rockslide damage to a resort hotel in Shenxigou.

Fig. 9 Landslide near Yinchanggou

Fig. 10 Massive rockslides near Shenxigou

Fig. 11 Large rocks on mountain road from rockslide

Fig. 12 Resort hotel damaged by rockslide in Shenxigou

Landslides and rockslides in the Longmenshan Mountains are quite common even without seismic activity due to the steepness of the mountains and heavy rains that occur during the summer months. With continuing aftershock activity and frequent rains, landslides and rockslides are continuing to occur on the mountain roads, often isolating communities and

cutting off vital services and supplies. The continuing landslides and rockslides will also make the recovery more difficult because access to the mountain towns and villages will be hampered. The access to move heavy equipment and material into the more remote areas by road is severely limited by the current conditions.

Fault Rupture

Fault rupture was prominent in the Longmenshan Mountains as the rupture was about 270 km in length. The fault rupture cut through towns, villages, and roads, causing much damage and havoc in the region. The fault movement was predominantly a reverse thrust in southwestern portion of the rupture, becoming more strike-slip towards the northeast. Fault rupture at Gaoyuan Village, north of Dujiangyan, is shown in Figures 13 and 14; Figure 13 shows about 1 meter of vertical displacement as evident in the concrete roadway and Figure 14 shows the effect of the fault rupture on a brick building nearby.

Fig. 13 Surface fault rupture with 2 meter vertical displacement at Gaoyuan Village

Fig. 14 Surface rupture under brick building at Gaoyuan Village

Fig. 15 Surface fault rupture contributed to failure of Gaoyuan Bridge; north abutment is to the left

The Gaoyuan Bridge, near Gaoyuan Village, is a two lane traffic bridge with north and south abutments and three bents over a river (Figure 15). The bridge suffered the collapse of the second simply supported span (from the north). The thrust fault rupture went through the north (left) abutment of the bridge and caused the approach slab to be thrusted over the first span of the bridge. In addition, part of the west wing wall of the abutment collapsed along with some of the fill in the abutment. This apparently caused the passive resistance of the north abutment to be reduced. There was also a failure of the south abutment which showed evidence of yield of the abutment and movement inwards towards the north (as the passive resistance at the north abutment was reduced). This movement of the abutment appears to have caused the spans of the bridge to be pushed northward. The movement was large enough that the second span became unseated at the center bent and fell to the ground below. The other side of the span hit the first bent and caused some bending of the piers.

The fault rupture was reported by CEA to be as much as 5 meters of vertical fault displacement with about 4.5 meters of horizontal fault displacement (Fig. 16). Fault rupture caused collapse of many structures that were constructed over the fault traces; as many of the buildings were of brick construction, total collapse was very common (Fig. 17).

Fig. 16 Surface fault rupture with 5 meter vertical displacement at Shenxigou

Fig. 17 Surface rupture causing total collapse of buildings at Xiaoyudong

Fault rupture also caused damage and collapse of several bridges, including the Xiaoyudong Bridge as shown in Figure 18 and the Baihua Bridge near Yingxiu as shown in Figure 19.

Fig. 18 Surface fault rupture caused damage and collapse of Xiaoyudong Bridge

Fig. 19 Collapse and severe damage of Baihua Bridge at Yingxiu caused by fault rupture

STRUCTURAL OBSERVATIONS

Brick masonry is the predominant type of construction in Sichuan Province. The two primary building types observed were unreinforced brick bearing wall buildings, particularly in the rural and mountainous areas, and restrained unreinforced brick infill shear wall buildings (also referred to as confined masonry buildings) used in mostly dense urban areas, such as Dujiangyan and Chengdu. Concrete moment frame buildings were present, but were not as numerous as brick buildings in the regions most strongly affected by the earthquake; there are numerous such buildings in Chengdu that were less affected by the earthquake. There were a few wood buildings, but primarily limited to distant rural areas.

The unreinforced brick bearing wall buildings were typically some two to four stories in height with precast hollow core plank floors and roofs which bear on transverse brick walls and longitudinal perimeter walls which may have many openings. As would be expected, this type of building did not perform well in the earthquake as there were many catastrophic collapses as shown in Figure 20.

Fig. 20 Unreinforced brick bearing wall building

Fig. 21 Restrained brick bearing wall building

Fig. 22 Steel reinforcing in brick bearing wall building

Fig. 23 Steel reinforcing and pebble aggregate used in column of brick bearing wall building

Restrained brick bearing wall buildings were typically long rectangular buildings with heights from three to seven stories with precast hollow core plank floors and roofs which bear on reinforced concrete beams spanning to reinforced concrete columns (see Figure 21); there is also a reinforced concrete perimeter ring beam. It was observed that beam stirrups and column ties were typically No. 3 undeformed bars with a fairly wide spacing of 12 inches or greater (Figures 22 and 23). There was no positive connection of floor planks to the bearing beams or perimeter ring beam except by bearing and friction contact. These buildings typically appeared to be stronger in the longitudinal direction than in the transverse direction because the ground floors typically had open storefronts. This type of building had performance that varied from what could be considered "life safe" performance (although there was significant and perhaps unrepairable damage) to partial and total collapse. Issues that may have contributed to poor performance include: poor ductile detailing, insufficient concrete cover over reinforcing steel, improper size and shape of aggregate in concrete, quality of cement, and poor quality of brick.

Although not as common in the Longmenshan Mountain region, concrete moment frame buildings appeared to perform much better than the adjacent brick buildings; however, we did not have the opportunity to observe many of these buildings. Although it was observed that some concrete moment frame buildings suffered from weak column/strong beam behavior, there were some buildings that performed remarkably well, even when in close proximity to the fault rupture, such as the newer building constructed in 2007 at the Bailu Middle School and another school building at the middle school in Tongji (see Figures 24 and 25).

Figure 24 Xuankou Middle School building in Bailu with fault rupture in foreground

Figure 25 Tongji Middle School building

It appeared that many of the bridges in the Longmenshan region have bridge spans that are simply supported at the ends, such as the Gaoyuan Bridge shown in Figure 15. A single span of one of the approaches to the tall Minjiang Bridge over the Zipingpu Reservoir became unseated and fell into the lake as shown in Figure 26. There were numerous other reports of bridges having simply supported spans becoming unseated and collapsing. New replacement bridges will need to consider higher seismic input as well as larger displacements. Existing bridges will need to be retrofitted to prevent unseating in future earthquakes and retrofit strategies used in California and the United States may be needed to prevent unseating.

Reports of damage at several bridges indicate that the lateral design for earthquake forces of bridges may not be sufficient given the ground motions of this earthquake. Some bridges had damaged shear keys at the abutments and bent caps when the strongest ground motions were in the transverse direction. Also, the Baihua Bridge had damage to the transverse beams between the piers as well as flexural distress near the base of some of the bent piers.

Fig. 26 Minjiang Bridge crossing over Zipingpu reservoir with one missing span

EMERGENCY RESPONSE AND RECOVERY

The response to the massive earthquake was quick and decisive. Although no country is prepared for a natural disaster of this scale, the response was quickly coordinated by the central China government who mobilized 130,000 soldiers of the People's Liberation Army (PLA) to provide search and rescue, restore access, and maintain order. Other China provinces and major cities sent personnel, equipment and resources to supplement the PLA and local forces. In addition, many private individuals and groups from all over China went to Sichuan Province to offer aid and support. Foreign aid and personnel were also accepted by China, unlike during the 1976 Tangshan earthquake. Undoubtedly there was some confusion on coordination and overlapping of responsibilities, however, the response was considered to be well done by many.

China's 50-member State Council, chaired by Premier Wen Jiabao, quickly established an Earthquake Rescue and Relief Headquarters that has provided most of the overarching principles and priorities for restoring the livelihoods and physical environment of the 51 counties (cities and districts) in the 132,596 square kilometers, disaster-affected region and its 20 million

residents. Three-month targets were established, heavily emphasizing the needs of survivors, as well as an ambitious and comprehensive set of three-year goals to ensure that every family has a house, every household has employment, every person has social and medical care, and that the infrastructure, economy and environment are all improved.

The State Council also took swift legislative action to establish a multi-governmental management framework for the recovery effort. The "Wenchuan Earthquake Disaster Recovery and Reconstruction Act" (passed into law on June 4, 2008) provides the legal basis for various departments and government entities both in and out of the quake-hit region to assist with recovery and reconstruction. The act specifies guiding principles for damage assessment, temporary housing, reconstruction planning, financing, implementation, and management.

A central element of China's post-disaster management framework is a pairing of affected with unaffected regions to help provide the resources and funds for recovery and reconstruction. The disaster-impacted areas of Sichuan, Gansu and Shaanxi provinces were divided into 24 districts and matched with 24 localities across China. For example, the town of Dujiangyan (within the administrative boundaries of the city of Chengdu) is sponsored by Shanghai. Yingxiu's sponsor is Guangzhou; Pengzhou's is Fujian, Mianzhu's is Jiangsu; and, Anxian's is Beijing. Each sponsoring locality has been given work tasks, funding and resource assignments as well as timeframes for their completion. Their contributions include provision of staff and human resources, "in kind" support from planning institutes and other agencies within the sponsor region, provision of temporary housing units, and donations and financial support. Banners acknowledging the work of sponsor locations are visible across the disaster-affected region.

As of August 25, the State Council reports that nearly 1.5 million disaster-affected people have been relocated; about 180,000 have been organized to work outside the disaster zone and about 678,000 people have found jobs in their hometowns (Xinhua, 2008). About 92% of the 139,000 damaged business outlet had been reopened; almost 663,000 temporary houses have been constructed and another 2,500 were being installed, and nearly all of the 53,295 km of roads damaged by the earthquake had been restored.

Sponsoring localities have been major suppliers of the temporary housing, and planning institutes from sponsoring localities have volunteered to plan the temporary housing encampments, following the design principles laid out by the central government in the Wenchuan Earthquake Disaster Recovery and Reconstruction Act. Figure 27 shows one temporary shelter in northeastern Dujiangyan. The processes for determining the number of units needed and the site selections are unclear. Local officials described site selections being determined based upon the availability of water, electricity, and access, but less certain about environmental and hazard considerations. Some very large encampments were observed in river floodplains and at the base of steep slopes. Many of the temporary housing encampments include temporary school facilities, such as the elementary school in Yingxiu shown in Figure 28.

Figure 27 Temporary housing in Dujiangyan

Figure 28 Temporary elementary school in Yingxiu

Within a week after the earthquake, the National Development and Reform Commission (NDRC) [China's lead agency for urban plan development], financing and approval, the Ministry of Housing and Urban-rural Development and the disaster-affected provinces established a special team on reconstruction planning to act on the planning principles outlined in the Wenchuan Earthquake Disaster Recovery and Reconstruction Act. Since its founding, the team made dozens of trips to the disaster-affected region collecting the input of local officials and getting input from the disaster-affected residents. A general reconstruction plan, as well as ten specific plans – covering urban systems, rural development, urban-rural housing, infrastructure, public service facilities, productivity distribution and industrial restructuring, market service system, disaster prevention and mitigation, ecological rehabilitation, land utilization, were developed for each of the three, disaster-affected provinces. These, in turn, were incorporated into a comprehensive reconstruction plan that released for public review on August 12. The "State Overall Planning for Post-Wenchuan Earthquake Restoration and Reconstruction" groups the 51 disaster-affected counties into 3 categories – areas suitable for reconstruction, areas suitable for appropriate reconstruction, and ecological reconstruction areas (with future growth limitations) – and sets the rebuilding and funding guidelines for each. The NDRC is currently soliciting feedback on the plan holding outreach workshops with international experts, and setting up special websites for comments at the NDRC, People's Net and China Net.

The recovery effort will be a great challenge, even with China's strong economy. According to Watts (2008), the reconstruction is estimated to have a cost of about 1 trillion yuan (US$147 billion). This amount is equivalent to one-fifth of the entire tax revenue of China for a single year. This will include providing new homes for 3.9 million refugees, replacing schools and creating jobs for 1 million people.

The infrastructure of the mountains will be a challenge to rebuild based on the geologic and climatic conditions, in addition to the continuing seismic activity. Some massive relocation of the population in the mountains may be required to remove people from the hazards and risks associated with the region. One of the most pressing challenges is in ensuring higher seismic standards and construction quality in the rebuilding. The reconstruction plan calls for higher earthquake-resistance levels of infrastructure construction in the quake-hit regions, especially for schools and hospitals. In rural areas, the reconstruction planning recommends that technicians help advise residents to rebuild safely; but, many villagers are moving ahead and reconstructing

with a variety of traditional and recycled materials, particularly reclaimed bricks. In urban areas, like Dujiangyan, damage assessments are complete. Unsafe buildings have been demolished and buildings that are moderately damaged have had all interior contents, furnishings, doors, windows removed and await repair. But, financing for the repairs has yet to be determined (Iin, 2008). The repairs may be too costly for government to fund alone and too costly for individuals to finance.

ACKNOWLEDGEMENTS

The support of the Earthquake Engineering Research Institute and its Learning from Earthquakes project is greatly appreciated. The Learning from Earthquakes project is funded by the National Science Foundation.

Appreciation is also extended to our colleagues at the Institute of Engineering Mechanics – China Earthquake Administration who were our gracious hosts in China. Special thanks to Prof. Zifa Wang, Director, and to Prof. Junwu Dai, who accompanied and hosted the EERI-GEER field investigation team in China.

The observations and insights of the other EERI-GEER team members (Dennis Lau, Jian Zhao, Tricia Wachtendorf, David Frost, J.-P. Bardet, and Tao Qiu are also greatly appreciated as they have contributed much to this paper. Additional information was provided by Ken Elwood, Mark Yashinsky, Moh Huang, and Stephen Malin. Special thanks to EERI Executive Director Susan K. Tubessing and Marjorie Green of EERI for helping to organize the field investigation, and to William Holmes, Chair of the Learning from Earthquakes program. Special thanks to Jenny F. Lew, whose help cannot be measured or appreciated enough.

REFERENCES

Burchfiel, B.C., L.H. Royden, R.D. van der Hilst, B.H. Hager, Z. Chen, R.W. King, C. Li, J. Lu, H. Yao, and E. Kirby (2008), "A geological and geophysical context for the Wenchuan earthquake of 12 May 2008, Sichuan, People's Republic of China," GSA Today, v. 18, no. 7, July.

Iin (2008), "Interview on Wenchuan rebuilding plannings, with Professor Iin, Vice Dean/Professor, Faculty of Architecture, Southwest Jiaotong University."

Massachusetts Institute of Technology Department of Earth, Atmospheric, and Planetary Sciences (2008), "Earthquake near Wenchuan, West Sichuan, China, 2008 May 12 06:28:01 UTC; Magnitude 7.9," http://quake.mit.edu/~changli/wenchuan.html

National Reform and Development Commission (2008), "The State Overall Planning for Post-Wenchuan Earthquake Restoration and Reconstruction (Public Opinion Soliciting Draft)."

United States Geological Survey (2008), Poster of the Eastern Sichuan, China Earthquake, Magnitude 7.9, ftp://hazards.cr.usgs.gov/maps/sigeqs/20080512/seismicitypgbb.pdf

Watts, J. (2008), "Sichuan quake: China's earthquake reconstruction to cost $150bn," The Guardian, August 15. http://www.guardian.co.uk/world/2008/aug/15/chinaearthquake.china

Xinhua News Agency (2008), "China Quake Death Toll Remains Unchanged at 69,226," www.chinaview.cn, August 25.